Investigation of Electron Irradiation-Induced Cross-Linking of *p*-Terphenyl Thiol Self-Assembled Monolayers on Au(111) by Scanning Tunneling Microscopy

Inaugural-Dissertation

zur Erlangung des akademischen Grades Dr. rer. nat.

der Fakultät für Physik

der Universität Bielefeld

vorgelegt von

M.Sc. Patrick Stohmann

Bielefeld, February 2020

I hereby declare that I have written this thesis independently, that I have not used any resources other than those specified, and that I have identified all resources used for this thesis.

Erstgutachter: Herr Prof. Dr. Armin Gölzhäuser

Zweitgutachter: Herr Prof. Dr. Dario Anselmetti

Abstract

The unique attribute of *carbon nanomembranes* (CNMs) in molecular separation is their capability to overcome the typical trade-off between permeance and selectivity for conventional membranes[9],[1],[2]. These two key properties determine the performance and energy-efficiency of materials when used for molecular separation in filtration systems. CNMs are molecularly thin membranes that can act as two-dimensional sieves due to the presence of sub-nanometer conduits. CNMs are fabricated by cross-linking of aromatic *self-assembled monolayers* (SAMs), e.g. *p-terphenylthiol* (TPT) SAMs. Cross-linking can be achieved by irradiation with low-energy electrons. TPT CNMs, in particular, have shown great potential in water separation[9]. Spectroscopic methods have provided deeper insight into structural and chemical transformations associated with cross-linking[53],[13],[11],[14],[50] but molecularly resolved microscopic data on characterizing cross-linking is available only rarely[9].

In this work, electron irradiation-induced cross-linking of aromatic SAMs was studied by *scanning tunneling microscopy* (STM), employing TPT SAMs on Au(111) on mica as a model system for aromatic SAMs. SAMs were prepared from *dimethylformamide* (DMF)-based solution and from the vapor phase under *ultra-high vacuum* (UHV) conditions. CNMs from TPT SAMs are commonly prepared from DMF-based solution[9],[1]. SAMs prepared from the gas phase, however, are of similar structure and have proven to be more suitable for STM experiments. SAMs were cross-linked either by exposing the sample to the homogeneous 50 eV electron beam of an in-situ flood gun or by exposing the sample to the focused, scanning 1 keV electron beam of a *scanning electron microscope* (SEM). Both primary electron energies are expected to cause similar modifications of the monolayer/substrate system as XPS analysis has revealed similar cross-sections for the modification of the carbonaceous matrix and the sulfur-gold interface, respectively. The advantage of employing the combined STM/SEM system, however, is the chance to acquire STM images of the same sample location before and after electron irradiation and thus to observe the influence of the electron impact on the local, molecular level.

TPT SAMs were characterized by high-resolution STM. Two distinct, ordered phases were observed for SAMs prepared from DMF-based solution, denoted as α-phase and β-phase. Both phases were observed previously for TPT SAMs on Au(111) which were prepared in ethanolic solution and subsequently annealed in ethanol at 40°C[39]. The α-phase consists of densely-

packed molecules in the well-known $(2\sqrt{3} \times \sqrt{3})$R30° structure with two molecules per unit cell. The monomers occupy an area of 0.216 nm² and adopt tilt angles of γ~13°[39]. The β-phase is characterized by a point-on-line incommensurate $\begin{bmatrix} 4 & 0 \\ 0 & n \end{bmatrix}$ with n close to 8 and 8 molecules per unit cell. The monomers occupy an area of 0.288 nm² and adopt tilt angles of 33-49°[39]. SAMs prepared from the gas phase are characterized by the absence of α-phase domains. Instead, the largest part of the substrate surface is covered with β-phase domains. Moreover, domains of a slightly distorted β-phase were observed and identified. This phase can be described by a $\begin{bmatrix} 4 & 0 \\ -1 & n+1 \end{bmatrix}$ lattice with n close to 8. Typical domains sizes for SAMs prepared either from DMF-based solution or from the gas phase are 10-100 nm. It was found that SAMs prepared from the gas phase are much more suitable for STM experiments due to the total absence of mobile impurities or adsorbates that may lead to unstable imaging conditions.

STM data indicates that the initial stage of cross-linking in TPT SAMs, which has been caused by the impact of 50 eV and 1 keV electrons and only a few electrons per monomer, is characterized by the propagation of radical chain reactions, as proposed previously[14]. The chain reactions apparently involve up to 33 molecules and 5–6 monomers on average until they are terminated, and they are probably accompanied by a partial cleavage of S–Au bonds. The first radicals initiating individual chain reactions may form upon 6 eV (secondary) electron attachment, but different electron-molecule primary interactions producing radicals cannot be excluded. Potential termination mechanisms cannot be deduced from the STM data but different mechanisms are proposed.

In the further course of cross-linking, the long-range molecular order is reduced significantly compared to the pristine SAM. Pristine-like domains are typically less than 10 nm in size, being separated by apparently cross-linked, amorphous parts of the monolayer. The reduction of the average regular phase domain size is supported by STM data acquired within the scope of complementary STM/SEM experiments. The evolution towards the nearly fully cross-linked state is characterized by a loss of long- and short-range molecular order. Sub-nanometer-sized voids were observed, which can possibly be assigned to sub-nanochannels or pores in the transferred TPT CNM. Similar structures were were previously found and characterized[9]. The average void diameter was estimated to 0.5 ± 0.2 nm and the areal void density to $\sim 1.7 \times 10^{17}$ m^{-2} which is in agreement with previous findings[9].

Acknowledgement

Scientific education is tough. It can be daunting or liberating. Learning from former researchers, racking one's brain through the years, and eventually making own discoveries. But all's well that ends well - if you are not alone. I would like to express my deepest thanks and gratitude to all people who assisted me during my PhD, providing me help and support whenever needed.

I am greatly indebted to my research supervisor, ***Prof. Dr. Armin Gölzhäuser,*** for introducing me to the field of membrane technology and for giving me the opportunity to contribute to the research of *carbon nanomembranes*. He always offered me sufficient freedom in thinking and acting throughout my doctoral research, allowing me to develop my self-awareness in research; something I will benefit from during my entire future career and my life. I am very grateful for his assistance and support in discussions and feel glad of having chosen his research group to graduate.

I wish to thank the **members of my dissertation committee** for generously offering their time, energy, and their good will throughout the review of this thesis.

I warmly thank ***Dr. Sascha Koch*** for his professional guidance throughout the major part of my doctorate, his constant encouragement and all personal stories and funny anecdotes he shared with us. Thanks to Sascha, I could develop my knowledge about surface analytical techniques, in particular scanning probe techniques, in quite a short time. I truly acknowledge his strong leadership which was always wrapped in sympathy and a great talent for motivation. I am thankful for numerous coffees for takeaway (and free), for all good advices for travelling and restaurants, and for this delicious racelett in the presence of his wife and daughter.

My special thanks to ***Dr. Berthold Völkel*** for being not less than "a rock in the waves" for all group members. He provided everyone, including me, with unconditional help, advice, patience and timely technical assistance when working on the more than complex UHV surface analytical system.

I would like to express my gratitude to ***Dr. Xianghui Zhang*** for providing me important input and feedback regarding my understanding of the underlying mechanisms of molecular cross-

linking. I profited a lot from his deep knowledge and our discussions -always in friendly and welcoming atmosphere- truly helped me in interpreting my data.

I want to thank ***Dr. Udo Werner*** for giving me his confidence and support throughout the years to run a part of his course on practical physics. The extensive and detailed content does not only serve the undergraduates!

I would like to thank ***Dr. Yang Yang*** and ***Le Hoang Linh*** for preparing high-quality SAMs for my experiments, and for the patience when I asked for more. Thank you also for some pleasant short journeys. Thank you, Linh, for a mind-blowing joint trip through your home country under your caring guidance.

I would like to thank ***Christoph David Kaiser*** for his assistance in the laboratory, in particular for developing useful software, for setting up the flood gun, for all his help with maintenance work, and for good contributions to our discussions.

I want to thank all my PhD colleagues, office mates, and friends for a pleasant time, all encouraging words, numerous constructive and fruitful discussions in the office and during lunch break, excellent feedback, and multiple "after-work meetings" with fun and some tasty beer. Thank you, ***Dr. André Beyer, Niklas Biere, Raphael Dalpke, Dr. Daniel Emmrich, Dr. Natalie Frese, Christoph David Kaiser, Riko Korzetz, Linh Hoang Le, Florian Paneff, Dr. Paul Penner, Michael Westphal, Dr. Yang Yang*** (sorted by surnames).

Special thanks to ***Dr. Nikolaus Meyerbröker***, ***Dr. Henning Vieker*** and ***Dr. Polina Angelova*** for various helpful advices in the laboratory and, in particular, for improving the STM scanning tip conditions multiple times during the scan.

My acknowledgment would be incomplete without mentioning my *parents*, my *family*, and my *friends*, who have continuously provided me with encouragement and unfailing support not only during my doctoral research and all the challenges related thereto, but throughout my entire life.

List of Abbreviations

AFM *atomic force microscopy*
BPT *biphenylthiol*
CNM *carbon nanomembrane*
CP-AFM *conductive-probe atomic force microscopy*
CTE *coefficient of thermal expansion*
DEA *dissociative electron attachment*
DFT *density functional theory*
DI *dissociative ionization*
DMF *dimethylformamide*
DOS *density of states*
EA *electron attachment*
FFT *fast Fourier transform*
FWHM *full width of half maximum*
HIM *helium ion microscopy*
HOMO *highest occupied molecular orbital*
HOPG *highly oriented pyrolytic graphite*
HREELS *high resolution electron energy loss spectroscopy*
IMFP *inelastic mean free path*
KPFM *kelvin probe force microscopy*
LDOS *local density of states*
LEED *low-energy electron diffraction*
LUMO *lowest unoccupied molecular orbital*
NBPT *nitrobiphenylthiol*
ND *neutral dissociation*
NEXAFS *near edge X-ray absorption fine structure*
nSs *new sulfur species*
PDMS *polydimethylsiloxan*
PE *primary electron*
PVD *physical vapor deposition*
SAM *self-assembled monolayer*
SEM *scanning electron microscopy*
SEY *secondary electron yield*
SPM *scanning probe microscopy*
STM *scanning tunneling microscopy*
TEM *transmission electron microscopy*
TNI *transient negative ion*
TPT *p-terphenylthiol*
UHV *ultra-high vacuum*
UV *ultraviolet radiation*
vdW *van der Waals*
XPS *X-ray photoelectron spectroscopy*

Contents

1 Introduction

If you folded a regular sheet of paper (80 g/m²) 27 times, the stacking height would overcome the height of Mount Everest. If you did the same with a *carbon nanomembrane* (CNM), the membrane stack would barely reach your ankle. CNMs represent a specific class of synthetic nanomembranes[1],[2]. Whereas the term "nanomembrane" often denotes membranes with thicknesses less than 100 nm, CNMs with monomolecular thickness exhibit the nearly minimum possible material thickness beside graphene. A free-standing CNM prepared from *p-terphenylthiol* (TPT) precursors can be seen in the *helium ion microscopy* (HIM) image shown in Figure 1.1 (a). The membrane is suspended over a micrometer-sized *transmission electron microscopy* (TEM) mesh grid. CNMs are fabricated by cross-linking of aromatic *self-assembled monolayers* (SAMs), e.g. by irradiation with low-energy electrons (see Figure 1.1 (c)). The resulting sheet can subsequently be released from the supporting substrate by employing a sophisticated transfer process[3] and placed on other surfaces. Despite their minimal thickness (~1 nm) even thinner than cell membranes, CNMs show excellent mechanical strength[4],[5] and, beyond that, are highly resistant to chemicals[1] and heat[6]. CNMs are built in a versatile and scalable fabrication process and can further be tailored with physical, chemical or biological function[1],[7]. Moreover, CNMs show high potential in membrane filtration applications. The final CNM molecular structure is of rather amorphous nature and can sustain nanoscale pores or even sub-nanometer-sized pores[9],[11]. The pores may facilitate selective transport in membrane separation processes, thereby acting as *molecular sieves*. Gas permeation characteristics of single-layer and multilayer CNMs prepared from *biphenylthiol* (BPT) and *nitrobiphenylthiol* (NBPT) precursors were reported for the first time in 2014 by Ai *et al.*[8], revealing that gases of small kinetic diameter, i.e. He and H_2 are subject to a significantly higher permeance compared to larger molecules, i.e. CO_2, Ar, O_2, N_2, CH_4, and C_2H_6, in particular in multilayer CNMs. A schematic illustration of a single-layer BPT CNM on *polydimethylsiloxan* (PDMS) including pores (bright regions) is shown in Figure 1.1 (b). CNMs with appropriate pore sizes may therefore be utilized for energy-efficient natural gas purification, e.g. production of oxygen or nitrogen from air. It should be noted that pores constitute open pathways through the membrane for distinct molecular species. Open pathways for small molecules such as He or H_2 may still block larger molecules, e.g. CO_2 and therefore not act as pores for the latter species. In order to efficiently filtrate distinct molecular

species selectively, a narrow pore size distribution and a low areal density of defects is therefore generally of particular importance. Tremendous effort has also been invested to extend the utilization of CNMs towards water purification. The ability of CNMs prepared from TPT precursors to combine high water selectivity with an exceptionally high permeance was shown by Yang *et al.* in 2018[9], opening new pathways to applications in water purification, water desalination, membrane distillation, dehydration of organics and dehumidification of gases. In combination with their minimal thickness, CNMs can overcome the typical trade-off between permeance and selectivity applying for conventional bulky membranes[10]. The permeance describes how fast the molecules can pass through the membrane. The selectivity describes the ability of a membrane to separate the target molecules from impurities. In conventional membrane filtration processes, selective mass transport is usually achieved by a solution-diffusion process which is energy consuming and requires a high mechanical stability of the membrane. Here, material flow through the membrane is limited by the membrane thickness and a higher selectivity can only be achieved at the expense of throughput and vice versa. Thin selective membranes such as CNMs may overcome this fundamental dilemma.

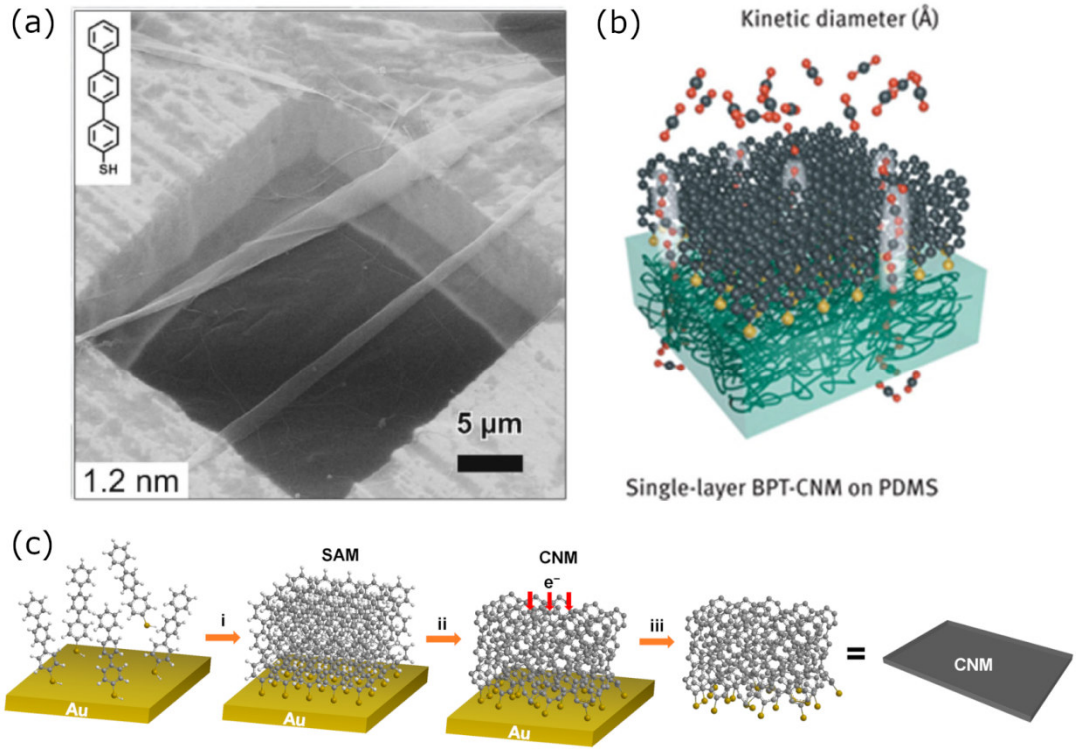

Figure 1.1: (a) Helium ion microscope (HIM) micrograph of a free-standing CNM prepared from TPT precursors (see upper left inset). The CNM is suspended over a gold TEM grid. The number in the lower left corner indicates the CNM thickness as determined from XPS before the transfer. (b) Schematic depiction of the proposed gas transport mechanism in single-layer BPT CNMs on PDMS support. Small gas molecules can permeate through channels of molecular size (highlighted by bright regions). (c) Preparation and transfer of TPT CNMs. TPT precursor molecules self-assemble on Au substrates and form a densely-packed SAM. Cross-linking by electron irradiation converts the SAM into a CNM that can be released from the substrate and transferred onto suitable supports. *Part a is reprinted and adapted with permission from ref [11]. Copyright (2013) American Chemical Society. Part b is reprinted and adapted with permission from ref [8]. Copyright (2014) John Wiley and Sons. Part c is reprinted and adapted with permission from ref [9]. Copyright (2018) Americal Chemical Society.*

The CNM molecular structure is of key importance in providing high performance in molecular separation. An essential feature of the membrane molecular structure facilitating the separation of target molecules from impurities is the presence of pores. Pores allow the passage of target molecules through the membrane; whereas other feed mixture components permeate the membrane at lower rates or are being efficiently blocked. Depending on the porosity of the membrane, in particular on shape and size of the pores, different transport mechanisms dictate the performance of a membrane in terms of permeance and selectivity[10]. An adequate choice of the molecular precursors (and the substrate material) may allow to control and tune the size, the areal density, and the chemcial nature of the pores and thus to control the membrane filtration performance. In particular, CNMs with a mean size of the pores of ~6 nm and 2.4 nm were prepared[11]. Pores in CNMs with diameters down to 1.3 nm were even created artificially

by employing the focused helium ion beam of a HIM[12]. The size of the intrinsic pores in TPT CNMs was estimated based on *atomic force microscopy* (AFM) data and an upper limit for the active pore diameter of 0.7 ± 0.1 nm was found. Figure 1.2 (a) shows STM and AFM image excerpts of the pristine SAM (left) and the cross-linked monolayer (right). In the pristine SAM, the monomers arrange themselves into a regular "zig-zag pattern". In the cross-linked monolayer, sub-nanometer-sized pores were observed that might be formed by several cross-linked monomers as highlighted schematically. Permeation data indicates that those pores efficiently block the passage of most liquids and gases but facilitate the permeance of water molecules. The estimated single-channel water permeation coefficient indicates that water transport through the pores of TPT CNMs is similar to water transport through aquaporin and carbon nanotubes (see Figure 1.2 (b)).

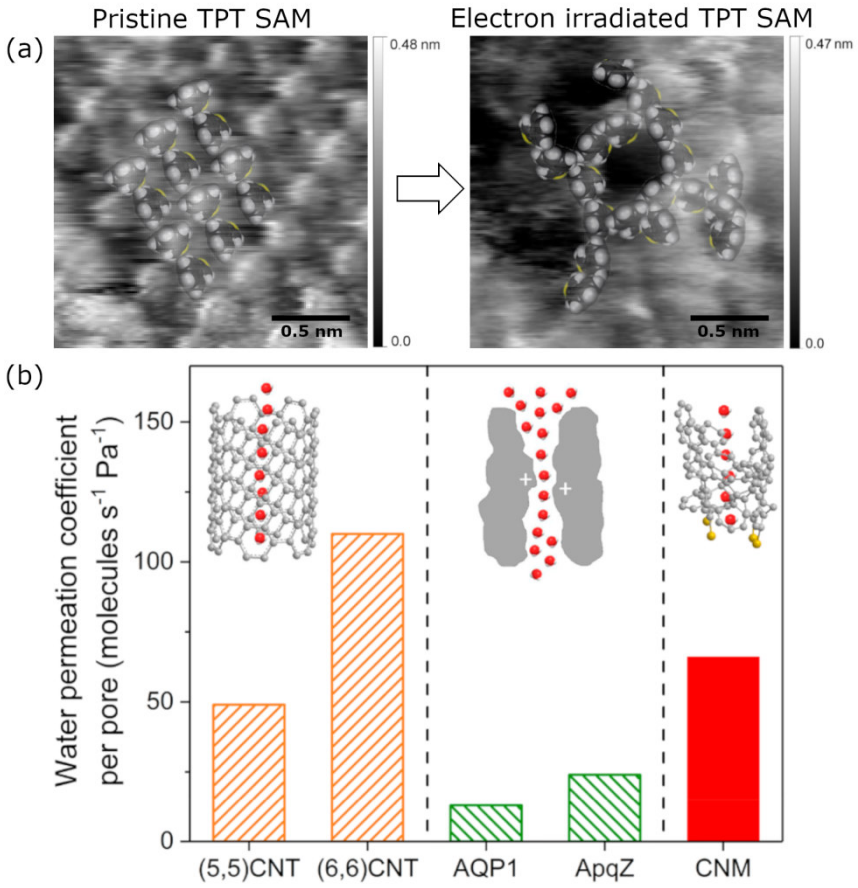

Figure 1.2: (a) Morphology of TPT SAM and CNM. (left: STM image of TPT SAM measured at room temperature in ultrahigh vacuum (U=790 ṉ V, I=40 pA); right: AFM image of TPT CNM measured at 93 K in UHV via AFM tapping mode of operation (amplitude set point A = 7.6 nm, center frequency f 0 = 274.8 kHz)). Molecular arrangements are highlighted by drawings of molecular monomers. (b) Comparison of single-channel water permeation coefficients of carbon nanotubes, aquaporins and pores in TPT CNMs. *Part a is reprinted and adapted with permission from ref 9. Copyright (2018) American Chemical Society. Part b is reprinted with permission from ref 9. Copyright (2018) American Chemical Society.*

The formation of pores proceeds during cross-linking by irradiation with energetic particles, e.g. electrons. While the spatial separation of adjacent monomers in the pristine SAM is essentially given by the *van der Waals* (vdW) dimensions of the monomers, intermolecular cross-linking, that is, the formation of intermolecular carbon-carbon bonds may lead to a reduction of the spatial separation of adjacent monomers and thereby to the formation of (sub-) nanometer-sized voids within the molecular layer[13]. Those voids may be preserved and act as pores when the cross-linked film is released from the substrate and employed in molecular separation processes. The molecular structure, rigidity, and dimensions of the pores is strongly influenced by the choice of the molecular precursors. In particular, the molecules should be able to form cross-links in two dimensions which is the case for TPT precursors as they can form independent cross-links via three rotable phenyl rings. The molecular packing density of the pristine SAM and the ability of the molecular monomers to undergo reorientations during cross-linking should also play a significant role for the molecular structure of the membrane and the dimension and areal density of the pores. A thorough microscopic study as performed for this thesis should provide deeper insight into the fundamental mechanisms of cross-linking, the structural transformation of the molecular layer during cross-linking, and the formation of pores.

1.1 Motivation and Thesis Outline

Spectroscopic data has provided deep insight into the molecular mechanisms of cross-linking[13],[14],[53]. However, detailed information about the influence of electron impact on the scale of molecular phase domains or even on the molecular scale is still lacking. This work aims to investigate electron irradiation-induced cross-linking by *scanning tunneling microscopy* (STM), focusing on structural transformations of the monolayer. For this purpose, TPT SAMs were employed as model aromatic SAM*s*. SAMs were cross-linked under *ultra-high vacuum* (UHV) conditions ($< 10^{-10}$ mbar) by delivering distinct intermediate 50 eV (flood-gun) and 1 keV (SEM) electron doses (< 50 mC/cm²) to the surface. Cross-linking of TPT SAMs is commonly achieved by irradiation with 50-100 eV electrons using a dose of 50 mC/cm². Within the scope of this thesis, however, a combined STM/SEM system (see section 3.2.3) was used that allows for acquiring STM data of the same sample location before and after electron-irradiation, thus enabling to observe the influence of the electrons on the SAM on the local, molecular level. The minimum kinetic energy the SEM can provide, however, is 1 keV.

The first research objective of this work is to unravel the initial stage of cross-linking, that is, the response of the monolayer to electron doses of only 1 % of the value required to obtain a "fully cross-linked" molecular film. The identification of elementary structural changes, that is, local modifications of the monolayer that can be ascribed to the impact of single electrons, is here of particular interest. This may reveal whether or not cross-linking propagates via radical chain reactions, as previously proposed[14]. Further research objectives are the investigation of the structural evolution from the pristine SAM to the fully cross-linked molecular film. This should provide deeper understanding about the formation of CNMs from TPT precursors. In particular, the observation and characterization of sub-nanometer voids or "pores" may support previous findings and assumptions about the molecular sieving mechanisms of TPT CNMs[9].

Chapter 2 provides basics and theoretical considerations about the preparation and characterization of SAMs and on the present knowledge about the molecular mechanisms of electron irradiation-induced cross-linking of aromatic SAMs, primarily deduced from spectroscopic data. Information is given about the effects of cross-linking on the structural, chemical and electronic properties of aromatic SAMs. The following sections introduce the main methodologies employed for this thesis to characterize pristine and partially irradiated SAMs, i.e. STM and *X-ray photoelectron spectroscopy* (XPS). In particular, preliminary considerations on the effect of cross-linking on the STM image contrast are made.

Chapter 3 presents the materials and methods employed for this thesis, involving detailed information about the analytical instruments and the experimental parameters employed, how the experimental data was processed and how SAMs from TPT precursors on Au(111) were prepared, cross-linked and characterized.

Chapter 4 presents the XPS and STM data acquired for this thesis covering the structural and chemical transformation from the pristine TPT SAM to the nearly fully cross-linked film. SAMs of oligo(phenyl)thiols on Au(111) and their response to 50-100 eV electron irradiation have already been investigated thoroughly by XPS[15],[13]. The main purpose of employing XPS for this thesis is to quantify the effect of the electron energy on the structural modification of the monolayer as monolayers were irradiated with 50 eV and 1 keV electrons (see above). This makes it possible to compare STM images of monolayer that were irradiated with different electron energies. The data is presented in the first section. In the following section, STM data

on the characterization of the pristine SAM surfaces that were prepared either in *dimethylformamide* (DMF) or from the gas phase under UHV conditions is presented. Afterwards, STM data on the initial stage of cross-linking is presented. Eventually, the evolution of the monolayer towards the fully cross-linked state is investigated and the structural transformation accompanied therewith.

Chapter 5 draws final conclusions of the present study and provides outlook for future research.

2 Basics and Theoretical Considerations

This chapter first focuses on the structure and preparation of *self-assembled monolayers* (SAMs) on solid substrates and their structural and chemical conversion into laterally cross-linked, two-dimensional molecular sheets as well as the underlying molecular mechanisms of cross-linking. The motivation of this thesis, basically the investigation of cross-linking of aromatic SAMs by *scanning tunneling microscopy* (STM), is formulated in detail. Finally, the operation principles of the surface analytical methods employed for this thesis, STM and *X-ray photoelectron spectroscopy* (XPS), are described in detail.

2.1 Self-Assembled Monolayers

SAMs are ultrathin molecular films that form on suitable substrates by adsorption and subsequent self-organization, that is, by exposing a bare substrate (e.g. metals like Au, Ag, Cu, Pd, Hg, metal oxides like Al_2O_3, SnO_2, TiO_2, SiO_2, or 'functionalized semiconductors' like Si–H, or semiconductor surfaces like GaAs, InP) to specific amphiphilic molecular precursors (e.g. aromatic or aliphatic hydrocarbons with suitable head groups, e.g. –SH, –COOH , –OH, trichlorosilane) a well-ordered and densely-packed molecular assembly is generated spontaneously on its surface[16],[17],[18].

The building blocks for SAMs are the precursor molecules (see Figure 2.1 (a)). They can generally be divided into three parts: (a) the *head group* (also called anchor group, linking group or ligand), (b) the *spacer* (also called backbone), and (c) the *functional group* (also called terminal group). The orientation of the molecules with respect to the substrate surface is typically defined by the tilt angle α, which is the angle between the molecular backbone and the surface normal direction; the twist angle β which describes the rotation of the molecular backbone plane with respect to the molecular axis; and the precession angle χ which gives the tilt direction and is derived from the projection of the inclination plane (defined by the substrate normal and the axis of the molecular backbone) on the substrate plane[20] (see Figure 2.1 (b)).

The choice of the precursors plays a crucial role for defining the physical, chemical and interfacial properties of the monolayer/substrate system. The head group mediates the chemical bond of the precursors to the substrate surface, which is, in particular, of covalent

nature in case of self-assembled organothiols on gold. The spacers stabilize the molecular assembly through (intermolecular) van der Waals (vdW) interactions. The final SAM structure arises from a complex interplay between the adsorption kinetics and the adsorption energy ΔE_{ads} of the molecular precursors, the interchain interaction energy ΔE_{int}, and the substrate-headgroup binding energy ΔE_{bind}[21],[22]. The choice of the spacer also defines the mechanical, electrical, thermal, and optical properties of the SAM, and in particular, the response of the SAM to ionizing irradiation (see section 2.2). The macroscopic surface properties of the SAM (e.g. wetting, adhesion, tribology, corrosion resistance, electrochemistry, and immobilization of biomolecules[18],[20],[23],[24]) define its interaction with the (chemical) environment; they can be tuned by a suitable choice of the functional group. SAMs can be integrated into organic electronic devices, such as ultra-sensitive label-free biosensors and SAM/organic transistors[25],[26]. In this context, their ability to tune the work function of metal electrodes is of particular importance[27],[91]. The use of SAMs for patterning surfaces enlarges the range of applications to nanolithography. Due to their monomolecular thickness, SAMs can be employed as positive and negative tone electron beam resists with ultra-high resolution[48]. All previously mentioned applications comprise SAMs on solid supports. However, aromatic SAMs can even be laterally cross-linked and transferred as monomolecular thin membranes on micrometer-sized holes (see below), which provides an innovative technology in the field of membrane separation[1],[2],[9].

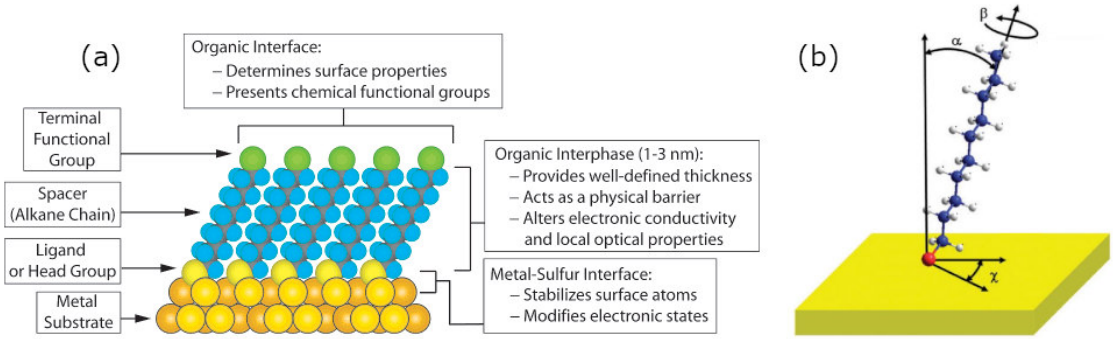

Figure 2.1: (a) Schematic diagram depicting a self-assembled monolayer (SAM) of alkanethiolates on a metal substrate. (b) Scheme of a decanethiol molecule adsorbed on a solid surface. The orientation of the molecule with respect to the substrate surface is defined by the tilt angle α, the twist angle β, and the precession angle χ. *Part a is reprinted with permission from ref 16. Copyright (2005) American Chemical Society. Part b is reprinted with permission from ref [20]. Copyright (2010) Royal Society of Chemistry (Great Britain).*

2.1.1 The Langmuir adsorption model

The Langmuir adsorption model[28] explains the kinetics of adsorption on a rather fundamental level, that is, by assuming that i) the surface of the solid adsorbent is homogeneous, that is, the adsorption sites are equivalent, ii) the adsorbates occupy the sites with probability $p = 1$ (free site) and $p = 0$ (occupied site), iii) no interaction between the adsorbates on adjacent sites takes place, and iv) the adsorbate coverage is limited by one monolayer.

In case of single non-dissociative adsorbates, the adsorption rate r_{ads} and desorption rate r_{des} are given by

$$r_{ads} = k_{ads} \times p_A \times c_{b.s.} \qquad \text{Equation 2.1}$$

$$r_{des} = k_{des} \times c_A \qquad \text{Equation 2.2}$$

where k_{ads} and k_{des} are the adsorption and desorption constants, respectively, p_A is the partial pressure of the adsorbate, c_A is the surface adsorbate concentration, and $c_{b.s.}$ is the surface concentration of the bare adsorbtion sites.

In the equilibrium state, the surface coverage of the adsorbent θ_A is given by

$$\Theta_A = \frac{K_{eq} \cdot p_A}{1 + K_{eq} \cdot p_A} \text{ with } K_{eq} = \frac{k_{ads}}{k_{des}} \qquad \text{Equation 2.3}$$

where K_{eq} denotes the equilibrium adsorption rate.

If the adsorption rate k_{ads} exceeds the desorption rate k_{des}, that is, $K_{eq} > 1$, the Langmuir adsorption isotherm is characterized by a leveling-off behavior of the surface coverage θ_A. As previously mentioned, the previous model considers the simplest case of adsorption. It does not account for the competitive adsorption of different adsorbate species *A* and *B,* for the case of dissociative adsorption, for rough surfaces with inequivalent adsorption sites, for adsorbate-adsorbate interactions, or for multilayer adsorption. Extensions of the basic Langmuir model can be found in the literature[29]. In particular when the monolayer is formed in the liquid phase, solvent-substrate and solvent-adsorbate interactions need to be taken into account (see below).

2.1.2 Vapor Phase Deposition vs. Liquid Phase Deposition

Two preparation methods are commonly used to prepare SAMs on substrates: i) SAMs are formed by immersing a clean substrate in a dilute solution of molecular precursors or ii) SAMs are prepared by vapor deposition; typically under UHV conditions. Fundamental aspects concerning both techniques are described below.

SAM formation by vapor deposition requires sophisticated UHV equipment and may be of lower throughput compared to the preparation from solution but may yield SAMs of high purity due to the absence of a solvent and other contamination sources, making them suitable for spectroscopic or microscopic studies, in particular SPM experiments. However, adequate vapor pressures are required allowing for thermally evaporating the precursors while avoiding thermal degradation. This is problematic in particular for long-chain alkanethiols. The monolayer coverage is typically controlled by the exposure time of the substrate to the molecular stream. The assembly of thiols on gold from the vapor phase at low coverage typically involves the formation of one or more low-coverage phases, characterized by an ordered pattern of molecules lying flat. The growth kinetics may be approximated by simple first-order Langmuir adsorption kinetics[30]. At higher coverage, that is, when steric interactions between the precursor molecules become relevant, adsorption becomes more complicated involving different (intermediate) phases[31],[32],[33]. The final state of self-assembled (aliphatic and aromatic) organothiols on Au(111) is typically characterized by a densely-packed molecular layer of (nearly) upright-standing molecules, accompanied by a conversion of the molecules to thiolates via dissociative adsorption and therefore by a transition from a physisorbed state to a chemisorbed state[16]. The specific ordering of the SAM is strongly determined by the energetic of the metal-sulfur bonds and the attractive intermolecular interactions between the molecular spacers via vdW forces and hydrogen bonding interactions[16].

SAM formation in solution is a rather complex process compared to gas phase formation in UHV due to additional solvent-substrate and solvent-adsorbate interactions. For this thesis, TPT SAMs on Au(111) on mica were prepared in a 1 mM solution of TPT in dry, degassed DMF by immersing the clean gold substrate in the solution for one day at 70 °C (see section 3.1.3). Another common method to prepare organothiolate-based SAMs is to employ ethanolic solution of the precursors [16]. The adsorption process of terphenyl-derivatized thiols

was investigated by STM involving different solvents[34]. The most important parameters influencing the final SAM structure are the nature of the solvent, the concentration of the solute, the immersion time, and the adsorption temperature. At low coverage, that is, immediately after adding the substrate to the precursor solution, SAM growth can be described by Langmuir adsorption (see above)[35]. The precursor adsorption rate is influenced and may be lowered by interactions between solvent molecules and the substrate surface[16]. The SAM growth rate is significantly lower at higher coverage (~ 80%) due to the reorientation of the precursors in order to obtain a densely packed SAM layer with (nearly) upright-standing monomers, similar to SAM growth from the vapor phase. SAM preparation may therefore require immersion times up to one day. The fabrication of SAMs from solution is reasonable if the SAM is subsequently exposed to other liquids, for example biosensor applications[23], water filtration[9], or wetting studies[36].

2.1.3 Organothiolate-based SAMs at High Surface Coverage

For this thesis, *p-terphenylthiol (*TPT) SAMs were prepared on Au(111) on mica. TPT molecules form well-ordered SAMs on noble metal surfaces, such as Au(111)[39],[40],[112] or Ag(111)[124]. The gold surface is well-suited for the fabrication of SAMs from thiol-containing precursors. The low chemical activity of the gold surface provides protection against oxidization and most chemicals but binds thiols with high affinity[19]. The gold surface is easy to clean via ozone treatment and subsequent rinsing with ethanol. TPT SAMs were prepared either from *dimethylformamide* (DMF)-based solution or from the gas phase under *ultra-high vacuum* (UHV) conditions. Both preparation methods bring their own advantages and disadvantages in terms of the ease of fabrication, cleanliness, throughput and the quality and structure of the monolayer. However, the basic mechanisms underlying the respective formation processes are similar, but their understanding is complex and requires the consideration of both kinetic and thermodynamic factors[16].

The molecular ordering of organothiolate-based SAMs (aliphatic and aromatic SAMs) on Au(111) at high surface coverage is generally dictated strongly by the local $(\sqrt{3} \times \sqrt{3})R30°$ overlayer domain structure of atomic sulfur on Au(111)[20],[37] at highest coverage (0.28 ML), indicating the influence of the interaction between the sulfur anchor groups and the Au(111) surface on the molecular assembly. This ordering also determines the maximum packing density of the SAM molecules. Figure 2.2 shows a structural model for the local $(\sqrt{3} \times \sqrt{3})R30°$

domains (black circular borders) of sulfur atoms (red circles) on Au(111) (yellow circles). In case of atomic sulfur on Au(111), the local $(\sqrt{3} \times \sqrt{3})R30°$ ordering may further be found within a (5×5) ordered domain structure (black unit cell)[37]. The sulfur atoms are shown in equivalent hollow sites on the underlying Au(111) surface.

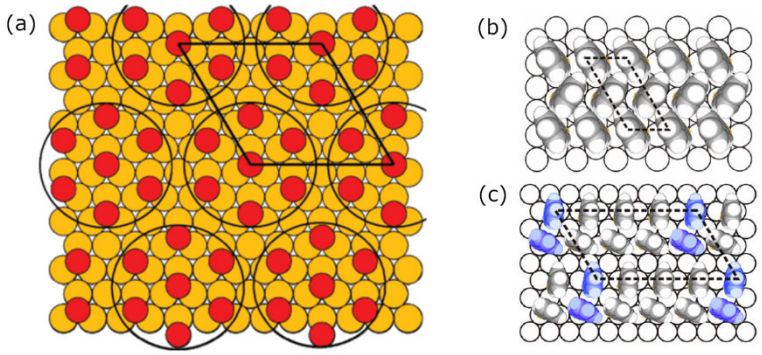

Figure 2.2: (a) Structural model for the (5×5) phase at highest surface coverage (0.28 ML) of sulfur atoms (red circles) on Au(111) (yellow circles). The sulfur atoms locally form $(\sqrt{3} \times \sqrt{3})R30°$ domains (black circular borders). The sulfur atoms are shown in equivalent hollow sites on the underlying Au(111) surface. The unit cell for the (5×5) phase is drawn. (b) $(2\sqrt{3}\times\sqrt{3})R30°$ structure of TPT SAM on Au(111). The unit cell is drawn by black, dashed lines. (c) $(4\times n)$ structure with $n \sim 8$. The unit cell is drawn by black, dashed lines. *Part a is reprinted and adapted with permission from ref [37]. Copyright (2007) American Chemical Society. Part b and c are reprinted and adapted with permission from ref [39]. Copyright (2013) American Chemical Society.*

The complex interplay between the anchor group-substrate interactions and the interactions between the molecular spacers generally leads to a secondary ordering of the molecular layer. Depending on the preparation procedure, the molecules can form different supperlattice structures. TPT SAMs on Au(111) prepared from ethanolic solution at room temperature are typically characterized by a molecular arrangement in which the monomers form a so-called "zig-zag pattern". The areal molecular density and the tilt angle of the monomers, however, can vary, which typically leads to the coexistence of different phase domains, e.g. the $(2\sqrt{3}\times\sqrt{3})R30°$ structure (see Figure 2.2 (b)) with a molecular tilt angle of $\gamma \sim 13°$[39] and the $(4\times n)$ structure with $n \sim 8$[39],[40] with a molecular tilt angle of 33-49°[39] (see Figure 2.2 (c)). In this context, an average tilt angle in TPT SAMs on gold of 28° was deduced from *near edge X-ray absorption fine structure* (NEXAFS) data[41]. Overlayer structures of similar packing densities were further observed for 4-biphenyl-derivatized thiols[42].

The geometry of the SAM unit cell, its orientation with respect to the substrate surface, the packing density and the SAM thickness can generally be assessed by microscopic and spectroscopic methods, e.g. STM, *atomic force microscopy* (AFM), XPS, NEXAFS, and *low-energy electron diffraction* (LEED). However, the relative arrangement of the molecules inside

the unit cell and the respective intramolecular configuration, e.g. the inter-ring twist angle γ defining the rotation between the phenyl rings in case of oligophenyl-based SAMs, remains unknown. NEXAFS may provide information on the average tilt angle α of the molecules in oligophenyl-based SAMs[41],[43] but cannot distinguish between different tilt angles adopted in different phase domains. The same applies to XPS which allows for estimating the average tilt angle by determining the thickness of the molecular layer[44], provided that the molecular length is well-known. Closer insight into the molecular packing motifs of biphenylthiolates on Au(111) was recently achieved by Verwüster *et al.* employing *density functional theory* (DFT)[21]. The results indicate, among others, that i) neighboring phenyl rings preferentially adopt a T-shaped arrangement resulting in a herringbone pattern compared to a co-planar situation (this finding is supported by STM data for TPT SAMs on Au(111)[41]), and that ii) the molecules are either almost perfectly planar or strongly twisted with $\gamma \approx 70°$-$80°$.

2.2 Cross-Linking of Aromatic SAMs

Whereas aliphatic SAMs degrade upon electron exposure[45],[46], SAMs from aromatic precursors are laterally cross-linked and converted into monomolecular sheets with extremely high thermal stability[13],[47],[6]. Aromatic SAMs can be employed as negative electron resists in nanolithography applications[48] (but also SAMs from cycloaliphatic precursors have shown performance as negative electron resist[49]) and as building blocks for the fabrication of ultrathin (quasi two-dimensional) materials, i.e. *carbon nanomembranes* (CNMs), providing an innovative technology in the field of membrane separation[1],[2],[9]. This section focuses on molecular mechanisms of cross-linking as well as on electron irradiation-induced structural and chemical modifications of aromatic SAMs.

2.2.1 Molecular Mechanisms

Cross-linking of aromatic SAMs can be achieved by irradiation with electrons[48],[11],[50],[13], He^+ ions[51], or UV light[52]. Both *primary electrons* (PEs) with kinetic energies of typically 50-100 eV and the low-energy *secondary electrons* (SEs) emitted from the substrate were identified to contribute to cross-linking[53],[54],[13],[1],[14],[55]. Cross-linking starting with *electron attachment* (EA) can be described by the reaction route depicted in Figure 2.3. (a) An incoming electron of low kinetic energy is attached to a phenyl unit of a SAM molecule to form a

transient negative ion (TNI), that is, the incident electron becomes temporarily trapped in the vicinity of the target molecule, e.g. the *biphenylthiol* (BPT). (b) The TNI may decay via a number of different channels, among which the abstraction of (anionic) hydrogen through the dissociation of C–H bonds and quenching of the electronically excited $C–H^*$ state through interaction with the induced image dipole at the metal surface are two dominating decay channels. In the first case, the remaining radicalized carbon center may further react with an adjacent molecule in forming an intermolecular, covalent carbon-carbon bond; a process which is accompanied by some significant conformational and orientational molecular disordering which gives rise to the amorphous molecular structure of the monolayer at the final stage of cross-linking.

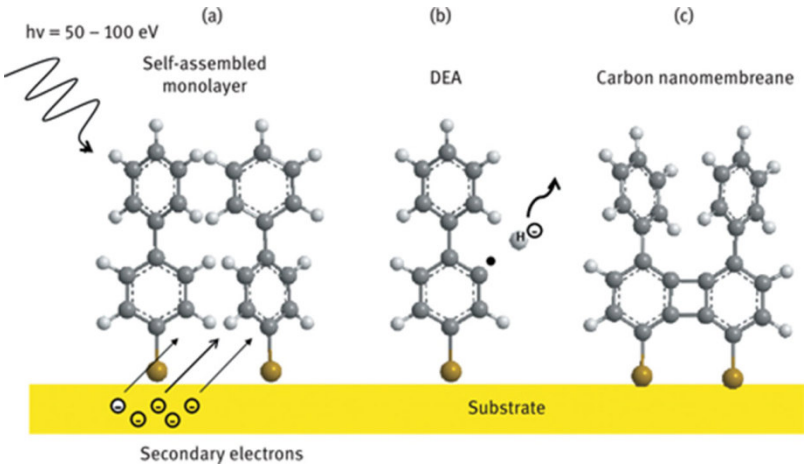

Figure 2.3: Schematic representation of cross-linking in biphenylthiol-based SAMs, involving (a) electron attachment to phenyl units, (b) dissociation of C–H bonds, and (c) formation of intermolecular covalent carbon-carbon bonds. *Reprinted from ref [1]. Copyright (2017) Walter De Gruyter GmbH.*

Low-energy (< 10 eV) electron-induced cross-linking of TPT SAMs on Au(111) was investigated by Amiaud *et al.* employing *high resolution electron energy loss spectroscopy* (HREELS)[14]. The excitation function of the energy loss at 378 meV, attributed to the $\nu(C–H)_{ph}$ stretching mode, exhibits a maximum at 6.0 ± 1.5 eV. Based on the observed aromaticity loss of 47-53 % upon 6 eV electron exposure with a dose of 50 electrons per monomer, a radical chain reaction mechanism going along with aromaticity loss was proposed. This mechanism is schematically shown in Figure 2.4. Individual chain reactions are initiated by EA at 6 eV. The resulting TNIs decay either via electronic rearrangement (without hydrogen loss), leading to the creation of a negatively charged carbon centre next to a radical carbon centre (route A), or via *dissociative electron attachment* (DEA) process going along with the release of an hydrogen ion and the creation of a radicalized carbon center (route B). Therefore,

the first radical is created upon EA. The chain reaction propagates as the radicalized phenyl rings are free to react with adjacent phenyl rings, generating new radicals which in turn generate new radicals and so on. Every involved monomer is subject to rehybridization of two carbon centers from sp^2 to sp^3. The efficiency of the propagation processes is thereby increased by the freedom of the radicalized carbon centers to propagate along the respective phenyl rings. Potential mechanisms leading to the termination of those two-dimensional chain reactions were not addressed. Based on the observed loss of aromaticity, which was attributed to the electron irradiation-induced formation of sp^3-hybridized $C–H_x$ groups, a reactive EA cross-section of 1.2×10^{-16} cm^2 was estimated. A partial loss of aromaticity was also observed previously in NEXAFS data for 50 eV electron-irradiated BPT SAMs[13]. However, HREELS data indicates that exposure of TPT SAMs on Au(111) with 50 eV PEs is not accompanied by aromaticity loss[53]. Note that the proposed chain reactions propagate without hydrogen loss. However, cross-linking is accompanied by hydrogen loss[53],[48] and an effective cross-section for hydrogen loss of $\sigma_{H\text{-}loss} = 2.7–4.7 \times 10^{-17}$ cm^2 was calculated[53]. Electron impact ionization was identified to be the major mechanism leading to the loss of hydrogen, with impact electronic excitation contributing only marginally. Reactive processes induced by the low-energy SEs seem to contribute to hydrogen loss with a cross-section estimated as one order of magnitude smaller.

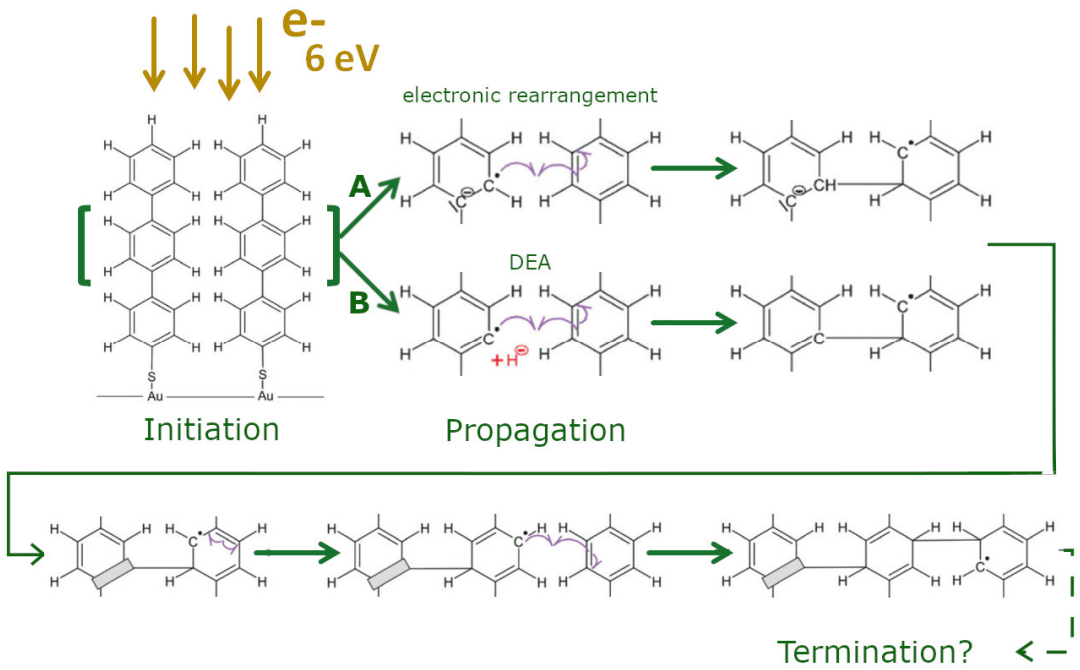

Figure 2.4: Mechanism for electron-induced cross-linking of TPT SAM, proposed by Amiaud *et al.*[14]. Upon electron attachment at 6 eV, the transition negative ion decays via electronic rearrangen ent (route A), leading to the creation of a negatively charged carbon centre next to a radical carbon centre, or via DEA process (route B), accompanied by the release of an hydrogen ion. Both routes lead to the formation of a radical carbon centre, thus initiating the radical chain reaction. As the radical carbon centers can propagate along the respective phenyl ring, the propagation can proceed until being terminated (the termination mechanism is not addressed in this publication). Note that the chain reaction mechanism is accompanied by a partial loss of aromaticity due to the partial rehybridization of the carbon centers from sp^2 to sp^3. *Reprinted and adapted with permission from ref [14]. Copyright (2013) Royal Society of Chemistry.*

Furthermore, it was found by Tai *et al.* employing NEXAFS using partial electron yield acquisition mode[56] that dehydrogenation predominantly occurs close to the SAM-ambient interface, far away from the metal substrate. This is explained by quenching of the electronically excited C–H* state through interaction with the induced image dipole at the metal surface. With increasing separation from the metal surface, the efficiency of the dehydrogenation process is significantly enhanced.

2.2.2 Modification of the Sulfur-Gold Interface

XPS data indicates that the exposure of aromatic thiol-derived SAMs on Au(111) with 50 eV electrons causes a partial cleavage of S–Au bonds[15],[13], accompanied by the formation of a new sulfur species (nSs) that can be assigned to organosulfides (R–S–R), organodisulfides (R–S–S–R), thiols (R–S–H) or thiolate dimers (RS–Au–SR) [13]. The ratio between the nSs signal and the RS–Au signal was found to increase gradually with increasing electron dose until saturation at ~0.7 at a dose of ~50 mC/cm². Angular-resolved XPS measurements indicate that

the nSs may be incorporated into the carbonaceous matrix. S–Au bond cleavage may be slowed by cross-linking of the aromatic network[13]. For TPT SAM on Au(111), the cross-section of the S–Au bonds to undergo bond cleavage upon 50 eV electron exposure amounts to $1.7 \pm 0.3 \times 10^{-17}$ cm², as derived from XPS data[15].

2.2.3 Structural and Chemical Modifications upon Cross-Linking

The progressive broadening of the C1s XP signal indicates both the reduction of the molecular conformational and orientational order of the monolayer and the modification of the electronic structure of the carbon centers upon electron exposure[13],[57]. The reduction of the long-range molecular order upon electron exposure was further verified on the molecular level for BPT SAMs on Cu(111) employing STM and LEED[58]. NEXAFS measurements further indicate an increased downward tilting of BPT molecules on Au(111) upon cross-linking, with tilt angles of ~31° (pristine SAM) and ~41° (after cross-linking). Earlier studies have shown that the irradiation of biphenyl-based aromatic SAMs with electrons may lead to a marginal desorption of carbonaceous material, hence leaving the carbon content mostly preserved[59],[48],[54]. For TPT on Au(111), the irradiation with electrons (100 eV, 60mC/cm²) led to a reduction of the carbon content by 4%[11], as seen from the intensities of the XPS C 1s and Au 4f photoelectron signals. HREELS measurements have shown[53] that the carbon content is conserved upon 50 eV electron irradiation up to a dose of 9.5 mC/cm², within the restriction of accounting for a carbon content variation of a few percent. Moreover, ring opening accompanied by the formation of aliphatic C=C bonds could not be excluded. Beside lateral cross-linking, electron exposure may affect the monolayer-ambient interface[60].

2.2.4 Formation of Molecular-Dimension Pores

More recently, the morphology of a cross-linked TPT monolayer (100 eV, 50 mC/cm²) on Au(111) was characterized by AFM[9], revealing its amorphous and porous molecular structure by indicating the presence of "nano-voids". The void diameter is estimated to an upper limit of 0.7 ± 0.2 nm. The presence of molecular-dimension pores may explain the capability of CNMs made from TPT precursors to filtrate water molecules and helium atoms[9]. The measured pore size is supported by an estimation of pore sizes from classical flow models[9]. Understanding the membrane molecular structure is of particular interest in order to tune their filtration properties.

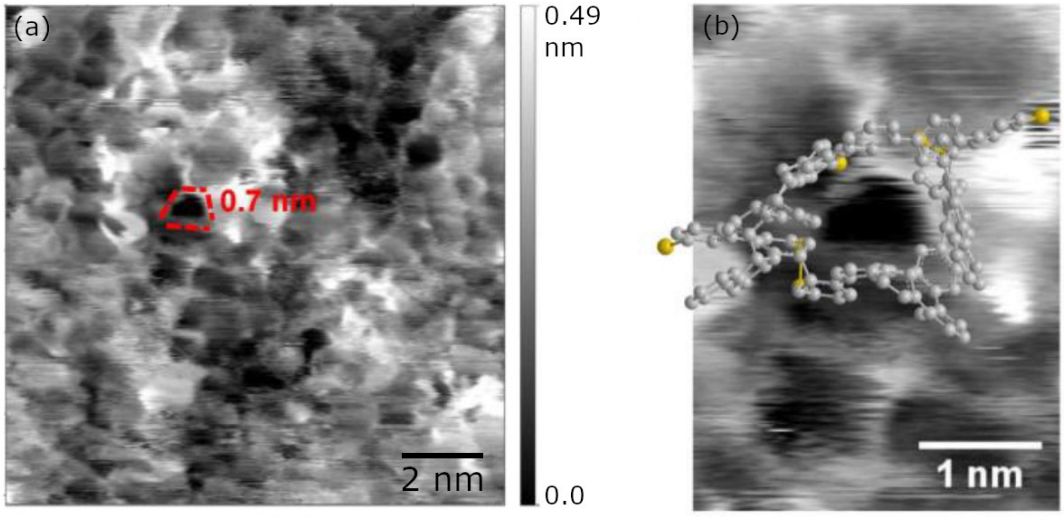

Figure 2.5: (a) AFM image of a TPT CNM measured at 93 K under UHV conditions. (b) Drawing of the pore marked in (a) by Chemdraw software (PerkinElmer Informatics). *Reprinted and adapted with permission from ref [9]. Copyright (2018) American Chemical Society.*

2.2.5 Density Functional Theory Modeling

Computational modeling of cross-linking is, due to its high complexity, a challenging task. Numerous parameters are to be taken into account, involving the dynamics of the hydrogen abstraction process and the resulting change of the intermolecular interaction forces, molecular reorientations during cross-linking, the energetics of the adsorbate-substrate interface, etc. A first-principles investigation of cross-linking within the framework of DFT was performed by Cabrera-Sanfelix *et al.*[61], considering densely-packed BPT molecules on Au(111) as a representative system. The calculations indicate the presence of "graphene-like" nanoflakes after full dehydrogenation and subsequent relaxation, consisting of four fully-dehydrogenated BPT molecules each. Those nanoflakes may constitute building blocks for the molecular structure of the real cross-linked monolayer. A bottleneck of this simulation, however, constitutes the simultaneously triggered abstraction of all H-atoms which does not occur in real samples. However, the formation of a two-dimensional molecular network should require the linkage between respective upper or lower phenyl rings of adjacent molecules[13].

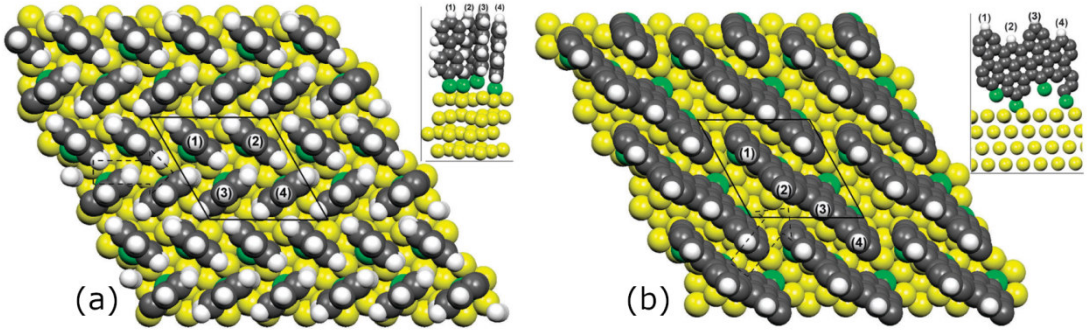

Figure 2.6: (a) pristine BPT SAM adsorbed on Au(111). Inset: side view of the surface unit cell area. (b) Optimized geometry after dehydrogenation of the molecules. Inset: side view of one carbon nanoflake. Sulfur atoms are partially separated from the Au surface. *Reprinted and adapted with permission from ref [61]. Copyright (2010) Royal Society of Chemistry (Great Britain).*

2.3 Scanning Tunneling Microscopy

The development of the STM by Gerd Binnig and Heinrich Rohrer at IBM Zürich Research Laboratory in 1981 paved the way, for the first time ever, to real-space imaging of solid surfaces with atomic resolution. Prior to publishing their work in scanning surfaces by a tunneling current[62], G. Binnig and H. Rohrer reported the first successful tunneling experiment verifying the exponential dependence of the tunneling resistance on the width of the gap, together with Christoph Gerber and Edmund Weibel[63]. The impact of the STM on surface science was recognized quickly by the scientific community. At that time, a large worldwide interest focused on the Si(111) surface 7x7 reconstruction as silicon was and is an important material in the computer industry. The STM with its unprecedented lateral resolution solved the riddle of this surface reconstruction in 1983[62]. Later on, STM contributed significantly to the experimental confirmation of quantum mechanics by visualizing quantum corrals[64]. The achievement of G. Binnig and H. Rohrer in the development of the STM was honored with the Nobel Prize in Physics in 1986. Since the success of the STM, numerous SPM techniques with individual assets and drawbacks have been developed, e.g. *spin-polarized scanning tunneling microscopy* enabling the investigation of atomic-scale magnetism, AFM to perform force measurements, topographic imaging and manipulation, or *kelvin probe force microscopy* (KPFM) enabling the observation of the work function of surfaces with atomic or molecular resolution. These techniques are only a very small part of the growing SPM family constantly opening new doors to nanotechnology.

2.3.1 Topographic Imaging in STM

The operating principle of STM contrasts significantly with related microscopic techniques, i.e. optical or electron microscopy. Instead of a complex lens system which is supposed to guide a beam of light or electrons interacting with the sample surface, a metallic tip of atomic sharpness is used as a pointed measuring probe and brought in tunneling contact with a conducting sample (see Figure 2.7). The separation between tip and sample surface d is typically only a few Ångström units. Applying a voltage U_T between tip and sample generates a tunneling current I_T. By employing piezoelectric actuators (one or more, depending on the construction of the STM) and a measuring and control system, the tip is scanned over the sample surface (x,y) while the tunneling current is monitored and used as a highly distance-sensitive measurement signal. When the STM is operated in the constant-current mode, an integrated feedback loop maintains I_T constant by controlling d; more specifically, the voltage applied to the respective piezo actuator. This technique allows for generating a three-dimensional map $z(x,y)$ of the surface with molecular or even atomic resolution.

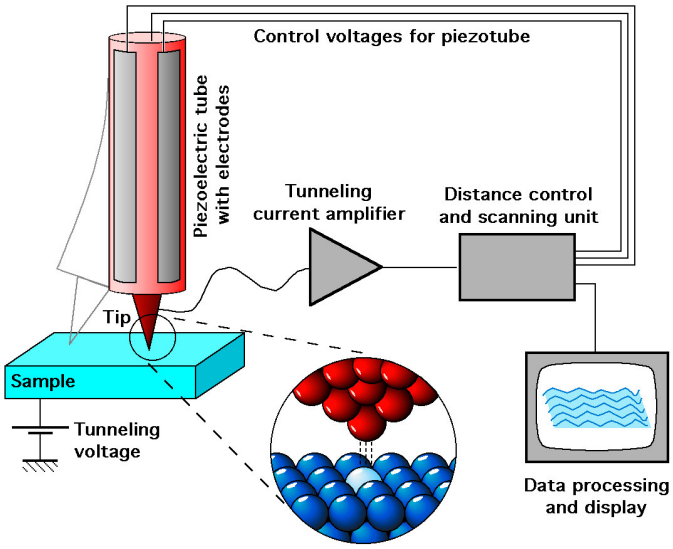

Figure 2.7: Operation principle of scanning tunneling microscopy. A metallic tip of atomic sharpness is used as a measuring probe and brought into tunneling contact. The application of a voltage between tip and sample surface results in a tunneling current being used as measurement and reference signal during image acquisition. The tip is scanned over the sample surface by piezoelectric actuators. In the constant-current mode, the tunneling current is kept constant by controlling the distance between tip and surface, thus enabling the acquisition of three-dimensional surface maps. *Reprinted from ref [65].*

The principle of operation of the STM is based on the quantum mechanical tunneling effect. Therefore, the following section focuses on the simplest case of electron tunneling, that is,

elastic electron tunneling in one dimension. This approximation already explains the extreme sensitivity of the tunneling current to the width of the potential barrier.

2.3.2 Elastic Tunneling in One Dimension

Elastic tunneling of a single electron with kinetic energy E_0 and wave vector $\boldsymbol{k_0}$ through a one-dimensional rectangular potential barrier of height V_0 and width Δz is the most fundamental approach for the theoretical description of tunneling phenomena (see Figure 2.8). The wave nature of microscopic particles, commonly known as *wave-particle dualism*, was first postulated by Louis de Broglie in 1923[66] and later formulated mathematically by Erwin Schrödinger[67] in his popular Schrödinger Equation(s). The wave nature of electrons allows them to traverse potential barriers which are impenetratable from the classical point of view. The overall wave function of the electron is derived from solving the time-independent Schrödinger equations for the three regions (j=I,II,III) and by matching the ψ_j and their first derivatives $\mathrm{d}\psi_j/\mathrm{d}z$ at the discontinuities of the potential $V(z)$. A thorough theoretical background of numerous tunneling processes, including a detailed mathematical description of the present subject can be found in ref [68]. In the wave model of the electron, the incident electron wave ψ_{inc} is split up into a transmitted part of lower amplitude, ψ_{trans} with wave vector $\boldsymbol{k}_{trans}$, and a reflected part (not shown), while the electron energy is being preserved during the (elastic) tunneling process. From the classical point of view, the transmitted part of the electron wave function equals zero. It is to be noted that particles in quantum mechanics are described by wave packets but, for clarification, a sinusoidal electron wave is shown in Figure 2.8. In the particle model of the electron, the electron passes the barrier with a certain transmission probability, which is expressed by the transmission coefficient T. For a strongly attenuating barrier ($\kappa \times \Delta z >> 1$), T shows the following dependency:

$$T \propto \exp(-2\kappa \times \Delta z) \quad \text{with decay rate} \quad \kappa = \sqrt{2m(V_0 - E_0)}/\hbar, \qquad \text{Equation 2.4}$$

where $\hbar$ is the Planck constant, m is the electron mass, and V_0 - E_0 is the effective barrier height.

The same result for the transmission coefficient T was also found by Bardeen in 1961 for metal-insulator-metal tunneling junctions by solving the time-dependent Schrödinger equation with approximate solutions of the exact Hamiltonian and by using Fermi's 'golden rule' of first-order time-dependent perturbation theory[69]. Equation 2.4 reveals the strong sensitivity of the

transmission coefficient T to the barrier width Δz. In typical tunneling experiments involving planar metal-insulator-metal junctions, the effective barrier height amounts to several eV and the barrier width Δz is on the order of Ångström units. Changing the barrier width by 1 Å may result in a change of the transmission coefficient T by one order of magnitude, providing the metrological basis for the development of the STM. The gap width, that is, the distance between the front end of the tip apex and the sample surface, is precisely controlled by a piezo actuator and the tunneling current is employed as controlled variable which is held constant during the scan.

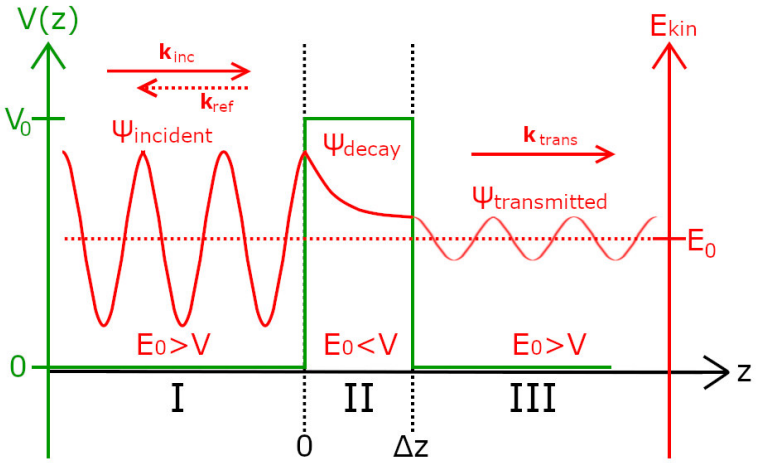

Figure 2.8: Elastic tunneling through a one-dimensional rectangular potential barrier (green). The overall wave function (red) of the incident electron represents the solution of the time-independent Schrödinger equation.

2.3.3 Elastic Tunneling in Planar Metal-Insulator-Metal Junctions

When a small bias voltage U is applied between two metal electrodes separated by an insulating barrier, the Fermi energies $E_{F,i}$ are shifted by $\Delta E = eU$ with respect to each other and electrons can tunnel from an occupied state of the negatively biased electrode through the potential barrier generated by the insulator into a free state of the opposite electrode. As a result, a tunneling current I can be measured. Figure 2.9 shows the potential diagrams of a tunneling junction where electrode 1 with work function Φ_1 is biased negatively with respect to Φ_2 of electrode 2 (a), or electrode 1 is biased positively with respect to electrode 2 (b). The electron tunneling from an occupied state of the first electrode into an unoccupied state of the second electrode is shown in red. The insulating barrier is treated as a vacuum barrier and the effect of an image potential is neglected. The trapezoidal shape of the tunneling barrier (green) in each case is defined by both the applied bias voltage U and, in case of two different metals, from the

difference in the respective work functions Φ_1 and Φ_2. The exponential dependency of the transmission coefficient T on the effective barrier height (see Equation 2.4) is valid in general, independent on the shape of the barrier and therefore, electrons near the Fermi energy of the negatively biased electrode tunnel most effectively (indicated by blue, horizontal arrows) as they experience the lowest energy barrier. For completeness, the *density of state*s (DOS) characterizing the metal electrodes are highlighted for the right electrode by a brown line profile. For the theoretical treatment of STM experiments, the influence of the tip DOS and the sample *local density of states* (LDOS) was considered by Tersoff and Hamann (see below).

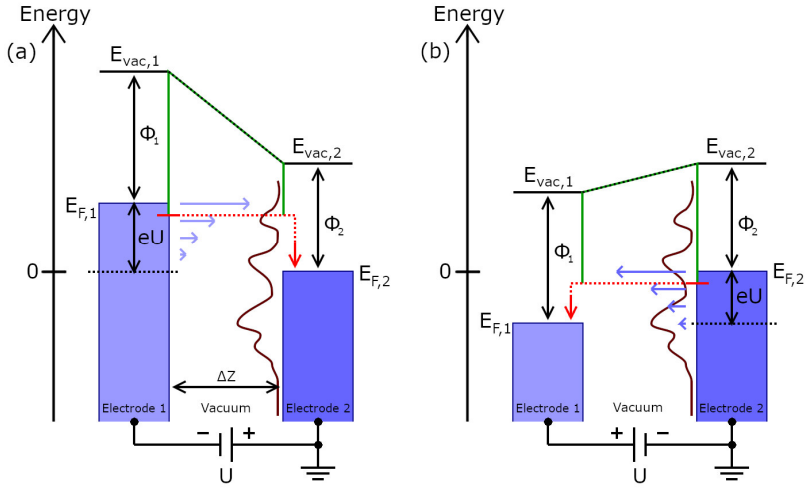

Figure 2.9: Tunneling barrier (green) between two metal electrodes 1 and 2 with work functions Φ_1 and Φ_2 separated by a vacuum gap of width Δz. The electron tunneling from an occupied electronic state of the negatively biased electrode into an unoccupied electronic state of the opposite electrode is shown in red. The horizontal arrows indicate that electrons with high kinetic energies tunnel through the barrier most effectively. The DOS characterizing the metal electrodes (brown line profile) are exemplarily depicted for electrode 2. (a) Electrode 1 is biased negatively with respect to electrode 2. (b) Electrode 1 is biased positively with respect to electrode 2.

In practice, the shape of the tunneling barrier is influenced by the electrode work functions, the material of the insulating barrier and the interaction of the tunneling electrons with the metal surfaces described by the image potential[68], leading to potential barriers with shapes that may deviate from a simple trapezoidal shape. One-dimensional potential barriers of arbitrary shape were treated theoretically by Wentzel, Kramers, and Brillouin in 1926[70],[71],[72]. The WKB approximation constitutes a semiclassical approach in the limit $\hbar \to 0$ and provides an approximate solution for the one-dimensional time-independent Schrödinger equation in case of a potential barrier $V(z)$ with insignificant z-dependency on the scale of the de Broglie wavelength λ of the electron. For this, the tunneling barrier is decomposed in many thin

barriers of rectangular shape and width dz (see Figure 2.10). If the effective potential barrier height is not too small (E_0 << V), the transmission coefficient $T(E)$ is expressed as

$$T(E) = \exp\{-2\int_{Barriere} dz \cdot \kappa(z)\} \quad \text{with} \quad \kappa(z) = \sqrt{2m(V(z)-E)}/\hbar \qquad \text{Equation 2.5}$$

Both Equation 2.4 and Equation 2.5 indicate that electrons with high kinetic energies tunnel through the barrier most effectively.

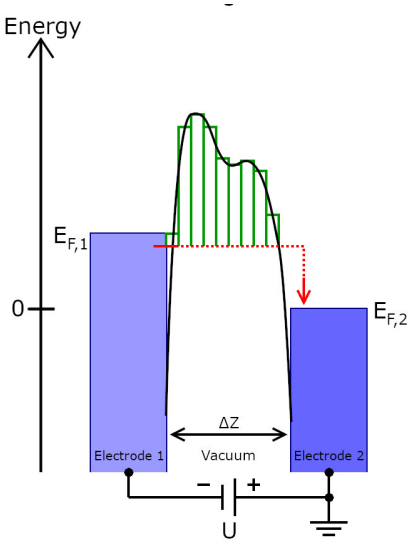

Figure 2.10: Decomposition of the arbitrarily shaped effective potential barrier (black line) for the tunneling electron (red) into rectangular barriers (green).

Elastic tunneling in planar metal-insulator-metal junctions (in thermal equilibrium) was treated theoretically by Simmons in 1963[73]. The calculations involve sin ilar metal electrodes with free-electron behavior. By employing the WKB approximation (see above) and by introducing a mean potential barrier height above the Fermi level E_{F1} of the negatively biased electrode, $\bar{\Phi} = \frac{1}{\Delta z}\int_{z1}^{z2} dz' \cdot \Phi(z')$ with $\Delta z = z_2 - z_1$, the following expression for the tunneling current density J was derived for bias voltages U << $\bar{\Phi}/e$ at zero temperature:

$$J \propto \frac{\sqrt{\bar{\Phi}}}{\Delta z} \cdot U \cdot exp(-2 \cdot \frac{\sqrt{2m\bar{\Phi}}}{\hbar} \cdot \Delta z) \qquad \text{Equation 2.6}$$

The linear dependency of J on the gap voltage U indicates Ohmic behavior at low bias. Similar to the previous equations, an exponential dependency of J on the gap width Δz is found, as well as on the square root of the mean tunneling barrier height.

2.3.4 Tunneling in STM

The major difference between planar tunneling junctions and STM tunneling junctions is the pointed shape of the STM scanning probe which allows for acquiring images with extraordinarily high lateral resolution. Already Equation **2.4** indicates that the tunneling current I majorly originates from the very front end of the scanning probe. This is a fundamental property of tunneling contacts. Thus, the origin of the tunneling current can be localized on the sample surface (x,y) in an extremely precise manner. However, the three-dimensional shape of the scanning probe makes the mathematical derivation of the tunneling current more complex. Moreover, in practice typically neither the atomic structure of the tip very near the sample surface nor the tip wave functions contributing to the tunneling process are known. In conventional STM experiments, the tip is typically subject to recurring modifications during the scan, making its exact characterization prior to experiments not practicable. In 1961, Bardeen derived the following expression for the tunneling current I in first-order time-dependent perturbation theory[69]:

$$I = \frac{2\pi e}{\hbar}\sum_{t,s}\{f(E_t) - f(E_s + eU)\} \cdot |M_{ts}|^2 \cdot \delta(E_s - E_t) \qquad \text{Equation 2.7}$$

where $f(E)$ is the Fermi function, U the bias voltage, M_{ts} is the tunneling matrix element between the unperturbed electronic states ψ_t of the tip and ψ_s of the sample surface, and E_t and E_s are the energies of the states ψ_t and ψ_s in the absence of tunneling.

In this formalism, the matrix element M_{ts} is given by

$$M_{ts} = -\frac{\hbar^2}{2m}\int d\boldsymbol{S} \cdot (\psi_t^* \nabla\psi_s - \psi_s \nabla\psi_t^*) \qquad \text{Equation 2.8}$$

where the integral is to be evaluated over a random surface separating the STM tip and the sample surface.

As the wave functions of tip and sample surface are typically unknown, further theoretical treatment requires the assumption of a model wave function. Tersoff and Hamann (1983, 1985) assumed the very front part of the tip to be of spherical geometry with effective radius R (see Figure 2.11)[74],[75]. The strong dependency of the tunneling current on the width of the potential barrier (see Equation 2.6), that is, an increase of the barrier width by one Ångström may lead to a decrease of the tunneling current by one order of magnitude, makes it reasonable to assume that the major part of the tunneling current results from the very front part of the tip

and that the overall tip geometry can be neglected. Therefore, assuming spherical tip geometry of radius of curvature *R*, with its center of curvature at $\boldsymbol{r_0}$, is reasonable (see Figure 2.11). The distance between the front end part of the tip and the sample surface is *d*. Tersoff and Hamann modeled the tip by an s-type wave function, neglecting all contributions from tip wave functions with angular dependence with orbital number $l \neq 0$.

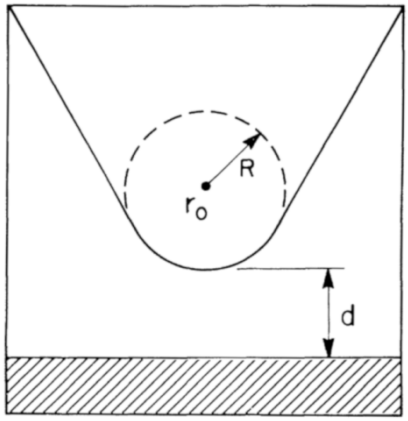

Figure 2.11: Schematic illustration of the tunneling geometry. The tip geometry is assumed locally spherical with radius of curvature *R* and center of curvature at $\boldsymbol{r_0}$. The distance between the front end of the tip and the sample surface (shaded) is *d*. *Reprinted with permission from ref [74]. Copyright (1998) American Physical Society.*

In the limit of low temperature *T* and small applied bias voltage *U*, the following dependency of the tunneling current was obtained:

$$I \propto U \cdot \exp(2\kappa R) \cdot n_t(E_F) \cdot n_S(E_F, \boldsymbol{r}_0) \qquad \text{Equation 2.9}$$

where $n_t(E_F)$ is the density of states of the tip at the Fermi level, $n_s(E_F,\boldsymbol{r_0})$ the LDOS of the sample surface at the Fermi level evaluated at the center of curvature $\boldsymbol{r_0}$ of the tip, and $\kappa = 2m\Phi/\hbar$ is the decay rate where Φ is the effective local potential barrier height.

Following the formalism by Tersoff and Hamann, the STM tunnel junction shows ohmic behavior at low bias (if $\boldsymbol{r_0}$ = constant). The influence of the electronic structure of the scanning probe can be neglected. The proportionality of the tunneling current to the LDOS of the sample surface implies that the STM images, if acquired in constant current operating mode, reflect contour maps of constant surface LDOS at the Fermi level, evaluated at the center of curvature $\boldsymbol{r_0}$ of the tip. For metals with a simple electronic structure, this contour map approximates the actual sample topography. However, Equation 2.9 is only valid at low bias voltage and in case that only one s-type wave function and no tip wave functions with angular dependence (l = 1,2, …) contribute to the tunneling current. A finite bias voltage may lead to a

distortion of the tip and sample surface wave functions ψ_t and ψ_s as well as to a distortion of the respective energy eigenvalues E_t and E_s[76]. In a first approximation, that is, by using the undistorted (zero-voltage) tip and sample surface wave functions and energy eigenvalues, by neglecting image potential effects and the influence of the electrodes' band structure on the tunneling probability, the tunneling current can be expressed as

$$I \propto \int_0^{eU} dE \cdot n_t(\mp E \pm eU) \cdot n_s(E) \cdot T(E, eU) \qquad \text{Equation 2.10}$$

with transmission coefficient

$$T(E, eU) = exp\{-2(d+R)\kappa\} \text{ with } \kappa = \sqrt{\frac{2m\Phi_{eff}}{\hbar^2}} \quad \text{and } \Phi_{eff} = \frac{\Phi_t + \Phi_s}{2} + \frac{eU}{2} - E \qquad \text{Equation 2.11}$$

where Φ_{eff} is the reduced effective barrier height. Depending on the polarity of the bias voltage, electrons can tunnel from occupied electronic states of one electrode (tip or sample) into unoccupied electronic states of the opposite electrode. The energy-dependency of the decay rate κ is a result of the WKB approximation. The exponential dependency of the transmission coefficient T is in agreement with Equation **2.4**, Equation 2.5 and Equation 2.6 and results from the fact that the LDOS of the sample surface at the Fermi level, $n_s(E_F)$, decay exponentially in the z direction normal to the surface towards the vacuum ambient:

$$n_S(E_F, z) \propto \exp(-2\kappa z) \qquad \text{Equation 2.12}$$

The effective lateral resolution of the STM was estimated geometrically by Tersoff and Hamann[74],[75] under consideration of the exponential dependency of the transmission coefficient (see Equation 2.11) a spherical model tip of radius R (see Figure 2.11) to

$$L_{eff} = 1.66 \cdot \sqrt{\frac{R+d}{\kappa}} \qquad \text{Equation 2.13}$$

Assuming a tip-sample distance of $R + d = 1$ nm and a sample work function Φ of 5 eV, the lateral resolution is about 4-5 Å. This relation indicates that L_{eff} is defined by the gap width d in case of a sharp tip ($R << d$) and by the radius of curvature R in case of rather blunt tips ($R >> d$). However, geometrically approximating the STM lateral resolution is only reasonable for larger surface corrugations such as the reconstruction of metal surfaces, e.g. Au(100) 5×1 and Au(110) 2×1 with surface periodicities of ~14 Å and 8.2 Å, respectively.

Wiesendanger *et al.* have shown[77] that the resolution of the STM can be significantly higher than predicted within the s-wave tip model by measuring the atomic surface structure of Au(111) exhibiting corrugations < 3 Å. Understanding the underlying mechanism requires a more detailed modeling of the STM tip. Chen[78],[79] found that the atomic orbital at the front end of the tip has strong impact on whether atomic corrugations can be resolved or not. In particular, the experimentally observed atomic corrugation of Al(111) is explained by assuming a d_{z^2} tip state, whereas an s tip state would only provide LDOS contrast without atomic resolution. In particular, tungsten STM tips are predominantly characterized by p_z and d_{z^2} states at the tip apex[78],[80]. Tunneling through electronic tip states with angular dependency is described by the 'derivative rule' developed by Chen[80]. Following Chen's formalism, the tunneling matrix element M for p_z and d_{z^2} tip states are proportional to the respective z derivatives of the surface atom wave functions $\partial\psi/\partial z$ and $\partial^2\psi/\partial z^2$, evaluated at the center $\boldsymbol{r_0}$ of the tip apex. Therefore, the observed corrugations in constant-current STM images involving tip states with angular momentum (l = 1, 2, …) generally do not represent contour maps of constant LDOS at E_F of the sample surface, as derived from the calculations of Tersoff and Hamann for *s*-type tip states, but contour maps of constant conductance distribution $\sigma(\boldsymbol{r}) = \sigma_0$. It is clarified by the 'reciprocity principle' in STM by Chen[78] that the STM tip apex generally does not image the actual electronic structure of the sample surface. If the tip state and the sample surface states are of different angular momentum, interchanging the tip and sample surface states would not affect the contours of constant conductance $\sigma(\boldsymbol{r}) = \sigma_0$ and therefore lead to similar patterns in constant-current STM images (see Figure 2.12).

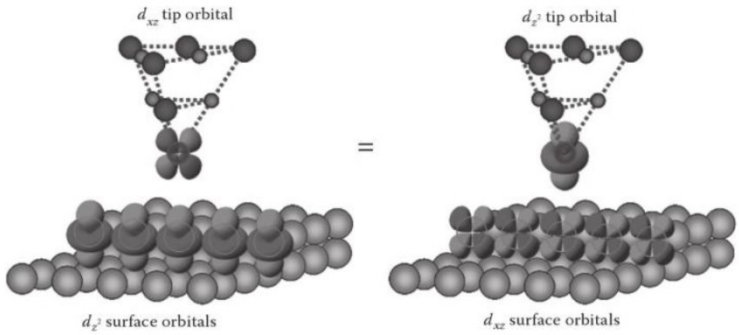

Figure 2.12: Schematic illustration demonstrating the 'reciprocity principle' by Chen. Interchanging the tip and sample surface states would yield a similar contour pattern. *Reprinted from ref [81].*

The contribution of non-*s*-type tip states can explain the unexpectedly high atomic corrugation amplitude on the Au(111) surface observed by Hallmark *et al.*[82] which is about two orders of magnitude higher than predicted by the theory of Tersoff and Hamann by assuming an *s*-type

tip state. Recent studies have demonstrated the possibility to reproducibly probe and select different *d*–orbitals of a single crystalline tungsten tip in a controlled manner[83] (see Figure 2.13). This was performed by employing the localized carbon orbitals of the HOPG surface atoms. The experimental results, being supported by DFT calculations, demonstrate the capability of the STM to achieve sub-ångström lateral resolution (at zero temperature), thereby breaking through the resolution limit proposed by Tersoff and Hamann.

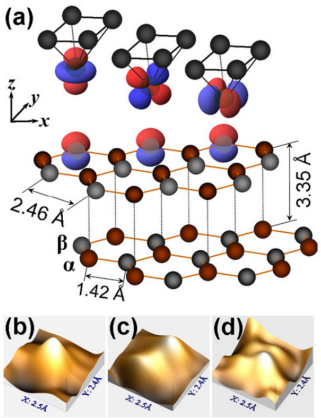

Figure 2.13: Schematic view of a W(001) tip with the $d_{3z^2-r^2}$ (left), $d_{xz,yz}$ (center), or $d_{x^2-y^2}$ (right) orbital at the apex above the graphite surface. (b)-(d) Pseudo 3D images of the atomic features measured with W(001) tips and predominant contribution of the displayed tip orbitals. *Reprinted with permission from ref [83]. Copyright (2010) Europhysics Letters.*

2.3.5 Preliminary Considerations on the Effect of Cross-linking on the STM Image Contrast

To specify the origin of the STM image contrast of isolated adsorbates or even adsorbate layers on metallic surfaces is a complex issue. STM does not simply measure the topography on a sample surface. Instead, manifold parameters influence the image contrast, e.g. the nature of the scanning probe frontal atomic orbital, the modulation of the sample work function by polarizable molecular adsorbates, the electronic structure of the adsorbates; in particular which electronic states predominantly contribute to the image contrast, the local electronic properties of the sample surface (LDOS), the tip-surface separation, mechanical and electrostatic tip-surface interactions, the applied bias voltage, etc. The electronic structure of adsorbates may further be altered by changes in molecular conformation and packing[84]. In particular, adsorbates can appear as peaks or valleys or even be completely invisible, depending on the applied bias voltage and on whether their presence increases or decreases the LDOS of the sample surface[85],[86]. "For the imaging of adsorbates with the STM, it is not correct to say that the microscope images the adsorbate, or that it images the adsorbate perturbed by its

interaction with the substrate. The microscope in fact probes the adsorbate and the substrate, both perturbed by their mutual interaction" (see: Sautet 1997, p.1115)[87].

The accurate interpretation of STM images which show partially cross-linked TPT monolayers on Au(111) therefore requires a prior discussion of how the appearance of cross-linked monolayer areas in (constant-current) STM images may differ from pristine ones; more specifically, how cross-linking may affect the STM image contrast. For this it is reasonable to consider the findings in previous studies on how cross-linking affects the charge transport and the electronic transport properties through the molecular layer. In this context, the relative contributions of cross-linking of the carbonaceous matrix and the modification of the S–Au interface to the (constant-current) STM image contrast should be discussed and, in particular, if both kind of modifications can be distinguished in the STM images. Cross-linking of SAMs made from oligophenyl derivatives significantly affects the charge transport through the monolayers. Penner *et al.*[88] investigated the charge transport through molecular junctions incorporating pristine and cross-linked SAMs (100 eV, 50 mC/cm²) of oligophenylthiols of different molecular length (phenylthiol, biphenylthiol, *p*-terphenylthiol, and *p*-quaterphenylthiol), employing an eutectic Ga-In (EGaIn) top electrode and the Au(111)/mica substrate as bottom electrode. It was found that the tunneling junction incorporating the cross-linked layer is characterized by an increase of the (low-bias) tunneling resistance *R* upon cross-linking by 1-2 orders of magnitude (also observed by Yildirim *et al.*[89]) which could be accounted for by the enhanced tunneling barrier at the Au/monolayer interface and the partial loss of aromaticity compared to the pristine monolayer. This indicates that locally cross-linked spots in the monolayer appear as depressions in STM images (see Figure 2.14). This hypothesis is supported by Zhang *et al.*[90] employing *conductive probe atomic force microscopy* (CP-AFM) yielding current images acquired at a bias voltage of 100 mV of a patterned monolayer consisting of pristine and cross-linked 4′-nitro-1,1′-biphenyl-4-thiol (NBPT) monolayer areas (patterned by shadow mask in close proximity to the monolayer during electron irradiation), revealing that the tunneling current is decreased in the cross-linked areas.

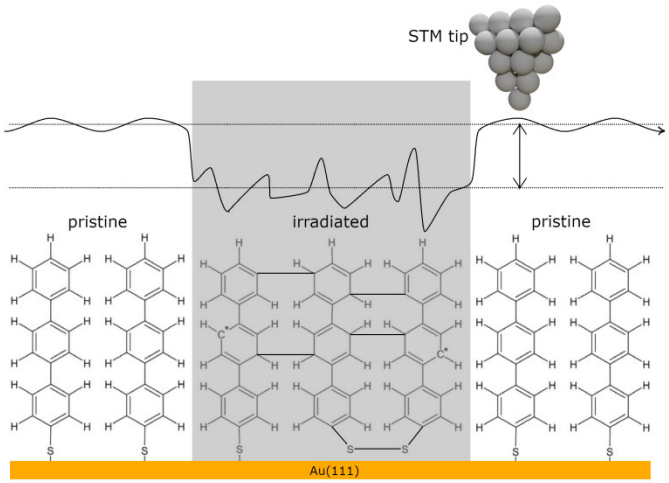

Figure 2.14: Expected appearance of locally cross-linked spots within the TPT layer in STM images. Cross-linked areas are expected to appear as depressions in STM images, due to the strong increase of the tunneling resistance *R* upon cross-linking (see text for details). Structural disordering upon cross-linking might be accompanied by a loss of molecular resolution, as indicated by the black line representing the STM tip trajectory. The relative contributions of the modification of the carbonaceous matrix and the modification of the sulfur-gold-interface are discussed in the text.

More precisely, Penner *et al.* have shown that the contact resistance R_0 as extracted from the intercept from *R*-*d*-curves (*R*: low-bias (±0.1 V) tunneling resistance, *d*: monolayer thickness) increases by 1-2 orders of magnitude which is accounted for by a modified interfacial electronic structure at the monolayer/Au interface. This observation is supported by Yildirim *et al.*[89] showing that cross-linking (50 eV, 40 mC/cm²) leads to an increase of the work function by ~ 200 meV which could be a result of the partial cleavage of the S–Au bonds after cross-linking and is expected to cause an increase of the tunneling barrier. In this context it is known that the interface dipole of SAMs can be used to tune metal work functions[91],[92]. Charge transfer between the adsorbates and the substrate surface may lead to the formation of an electric dipole layer and therefore to a modification of the work function. It is therefore expected that the modification of the S/Au interface upon cross-linking contributes strongly to the STM image contrast.

The dependency of *R* on the molecular length was quantified by Penner *et al.* by using the relation $R \propto R_0 \times \exp(\beta^R d)$, where β^R denotes the decay constant. β^R does not change significantly upon cross-linking, yielding values of 0.50 ± 0.05 Å^{-1} for the pristine and 0.53 ± 0.05 Å^{-1} for the cross-linked monolayer, indicating that cross-linking of the carbonaceous matrix contributes only marginally to the STM image contrast. Moreover, due to the relatively low bias voltages employed in the experiments for this thesis ($|U| < 1.2$ V), no molecular levels should mediate the tunneling current directly in terms of resonant tunneling.

The energy gap between the *highest occupied molecular orbital* (HOMO) and the *lowest unoccupied molecular orbital* (LUMO) for the pristine TPT film was determined by Kong *et al.*[93] using DFT calculations, yielding a value of 4.1 eV (4.4 eV was specified by Houplin *et al.*[94]). The energy of the LUMO orbital is 2.1 eV above the Fermi level. Schematic energy diagrams for the respective tunneling situations are shown in Figure 2.15. The calculated ground state molecular orbital energies and their positions are shown (brown, horizontal lines). For high bias voltages with respect to the LUMO (a), resonant tunneling is to be considered. For low bias voltages (b), no molecular orbitals should contribute to the tunneling current directly. However, a reduction of the HOMO-LUMO gap upon cross-linking may occur. It was shown in case of [1,1';4',1''-terphenyl]-4,4''-dimethanethiol SAMs on Au that electron irradiation (50 eV, 54 mC/cm²) results in a reduction of the HOMO-LUMO gap from 6.8 eV to 5.9 eV[95]. For TPT SAMs, this may lead to the contribution of additional tails of molecular orbital resonances to the STM image contrast through resonant tunneling and therefore, cross-linked areas within the molecular layer should appear brighter compared to the pristine areas. Moreover, taking into account the decrease in aromaticity, more broadened molecular orbitals are expected[88].

In conclusion, locally cross-linked spots within the TPT layer should appear as depressions in constant-current STM images, due to the strong increase of the tunneling resistance R upon cross-linking. As the increase of R is primarily caused by the increase of the contact resistance R_0, it is further expected that the major contribution to the STM image contrast results from the modification of the S–Au interface. Cross-linking of the carbonaceous matrix, however, is expected to contribute only marginally to the contrast as the decay constant. β^R does not change significantly after cross-linking. Though the reduction of the HOMO-LUMO gap might lead to the contribution of additional tails of molecular orbital resonances to the tunneling current, the strong increase of the tunneling resistance R upon cross-linking strongly indicates that locally cross-linked spots within the TPT layer appear as depressions in STM images.

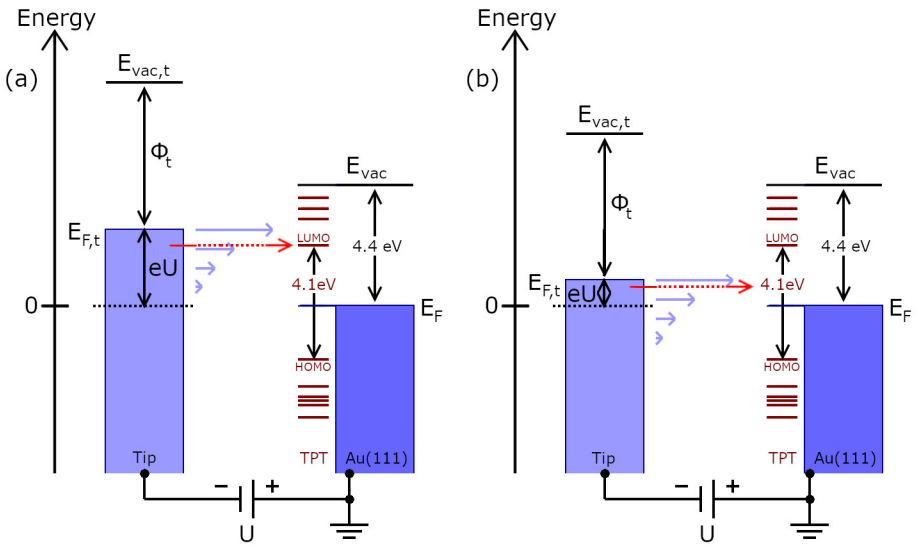

Figure 2.15: Schematic energy diagrams for a TPT SAM on Au(111) measured by STM. The calculated (DFT) ground state molecular orbital energies (brown, horizontal lines) and their positions were obtained from Kong *et al.*[93]. (a) The applied bias voltage is high enough to allow for resonant tunneling through the LUMO. (b) Due to the low bias voltages applied in the experiments of this thesis, no resonant tunneling through molecular orbitals is expected. However, the contribution of additional tails of molecular orbital resonances to the STM image contrast through resonant tunneling cannot be excluded.

2.4 X-Ray Photoelectron Spectroscopy

The illumination of a material surface with photons of sufficient energy causes the emission of electrons, so-called *photoelectrons*. This kind of interaction of radiation and matter is referred to as *photoeffect* and was explained for the first time by Albert Einstein in 1905[96] on the basis of Max Planck's law of black-body radiation[97]. When a photon of energy $h\nu$ hits an electron with characteristic binding energy E_B, the electron can be released from its bound state and be ejected from the material surface. The kinetic energy of the photoelectron, E_K, is expressed as

$$h\nu = E_K + E_B + \Phi, \qquad \text{Equation 2.14}$$

where Φ is the work function of the material, in the case of solid. When using monochromatic light of well-known energy, this law allows for the spectroscopic identification of elements by their characteristic binding energy.

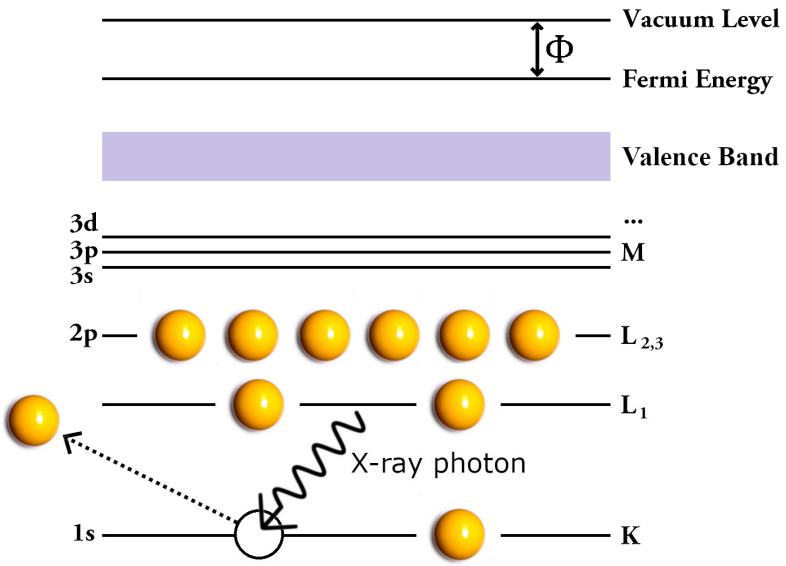

Figure 2.16: Schematic representation of the XPS photoemission process. X-ray photons can eject core-level electrons; their binding energy is characteristic for the respective element.

By employing high-energy X-ray light, the core-level electrons can be accessed. They appear as intensity peaks in the energy spectrum of the emitted photoelectrons and constitute a signature of the respective elements forming the material. Quantitative analysis of the relative concentrations is achieved by measuring the relative peak intensities, in consideration of the respective atomic cross-sections for photoionization σ_i for element i (Scofield factor)[98].

XP spectroscopy with sufficient high resolution further allows for the analysis of the chemical state of the elements. The binding energy of a core electron depends on the local chemical (and physical) environment of the atom. This effect is commonly referred to as *chemical shift* of the respective intensity peak in the XP spectrum. For BPT SAMs on Au(111), in particular, the binding energy of the carbon atoms bound to the sulfur anchor groups is shifted by $\Delta E \sim 0.9$ eV with respect to the carbon atoms constituting the molecular backbones[13]. The quantification of ΔE can therefore be attributed to the presence of particular chemical bonds.

A special attribute of XPS is its surface sensitivity, making it ideal for surface analysis purposes. This sensitivity results from the fact that the electrons loose energy in inelastic scattering events with atoms. Therefore, the intensity peaks in the XP spectra are mostly generated by atoms near the surface, whereas the background comes from subjacent atoms whose emitted electrons underwent (multiple) inelastic scattering events before leaving the sample surface. The attenuation of the electrons with intensity I_0, emitted from a depth d below the surface, is expressed according to the Beer-Lambert law as

$$I_S = I_0 \exp\left(-\frac{d}{\lambda}\right) \qquad \text{Equation 2.15}$$

Here, λ denotes the *inelastic mean free path* (IMFP) of the electrons inside the material. It depends on the kinetic energy of the photoelectron and the material itself. However, universal dependencies for elements, organic and inorganic compounds and adsorbed gases were discovered by Seah *et al.*[99]. The typical escape depth of non-scattered photoelectrons is 1-10 nm.

XPS further allows for determining the layer thickness *t* of the monolayer from the attenuation of a substrate photoemission signal with preferably high intensity. For this method, a bare reference substrate sample is required. The layer thickness *t* can be calculated according to[100]:

$$I_d = I_0 \times e^{-\frac{t}{\lambda cos\Theta}} \qquad \text{Equation 2.16}$$

where I_0 and I_d are the photoemission signals from the reference sample and the monolayer-covered substrate, respectively. Θ is the emission angle and λ is the attenuation length of the chosen substrate photoemission signal. For this thesis, the monolayer thickness was calculated by employing the Au $4f_{7/2}$ signal. The attenuation length λ employed amounts to 36 Å[52].

3 Materials and Methods

This chapter provides background information about the molecular and electronic structure of the TPT precursors and how TPT SAMs on Au(111) on mica were prepared from solution and from the gas phase. Most experiments for this thesis were performed on the Omicron Multichamber UHV system (excluding SAM preparation from solution). The modular design of this system will be explained. Afterwards, technical details about the surface analytical instruments, XPS and STM, are given and how the data was processed and evaluated after acquisition. Monolayers were cross-linked either by using the rastering electron beam of a SEM or by using an in-situ electron floodgun. Both procedures are described in detail. In some experiments, the STM/SEM combination system was employed to irradiate a distinct area of a monolayer with electrons and to acquire STM data of the respective surface location immediately before and after electron irradiation. All steps involved in this procedure will be described in detail.

3.1 Materials

3.1.1 Molecular Precursors

The *p*-terphenyl (TPT, HS-$(C_6H_4)_2$-C_6H_5) precursor molecules were purchased from Sigma-Aldrich. A schematic drawing of the molecules is shown in Figure 3.1 (a). Each of the three planar phenyl rings forming the terphenyl spacer has a rotational degree of freedom about the main molecular axis. It is reasonable to assume that the rotation of the phenyl rings is of particular importance for the TPT molecules to form intermolecular bonds in two dimensions. Two stable twisted conformations of the free molecules were found by employing DFT calculations[101], differing mainly by the twisting angles between the successive planar phenyl rings (see Figure 3.1 (b1),(b2)). The twisting angles were respectively associated to the couples of angles (ϕ_1,ϕ_2) = (+41.0°,+41.8°) and (+41.9°,-43.2°), taking the central phenyl ring as reference and ϕ_1 referring to the thiol substituted ring. An upper value for the rotation barrier separating the two stable conformations upon variation of the twisting angle ϕ_2 of 110 meV was found. The distance between the sulfur and the terminal carbon atom amounts to ~13.2 Å.

The HOMO and LUMO orbitals along with their energy positions with respect to the vacuum level (HOMO: -5.28 eV, LUMO: -1.23 eV) were determined using DFT[93].

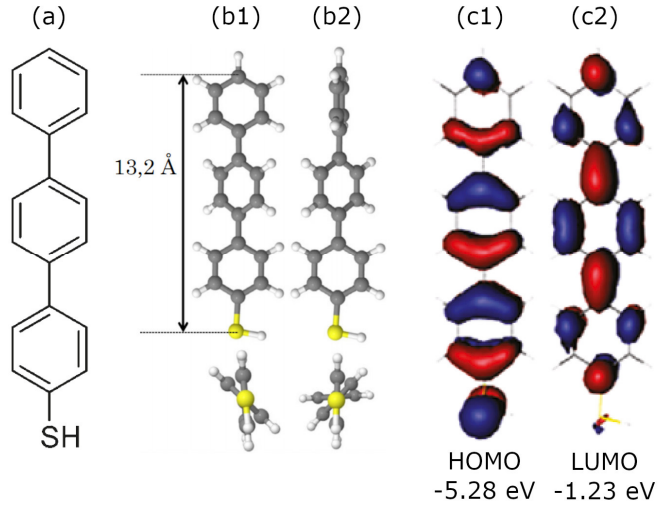

Figure 3.1: (a) Structure of the TPT molecule. (b) Dimension and calculated (DFT) stable conformations of comparable energies of the TPT molecule, differing mainly by the twisting angles between the successive planar phenyl rings (c1),(c2) Calculated (DFT) HOMO and LUMO orbitals, along with their energy positions with respect to the vacuum level. *Part b is reprinted and adapted with permission from ref [101]. Copyright (2015) Springer Nature. Part c is reprinted and adapted with permission from ref [93]. Copyright (2011) American Chemical Society.*

3.1.2 Substrates

Au(111) on mica has been the common substrate for the preparation of CNMs from TPT precursors[9]. This surface provides a high resistance to adsorption of contaminants or surface oxidization. SAMs were prepared on commercially available, 300 nm thermally evaporated Au(111) on mica substrates (Georg Albert PVD, Silz, Germany), fabricated by means of physical vapor deposition (PVD). These substrates provide, without further flame annealing treatment, atomically flat terraces on the range of several 100 nm (terraces of 100-200 nm were typically observed).

3.1.3 Preparation of SAMs from Solution

TPT monolayers were prepared on Au(111)/mica from DMF-based solution. For this, the clean gold substrate was immersed in 1 mmol solution of TPT in dry and degassed DMF. The solution was heated at 70 °C under inert atmosphere. After 24 hours the sample was removed from solution, rinsed with DMF and EtOH and blown dry with nitrogen. Subsequent to their preparation, the samples were protected by argon atmosphere and stored not more than one

day before being introduced into the multichamber UHV system. XP spectra typically revealed the absence of any oxidized carbon or sulfur species. If not, the samples were not used for the STM experiments.

3.1.4 Preparation of SAMs from Gas Phase

TPT molecules were deposited from gas phase on Au(111)/mica substrates under UHV conditions. For this, a clean Au(111) surface was prepared by argon sputtering for 10 min at 1 keV and a pressure of 3×10^{-6} mbar. Subsequently, the sample was annealed at 673 K for 1 hour in order to obtain a flat substrate surface characterized by large gold terraces. The grade of purity was monitored by measuring the C 1s and O 1s XPS signal intensities. If required, successive sputtering/annealing cycles were performed until the absence of any aforementioned XPS signal was proven. Immediately subsequent to sputtering, the gold substrate was exposed to the molecular beam from a quartz crucible inside a Knudsen-type organic evaporator (TCE-BSC, Kentax). The crucible was filled with TPT crystals previously purified by sublimation. The sublimation temperature was set to 398 K and the substrate was held at room temperature. The chamber pressure during the evaporation process was ~10^{-8} mbar and the evaporation time was ~30 min. Subsequent to the evaporation step, the XPS S 2p signal was monitored in order to prove the existence of thiolates (R-S–Au) as well as unbound thiols (R-S-H, physisorbed on top of the SAM surface). To remove physisorbed molecules, the sample was annealed at 343 K for ~15 min. The absence of any traces of physisorbed thiols and the existence of a densely-packed SAM was subsequently verified by XPS.

3.2 Methods

3.2.1 Introduction to the Omicron Multichamber UHV System

The Multiprobe® UHV surface science system (Omicron) is depicted in Figure 3.2. Among others, it is equipped with a combined STM/SEM system, an XPS instrument, two electron flood-guns and an organic evaporator. All instruments are described in detail in the sections of this chapter. The preparation and analysis chambers are interconnected by an integrated transfer system, allowing for transferring the samples between all chambers whilst being protected constantly from surface contaminations by the UHV environment.

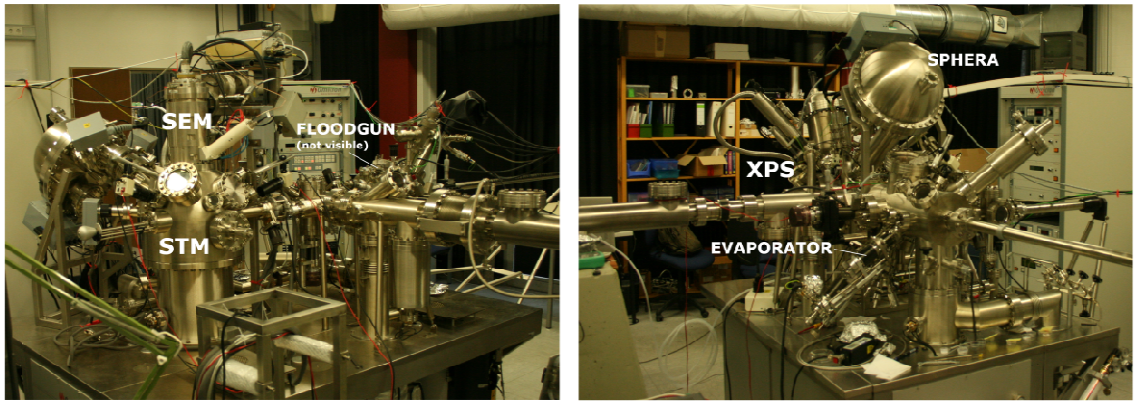

Figure 3.2: Multichamber UHV system (Omicron). (left) Analysis chamber equipped with a combined STM/SEM system. Preparation chamber equipped with an in-situ floodgun. (right) Analysis chamber equipped with XPS with SPHERA electron analyser. Preparation chamber equipped with Knudsen-type organic evaporator. Samples can be transferred between the chambers by the interconnecting transfer system.

3.2.2 X-Ray Photoelectron Spectroscopy

X-ray analysis was performed on an Omicron Multiprobe system by utilizing a monochromatic Al K_α source (XM1000, 1486.7 eV, 225 W) under UHV conditions (~10^{-11} mbar). A Sphera hemispherical electron analyser (Omicron) with a spectral resolution of 0.9 eV was utilized for the analysis of the emitted photoelectrons. The X-ray beam was focused on the sample surface under normal incidence and the angle of the detected photoelectrons was 77° with respect to the surface normal. The binding energies were calibrated with reference to the Au $4f_{7/2}$ signal at 84.0 eV. The short exposure of the monolayers to the X-ray beam did not lead to detectable, irradiation-induced changes. The analysis of the photoemission spectra was conducted by using CasaXPS v.2.3.15 (Casa Software Ltd.) analysing software. The S 2p spectra were evaluated by approximating the Voigt functional signal form with a Gaussian/Lorentzian product form of 70:30 ratio and by using a linear background. The energy separation of the characteristic doublet (S $2p_{3/2}$, S $2p_{1/2}$) was constrained to 1.2 eV[102] and the area ratio to 2:1 . The C 1s and Au 4f spectra were evaluated by fitting Shirley backgrounds. The Au $4f_{7/2}$ and Au $4f_{5/2}$ signals were fitted by using the Gaussian/Lorentzian sum form of 20:80 ratio and an area ratio of 4:3. The C 1s spectra were fitted by using a Gaussian/Lorentzian product form of 70:30 ratio. The effective monolayer thickness was estimated from the attenuation of Au $4f_{7/2}$ photoelectrons by the monolayer (see section 2.4) and by using an inelastic mean free path of 36 Å[13].

3.2.3 STM/SEM Combination System

The STM experiments were performed on a commercial Omicron Multiscan system combining both a variable temperature STM (Multiscan STM VT) and a SEM, as depicted in Figure 3.3. The SEM is a modified type of a UHV Zeiss Standard Gen ini with a Schottky-type thermal field emission source (ZrO/W). The STM tip is aligned by ~45° with respect to the surface normal, thus enabling to control the position of the STM tip by SEM. The STM chamber pressure was ~10^{-11} mbar.

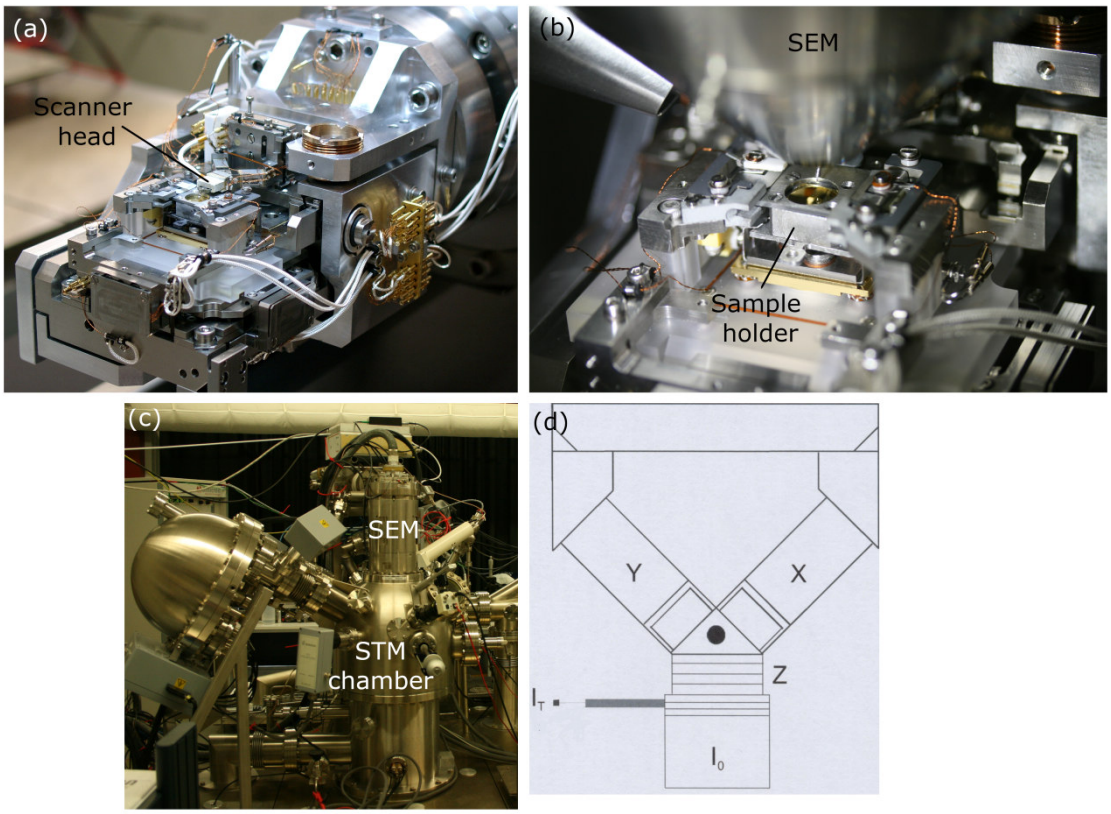

Figure 3.3: (a) Multiscan STM VT (Scienta Omicron) outside of the analysis chamber. (b) STM inside the analysis chamber. The outer housing of the SEM column is visible. (c) STM analysis chamber and SEM column from the atmospheric side. The hemispherical analyser for performing Auger spectroscopy is also visible. (d) STM scanner head with individual piezos for x- and y-movements. A z-resolution of better than 0.01 nm can be achieved.

3.2.4 Electron Irradiation

3.2.4.1 Irradiation by Flood-Gun

Flood guns provide a cm^2-sized, almost homogeneous electron flux which makes them ideal for the fabrication of CNMs. TPT SAMs were irradiated under UHV conditions with electrons from an in-situ floodgun (FG20, Specs) with an energy of 50 eV. The dose was calibrated by using a Faraday cup. After applying distinct doses, STM measurements were performed.

3.2.4.2 Irradiation by SEM

To cross-link SAMs by the rastering electron beam of the SEM, the kinetic energy of the electrons was set to 1 keV for all experiments, which is the minimum energy of the SEM. The pressure in the SEM column was ~10^{-8} mbar. Prior to each experiment, the beam current was measured by using a Faraday Cup. SAMs were irradiated with beam currents ranging from 200-600 pA. For this purpose, the SEM beam was rastered over the sample surface with a distinct number of cycles. Prior to electron irradiation, the STM tip was retracted and moved sufficiently far away from the surface location of interest, so that the electrons to may pass the tip and reach the surface location. This procedure is described in detail below. The irradiated area was typically around $30 \times 40\ \mu m^2$. The time per cycle was 2.5 s. The irradiation dose applied to the surface, *d,* is calculated from the beam current, *I,* the cycle time, *t*, the number of cycles, *n,* and the scan area, *A,* according to $d = (I \times t \times n)/A$. The diameter of the SEM beam was sufficiently lower than the SEM scan width/height. All STM data was acquired at room temperature under UHV conditions (chamber pressure < 10^{-10} mbar). The instrument was operated in the constant-current mode with tunneling currents of 10 – 100 pA and sample biases between −1.2 to −0.4 V and +0.4 to +1.2 V. A z-resolution of better than 0.01 nm can be achieved. The STM tips were prepared from 0.375 mm polycrystalline tungsten wire (Alfa Aesar) by electrochemical etching in 3 M NaOH solution. The instrument was calibrated by imaging HOPG with atomic resolution. The data was post-processed by using *gwyddion v.2.41* free software.

The main advantage of the STM/SEM combination system is the possibility to irradiate the TPT SAM locally and to acquire STM images of the same sample location immediately before and after irradiation, thus allowing for observing the influence of the electrons on the SAM on the local, molecular level.

The experimental implementation requires several steps, as listed below. A simplified scheme is depicted in Figure 3.4.

1) The SEM beam energy is set to 1 keV.

2) The beam current is measured by using a Faraday cup (20 µm aperture).

3) The SEM beam is focused on the very front part of the STM probe tip which is in tunneling contact (scan area ~$30 \times 40\ \mu m^2$).

4) The beam path is interrupted by using a beam shutter.

5) The STM tip is retracted by several micrometers in order to avoid a tip crash during the following step.

6) The sample stage is moved by ~1 mm in order to bring a pristine part of the SAM surface into the focus of the SEM beam.

7) The STM probe tip is brought in tunneling contact with the sample surface and STM data of the pristine SAM is acquired.

8) The STM probe tip is retracted from the surface over the full travel of the z-piezo actuator and moved laterally over the full travel of either the x- or y-piezo actuator.

9) The beam shutter is opened and the required electron dose is delivered to the surface.

10) The beam shutter is closed and the STM probe tip is moved laterally over the full travel of the respective piezo actuator to its original position.

11) The STM tip is brought in tunneling contact and STM data of the same, now irradiated sample location is acquired.

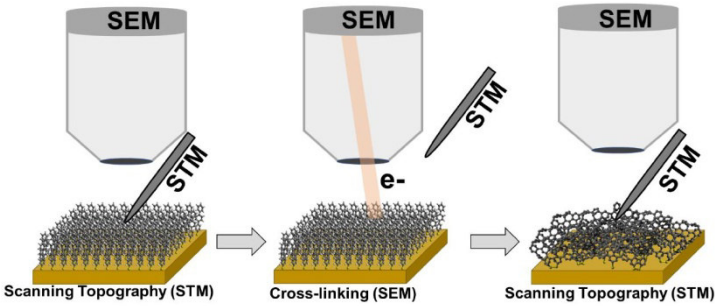

Figure 3.4: Simplified scheme of the SEM irradiation process, accompanied by STM imaging of the same sample location before and after irradiation. At first, STM data of the pristine SAM is acquired. Second, the STM probe tip is retracted and moved to the side in order to enable the subsequent irradiation by the SEM beam. Finally, the STM probe tip is positioned back to the initial sample location and STM data of the same, now irradiated sample area is acquired.

3.2.5 Post-Imaging Software Image Correction

STM images are typically subject to linear and non-linear distortion, i.e. *thermal drift*, *piezo creep, piezo hysteresis*, and *cross-talk* which would lead to large errors in the determination of distances and angles if the images would not be subsequently corrected by employing suitable standard protocols.

Thermal drift is typically a linear effect and results from the fact that the components building up the STM device, in particular the scanner head including scanning probe, piezo ceramics and linking parts and the scanning stage consist of different materials with different *coefficients*

of thermal expansion (CTE) and temperature diffusivities. Slow temperature variations ΔT and the difference between the thermal expansion coefficients α cause thermal drift according to $\Delta l/l=\Delta\alpha\cdot\Delta T$[68]. The consequential linear relative (lateral and vertical) motion between the STM tip and the sample surface during the scan was estimated to ~10 nm/h when a change in temperature of only 1 K/h and a difference in the CTE of 10% between two materials is assumed[103]. Within the scope of this thesis, typical image sizes are ~10-100 nm and typical image acquisition times are 10-30 min. Therefore, the acquired images had to be corrected subsequent to the scan. Given that thermal drift is typically a linear effect, that is, the drift velocity is nearly constant during the acquisition of successive up- and down-scans, as the acquisition of STM images is usually carried out on a time scale significantly shorter than the time that is needed to reach thermal equilibrium, SPM images can easily be corrected by applying basic affine image transformations, in particular scaling and shearing operations. A procedure for correction of SPM images distorted by linear thermal drift was developed by Rahe *et al.*[103] and applied for the images for this thesis by using the polynomial distortion tool of *gwyddion 2.41*[104].

Piezo creep is a non-linear effect and an inherent property of the piezo ceramics. Creep appears after a fast voltage change, that is, when the STM tip is moved on a short time scale over a long distance relative to the sample surface, e.g. in the course of moving to a new sample location (creep in *x*- and/or *y*-direction) of after approaching the STM tip to the sample surface to create the tunneling contact (creep in *z*-direction). Piezo creep is characterized by a slow logarithmic expansion according to $\Delta l/l=\alpha+\beta\cdot\ln(t)$[68], where α and β are constants that depend on the piezo ceramics and t is time. The fact that piezo creep occurs to different extent, depending on the ramp shape of the voltage change, makes a post-imaging processing of the STM image difficult, in particular if sample surfaces of low order and unknown structure are investigated. Within the scope of this thesis, creep effects on the images were minimized by waiting long enough before the acquiring the new image. Due to its logarithmic character, piezo creep becomes nearly linear over time and cannot be distinguished from linear thermal drift effects anymore. Post-imaging correction was therefore carried out by using the standard protocol for thermal drift correction[103].

Piezo hysteresis is a non-linear effect and the most accepted explanation for this behavior is attributed to reversible and irreversible displacement or sliding of polarization domain walls, which are related to the material polarized grains[105]. However, significant hysteresis effects in

the instrument used for this thesis (see previous section) only become significant when acquiring STM images with sizes > 100 nm with the typically used scan velocities of ~100-300 nm/s in the fast scan direction. Those images were, due to their large size, not used for the precise determination of characteristic distances and angles. Therefore, no hysteresis correction was performed

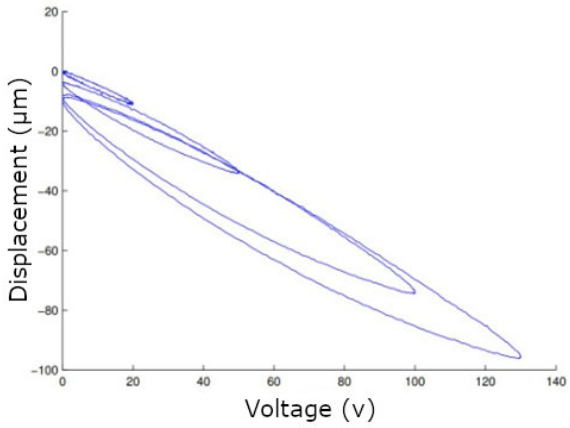

Figure 3.5: Hysteresis upon applying consecutive voltage inputs of different amplitudes to the piezo actuator with a frequency of 50 Hz. This figure was adapted from ref [105].

Cross-talk. The scanner head of the Multiscan STM VT experiences, due to its construction, a significant crosstalk between the lateral piezo actuators of the x- and y- axis that typically leads to a deviation between the geometries of the desired and the actual raster scan pattern (see Figure 3.6). All STM images were obtained at a scan angle of 0°, which means that the fast scan direction is parallel to the x-axis, which is the elongation axis of the respective piezo actuator. The crosstalk predominantly affects the angle φ between the fast and the slow scan direction but to a minor extent also the width w and the height h of the scan (see Figure 3.6). Table 3.1 lists the parameters needed for correcting the cross-talk effect in STM in ages of various scan sizes. The correction of the STM images was eventually performed by using the arithmetic averages of the scale factors $(w_{raw}/w_{corr})_i$ and $(h_{raw}/h_{corr})_i$ and the shear factors φ_i. The contribution of cross-talk effects to the total measurement uncertainty of the Multiscan STM VT in terms of length and angle measurements amounts to $\Delta l_{CT}/l = 2.4\%$ and $\Delta\varphi_{CT}/\varphi = 0.9°$. The errors of the cross-talk calibration parameters affect all recorded STM images. Cross-talk correction was carried out using the *Affine Distortion*-tool of *gwyddion 2.41*[104].

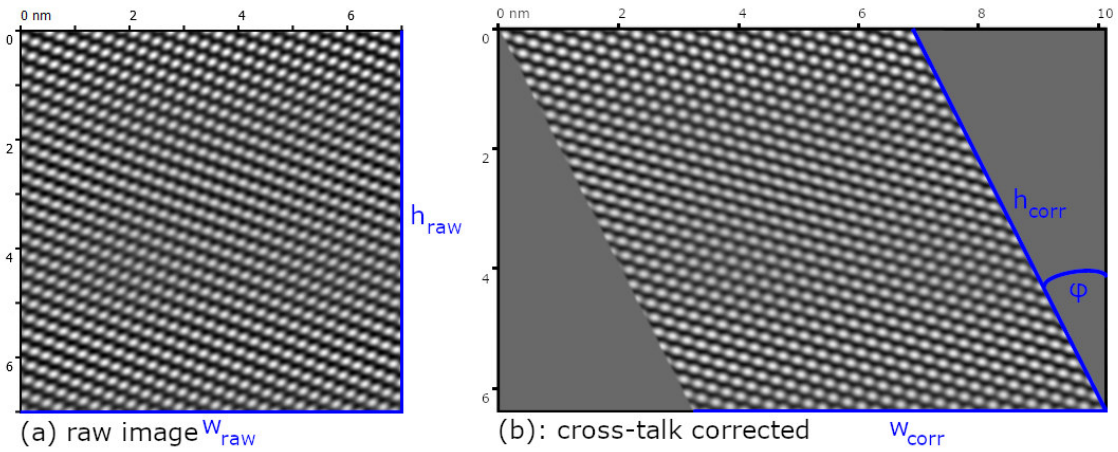

Figure 3.6: STM image of a HOPG surface before (a) and after (b) cross-talk compensation was performed.

Table 3.1: Cross-talk compensation parameters for high-magnification STM images for the Omicron Multiscan STM VT instrument (see previous section). The parameters were determined by employing a HOPG surface as reference. The scan angle is 0°.

	Scan size [nm]	w_{raw}/w_{corr}	h_{raw}/h_{corr}	Shear angle φ
Mar 2018	10x10	99.1%	101.8%	26.9°
	20x20	99.7%	102.7%	26.7°
	30x30	99.6%	101.9%	26.7°
Feb 2019	10x10	98.5%	102.9%	25.4°
	20x20	98.8%	104.9%	25.3°
	30x30	99.1%	100.9%	26.1°
Mean values and maximum errors		99.1 ± 0.6%	102.5 ± 2.4%	26.2 ± 0.9°

The Matrix software from version V2.1 supports a crosstalk compensation facility that enables to minimize the deformation of the raster scan pattern during the scan process. For this, the crosstalk of x- and/or y-axis needs to be determined by measuring a reference sample such as HOPG or Si(111)-(7x7). The correction factors describing the actual scan axis deflection can be varied during the scan, until the topography of the reference sample shows the expected symmetry. Similar to the affine distortion operations described previously, the calibration parameters are determined once and are used for the recording of subsequent STM images. Therefore, STM images recorded with active crosstalk compensation are subjected to the same measurement errors as calculated previously.

Total measurement uncertainty of the Multiscan STM VT. All aforementioned linear and non-linear distortion effects affect the measurement accuracy of the Multiscan STM VT. However, their contributions may be more or less pronounced, depending on the current status of the experiment. For example, thermal drift might become partially non-linear if the acquisition time of the image is long and as a result, the accuracy of the employed correction protocol[103] is lowered. Within the scope of the experiments for this thesis, however, no length and angle deviations of over $\Delta l/l = 10\%$ and $\Delta\varphi/\varphi = 5.0°$ were observed after software image correction had been performed. This is in agreement with previous studies on the same instrument[31]. It is proposed that the determination of all characteristic length and angle values within the scope of this thesis are subject to the respective measurement errors.

4 Results and Discussion

Cross-linking of aromatic SAMs upon exposure to low-energy electrons (1-100 eV) has already been studied thoroughly by spectroscopic methods (see section 2.2). However, microscopic data covering defined intermediate stages of cross-linking that allows for the quantitative characterization of the structural transformation on the nanometer-scale is still lacking. Within the scope of this thesis, TPT SAM on Au(111) in mica was used as a model system to investigate electron-irradiation induced cross-linking by STM. Two different methods were used to irradiate the monolayers with electrons, in which 50 eV and 1 keV PEs were used. In the first section of this chapter, the influence of the kinetic energy of PE's on cross-linking will be discussed based on the quantitative XPS data. In particular, the effective cross-sections for the chemical modification of the carbonaceous matrix and the sulfur-gold interface of TPT SAM under 50 eV and 1 keV irradiation were calculated from the XPS data, which provides complementary data for the corresponding STM measurements. The second section focuses on the STM characterization of pristine SAM surfaces, which were prepared either from DMF-based solution or from gas phase under UHV conditions. In the following section, STM data for the initial stage of cross-linking are presented, where the changes of structural features on a molecular level, arising from the electron-molecule interaction, and the underlying elementary mechanisms will be discussed. In the last section, the evolution of the monolayer towards a fully cross-linked state and the associated structural transformation are investigated.

4.1 XPS Study of Cross-Linking: Effect of the PE Energy

The present study deals primarily with the influence of the kinetic energy of the PEs on cross-linking, in particular with the influence on the structural and chemical evolution of the carbonaceous matrix including the evolution of the carbon content and with the influence on the chemical evolution of the gold-sulfur interface. The experiments were performed in accordance with previous XPS studies[13].

The cross-sections obtained in this study represent average values that include the contribution of all electron-induced effects and processes that cause modifications in the respective system, in particular the relative contributions of electron impact ionization, electron impact excitation and electron attachment (see section 2.2).

SAMs were irradiated with 50 eV and 1 keV PEs using an in-situ flood-gun (SL1000, Omicron), which provides an homogeneous beam profile in an adequate lateral scale. The evaluation of the XPS data is described in section 3.2.2. SAMs were exposed to electron doses of 2.5/5/10/20/30/40/50/60/75 mC/cm². One pristine TPT sample was irradiated with 50 eV PEs and two samples with 1 keV PEs. Three XPS regions were studied: C1s, S2p and Au4f. Immediately prior to each XPS experiment, a clean Au substrate was measured as a reference to exclude systematic errors as a result of intensity variations of the incident X-ray beam. As the irradiation of the samples was carried out under UHV conditions, additional chemical reactions associated with electron irradiation, e.g. the formation of C-O-C bonds, can be excluded. The absence of oxygen was monitored during the whole irradiation process.

The negligibility of the influence of the X-ray beam on the monolayer-substrate system was verified in an independent experiment. A pristine SAM was exposed to the X-ray irradiation for a time period much longer compared to common measurement times (> 1 day) and only marginal changes of the C 1s and S 2p regions were detected.

4.1.1 Evolution of the Carbonaceous Matrix

The structural and chemical modification of the carbonaceous matrix is studied by means of the XPS C 1s photoelectron signal. The signals (black) are shown in Figure 4.1 (a) and (b) for PE energies of 50 eV and 1 keV, respectively. Spectra are displayed for doses of 20 to 80 mC/cm², respectively. The signals consist of the main C 1s peak (red) with a binding energy of 284.2 eV, assigned to the carbon atoms forming the phenyl rings, and a weak shoulder (blue) at 285.2 eV, assigned to the carbon atom bound to the sulfur (see Figure 4.1). Cross-linking leads to manifold modifications of the carbonaceous matrix (see section 2.2), e.g. the cleavage of C–H bonds, the formation of intermolecular covalent carbon-carbon bonds, loss of aromaticity, and the loss of conformational and orientational order. Therefore, the dependency of the C1s *full width of half maximum* (FWHM) on the irradiation dose is generally characterized by a sharp increase in the low-dose regime and a level-off behavior towards high doses[15],[106],[57]. The evolution of the C1s FWHM upon 50 eV and 1 keV electron exposure is shown in Figure 4.1 (c). Both PE kinetic energies have similar dependencies of the C1s FWHM on the irradiation dose. The dose- dependencies are characterized by a sharp increase in the low-dose regime (< 10 mC/cm²) and a level-off behavior towards doses up to 50 mC/cm², in agreement with previous studies[15]. The data sets were fitted by a standard saturation function

(see Equation 4.1) which was previously used to describe irradiation-induced modifications in SAMs[107],[108].

$$I = I_{sat} + (I_{pris} - I_{sat}) \times \exp(-\sigma \cdot d/e) \qquad \text{Equation 4.1}$$

where I represents the dose-dependent value of a characteristic parameter of the monolayer (here the shift of the C1s FWHM), I_{pris} and I_{sat} are the respective values for the pristine and fully cross-linked monolayer, d is the irradiation dose (typically in mC/cm²), e is the elementary charge, and σ represents the cross-section.

It is obvious that the carbonaceous matrix is modified predominantly at low doses less than 10 mC/cm². By fitting the data points (50 eV: red, dashed lines, 1 keV: black, dashed lines) using Equation 4.1, the cross-sections for the structural and chemical modification of the carbonaceous matrix are obtained, i.e. $2.9 \pm 0.7 \times 10^{-17}$ cm² (50 eV PE energy) and $2.0 \pm 0.4 \times 10^{-17}$ cm² (1 keV PE energy). For each data set, the individual data points represent the shift of the C1s FWHM calculated by subtraction of the respective dose-dependent FWHM value from the one of the pristine SAM. The 50 eV cross-section obtained here is in good agreement with the corresponding XPS-derived cross-section from in the literature[15]. In particular, an effective cross-section for hydrogen content loss of $3.7 \pm 1.0 \times 10^{-17}$ cm² was measured by employing HREELS[53], indicating that the XPS data reflects to some extent the loss of hydrogen of the carbonaceous matrix. No literature data are available for 1 keV PE energy. The similarity between the 50 eV and 1 keV cross-sections indicate that both PE kinetic energies cause similar modifications of the carbonaceous matrix, which makes it possible to reasonably correlate the respective STM data.

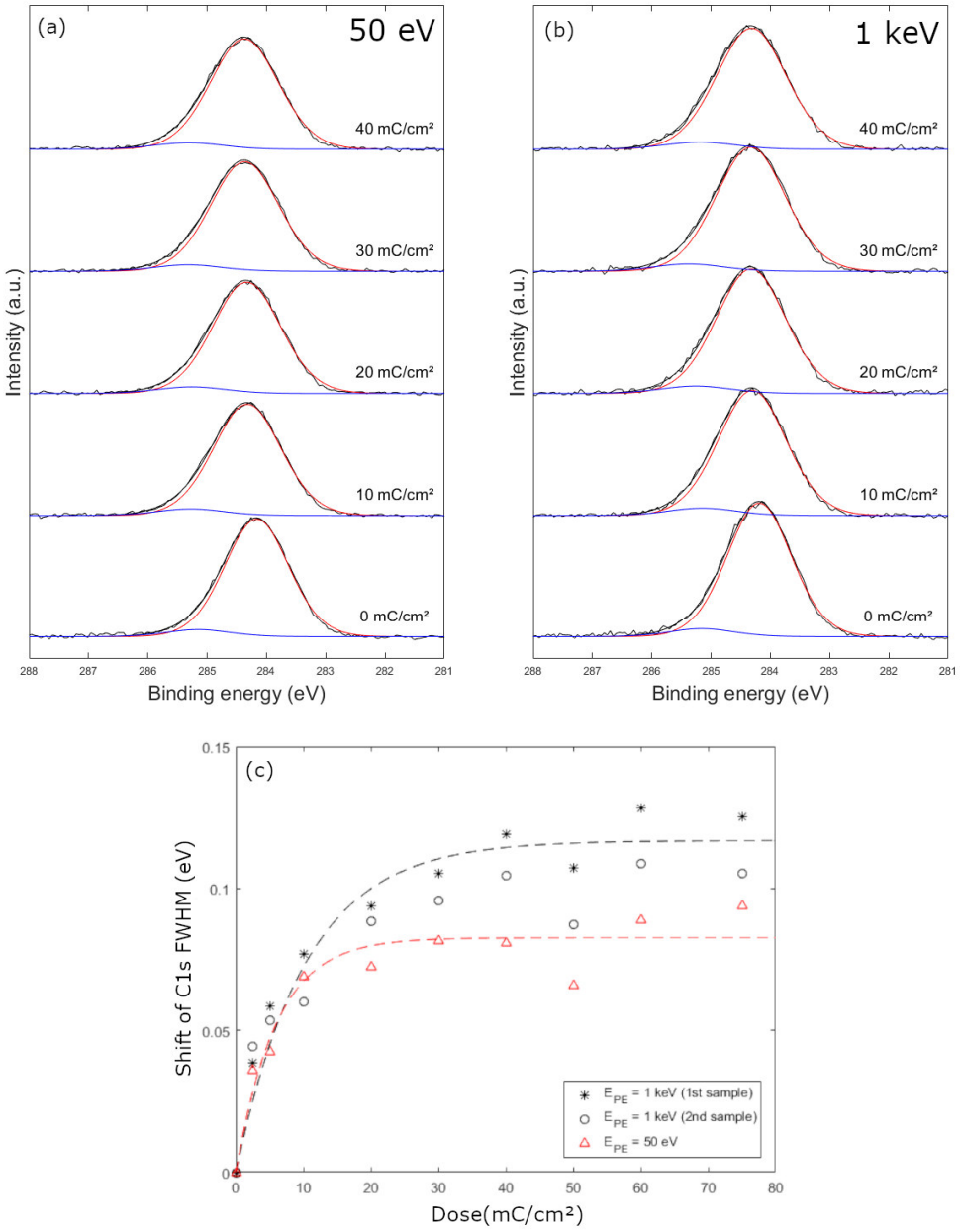

Figure 4.1: (a), (b) XP spectra of the C1s peak regions of the pristine and irradiated TPT SAMs. Electron exposure was conducted with 50 eV and 1 keV incident electrons; spectra are displayed for doses of 10-40 mC/cm², respectively. The raw data (black) was fitted with two peaks, the main peak (red) and the shoulder peak (blue), see text for details. (c) Evolution of the shift of the C 1s FWHM as a function of the irradiation dose. The shift values were calculated by subtraction of the measured values from the respective values of the pristine SAM. Electron irradiation was conducted with 50 eV (red) and 1 keV (black) incident electrons. The data points in panel (a) and (b) were fitted according to Equation 4.1.

As already discussed in section 2.2, the electron impact can lead to a marginal desorption of carbonaceous material, so that the carbon content is largely retained. The evolution of the carbon content was evaluated by means of the energy- and dose-dependent C 1s/Au 4f photoelectron signal ratio and the monolayer thickness (see section 2.4). The Au 4f signals are shown in Figure 4.2 (a) and (b) for PE energies of 50 eV and 1 keV, respectively. Spectra are

displayed for doses of 20 to 80 mC/cm², respectively. The raw data (black) was fitted with one doublet. The envelope of the fit is shown in red. Figure 4.2 (c) and (d) show the dependency of the C 1s/Au 4f photoelectron signal ratio and the film thickness on the irradiation dose, respectively. The results presented here indicate that both PE energies lead to a slight desorption of carbonaceous material for doses < 10 mC/cm². The reduction of the C 1s/Au 4f photoelectron signal ratio is more pronounced when the SAM is irradiated with 1 keV PEs. This can be attributed to a slight desorption of carbonaceous material at the initial stage of the irradiation process. Electron-stimulated desorption should occur more frequently for high-energy electrons than low-energy electrons. The irradiation with 50 eV PE's (red data points) caused a slight, almost linear decrease of the C 1s/Au 4f photoelectron signal ratio with increasing irradiation dose, resulting in a ~2-3 % reduction of the C 1s/Au 4f signal ratio after irradiation with a dose of 50 mC/cm². However, the calculated layer thickness (see section 3.2.2) is subject to relatively high fluctuations and a similar tendency cannot be observed clearly. The irradiation with 1 keV PEs (black data points) initially caused a 3-7 % reduction of the C 1s/Au 4f photoelectron signal ratio for both samples. Consequently, the calculated layer thickness is initially reduced. The evolution of the respective values towards high irradiation doses (> 10 mC/cm²), however, is different for both samples. The C 1s/Au 4f signal ratio remained unaltered for one sample and increased by ~5 % for the other sample after irradiating with a dose of 50 mC/cm². This can be attributed to different adsorption rates of residual molecules from the UHV environment over time as a result of pressure differences in the XPS chamber. The respective thickness values show similar dependencies, but are subject to relatively high fluctuations.

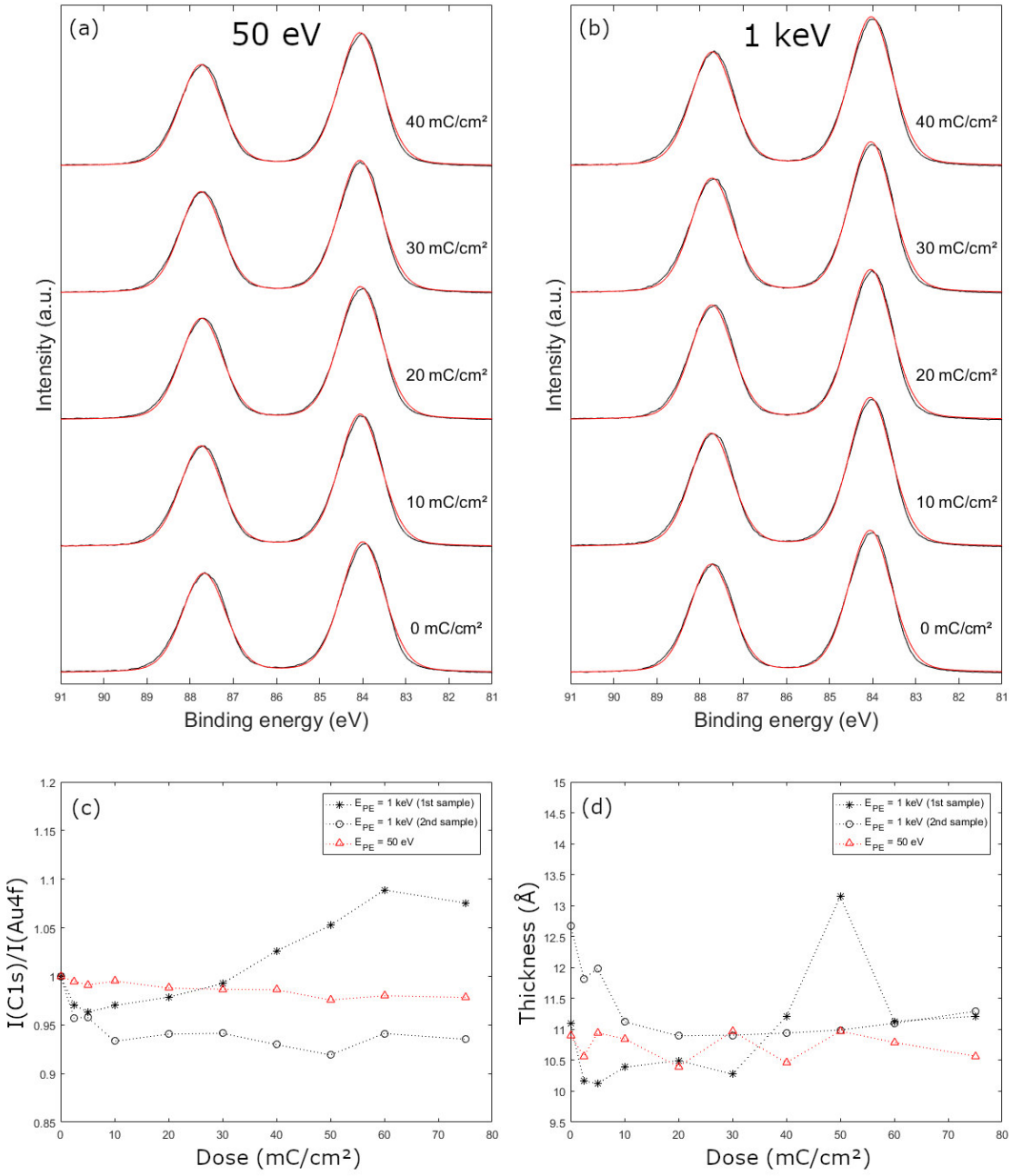

Figure 4.2: (a), (b) XP spectra of the Au 4f doublets of the pristine and irradiated monolayers. Electron exposure was conducted with 50 eV and 1 keV primary electrons. Spectra are displayed for doses of 20 to 80 mC/cm², respectively. The raw data (black) is fitted with one doublet; the envelope is shown in red (see text for details). (c) Evolution of the C 1s/Au 4f photoelectron signal ratio as a function of the irradiation dose. (d) Evolution of the calculated monolayer thickness. Electron irradiation was conducted with 50 eV (red) and 1 keV (black) incident electrons.

4.1.2 Evolution of the Sulfur-Gold Interface

As already discussed in section 2.2, electron exposure causes the cleavage of S–Au bonds, followed by the formation of a new sulfur species. The pristine SAM is characterized by the sole presence of thiolates. The evolution of the XPS S 2p regions at 50 eV and 1 keV electron

exposure are shown in Figure 4.3 (a) and (b), respectively. For both PE energies, a chemical transformation similar to the results of previous studies[15],[13] was observed, i.e. the electron exposure leads to a conversion of the thiolate-related XPS signal (red doublet) at 162.0 eV to a new sulfur species (blue doublet) at 163.1–163.4 eV. The ratio between the S 2p signal ascribed to the new sulfur species and the total S 2p signal is displayed in Figure 4.3 (c), together with the evolution of the total amount of sulfur normalized by reference to the value of the pristine SAM. The total amount of sulfur remains almost unchanged during irradiation. The data points are subject to high fluctuation due to the low signal-to-noise ratio of the S 2p photoelectron signal. However, a slight increase of the total amount of sulfur caused by doses less than 10 mC/cm², together with the initial increase of the C 1s/Au 4f signal ratio (see above), indicates a low extent of electron-induced desorption of carbonaceous material. The energy-dependent cross-sections for the cleavage of S–Au bonds were determined by fitting the XPS data according to Equation 4.1 (50 eV: red, dashed lines, 1 keV: black, dashed lines). For 50 eV PE energy, a cross-section of $0.8 \pm 0.2 \times 10^{-17}$ cm² was determined. For 1 keV PE energy, the cross-section is $1.2 \pm 0.2 \times 10^{-17}$ cm². Both cross-sections are in good agreement with the value determined by Yildirim *et al.* for 50 eV PE energy, which was found to be $1.7 \pm 0.3 \cdot 10^{-17}$ cm²[15].

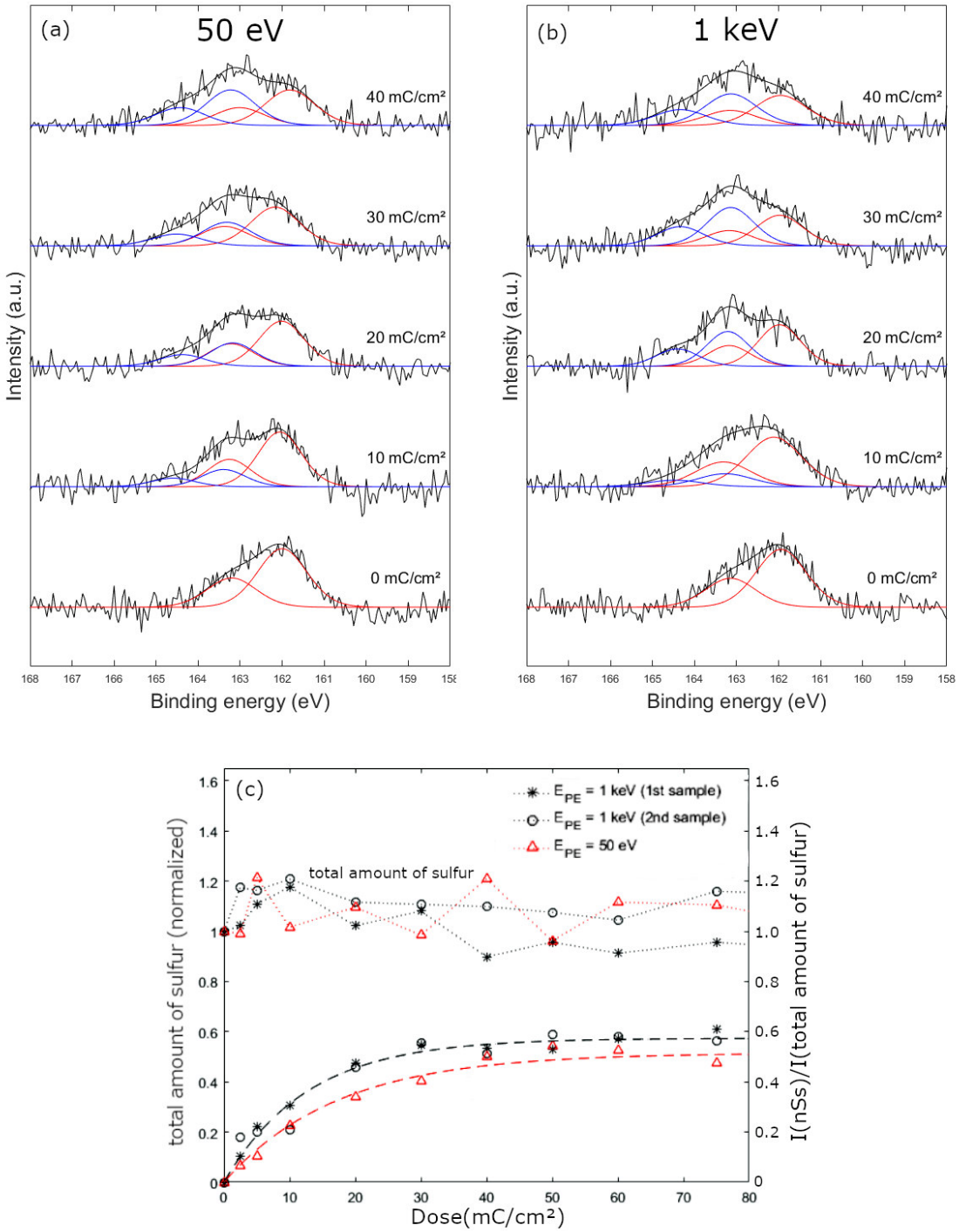

Figure 4.3: (a),(b) XP spectra of the S 2p doublets of the pristine and irradiated TPT SAM s. Electron exposure was conducted with (a) 50 eV and (b) 1 keV incident electrons. Spectra are displayed for doses of 10 to 40 mC/cm², respectively. The XPS raw data of the pristine SAMs are fitted with one S 2p doublet, attributed to thiols on gold[13],[15]. The raw data of the irradiated SAMs are fitted with two S 2p doublets, attributed to thiols on gold (red) and the other to the irradiation-induced species (blue), see text for details. (c) Ratio between the XPS photoelectron signal of the irradiation-induced new sulfur species and the total sulfur intensity as a function of the irradiation dose, both determined for 50 eV (red) and 1 keV (black) processed SAMs. The fits were calculated according to Equation 4.1. The total amount of sulfur was determined as the sum of the intensities of both doublets and normalized to the pristine SAM.

4.1.3 Summary

The present XPS study focuses primarily on the influence of the kinetic energy of the PEs on cross-linking, as SAMs were exposed to 50 eV and 1 keV electrons in this work. For 50 eV PE energy, both the cross-sections for the structural and chemical modification of the carbonaceous matrix and the cleavage of S–Au bonds are in agreement with the corresponding values from the literature. It was found that the response of the monolayer/substrate system on 1 keV electron impact does not differ significantly from the impact of 50 eV electrons, so that the corresponding STM data can be correlated. XPS data also indicates a slight desorption of carbonaceous material from the SAM during the irradiation process and adsorption of carbonaceous molecular residuals, possibly originating from the vacuum chamber or the sample holder, may also occur.

4.2 STM Characterization of the Pristine SAMs

Prior to the investigation of cross-linking, the pristine SAM surfaces were characterized by STM. As described in section 3.1, SAMs were prepared either in DMF-based solution which has been the standard method for the preparation of CNMs from TPT precursors[9],[1], or from gas phase under UHV conditions which may yield SAMs of comparable molecular structure but being more suitable for STM experiments due to a very low content of contamination. It turned out that STM experiments involving SAMs prepared from DMF-based solution were typically subject to unstable imaging conditions. This may have been caused by the presence of mobile contaminants that probably evolved during preparation or the subsequent exposure to the ambient air. The quality of the SAMs prepared by both approaches was evaluated by XPS. This was done by verifying the integrity of the sulfur-gold interface (only presence of thiolates and absolute absence of oxidized sulfur species) and the carbonaceous matrix (absolute absence of oxidized carbon species).

4.2.1 Preparation of SAMs from DMF-based solution

The preparation from DMF-based solution typically yielded SAMs characterized by the presence of well-ordered phase domains with sizes of 10-100 nm. An STM overview scan of the pristine monolayer surface is shown in Figure 4.4 (a). Two major, nearly densely-packed molecular phases were identified, which were previously observed by Bashir *et al.* in case of

TPT SAMs on Au(111) prepared in ethanol[39]. The phases were designated as α-phase (marked in green) and β-phase (blue). This notation will also be used in this thesis. Similar phase structures were observed and discussed earlier in 2001 by Ishida *et al.*[34] (observation of molecular patterns similar to the β-phase, but interpreted as flat-lying molecules) and Fuxen *et al.*[41] (observation of the α-phase). The image also reveals the existence of gold adatom islands on top of the Au terraces covered with TPT molecules. Those islands are not present on the bare Au surface but typically form during the self-assembly process of arenethiol SAMs on Au(111)[109].

α-phase. A *fast Fourier transform* (FFT)-enhanced STM image section is shown in Figure 4.4 (b). The observed pattern is characterized by repeating parallel rows with different brightness. The rows are composed of equivalent features attributed to individual TPT monomers[39]. The absence of an additional Moiré-like superstructure indicates a commensurate molecular arrangement with respect to the Au substrate. A model of the molecular structure of the α-phase of TPT on Au(111) is shown in Figure 4.4 (e) (reprinted from ref [39]). The sulfur atoms are located on a $(\sqrt{3} \times \sqrt{3})R30°$ lattice (similar to aliphatic SAMs[110]), whereas the molecular backbones form a herringbone-like arrangement. The different twist angles (with respect to the substrate) of the molecules can result in different electronic coupling efficiencies between the tip and the substrate[39] and thus to a different brightness in STM images. The periodic structure of the molecular backbones can be described by a $(2\sqrt{3} \times \sqrt{3})R30°$ structure. The unit cell is drawn in black. The unit cell contains two molecules. According to ref [39], the unit cell vectors are aligned along the $< 11\bar{2} >$ directions of the Au(111) substrate. The unit cell dimensions were quantified by means of the STM image section shown in Figure 4.4 (b). Line A represents a periodic pattern of equivalent maxima with a periodicity of 0.54 ± 0.06 nm. For line B, a periodic pattern of two unequal features with a periodicity of 0.98 ± 0.10 nm was found. The angle between the unit cell vectors is 125.2 ± 5.0°. The calculated area per molecule is 0.216 ± 0.036 nm², in agreement with ref [39]. On the scale of the phase domains, the SAM-ambient interface of the α-phase is slightly elevated by ~0.6–0.8 Å compared to the surrounding β-phase domains (see below). This indicates a smaller tilt angle of the molecules with respect to the surface normal compared to the molecules forming the surrounding β-phase domains. The tilt angles were estimated by Bashir *et al.,* yielding ~13° for the monomers in α-phase domains and 33–49° for the monomers in β-phase domains.

***β*-phase.** In contrast to α-phase domains, β-phase domains are characterized by the presence of a periodic superstructure including parallel stripes with a distance of ~2 nm. An FFT-enhanced STM image section is shown in Figure 4.4 (c). The superstructure indicates an incommensurability between the TPT overlayer and the Au(111) surface. Two different symmetry directions must be distinguished: the *stripe direction* and the *pair stacking direction*. The internal structure of the unit cell (black) is characterized by the existence of rows of oval spots aligned at an angle of ~60° with respect to the stripe direction. The β-phase was previously observed and modeled by Bashir *et al.* in case of TPT SAMs on Au(111) prepared in ethanolic solution[39]. Accordingly, the oval spots consist of spherical spots that overlap in pairs, which leads to the conclusion that one oval spot contains two TPT molecules. The distance between the oval spots along the stripe direction (line C) is 9.3 ± 1.0 Å. The distance between the oval spots along the pair stacking direction (line D) is 5.2 ± 0.6 Å. The angle between line A and B is 117.8° ± 5.0°. According to Bashir *et al.*, the superstructure of the β-phase is caused by a point-on-line incommensurability. The unit cell can be formulated as $(4 \times n)$ with parameter n close to 8 ($\begin{bmatrix} 4 & 0 \\ 0 & n \end{bmatrix}$ in matrix notation). A model is shown in Figure 4.4 (f) for $n \sim 7.5$ (reprinted from ref [39]). The molecular pairs forming the oval spots are colored in blue. Both the stripe directions and the pair stacking directions follow the $< 1\bar{1}0 >$ directions of the underlying Au(111) surface, whereby the molecular layer is incommensurable along the pair stacking directions. As the theoretical dimensions of the unit cell depend on the parameter n, possible variations of the unit cell dimensions are calculated by considering extremes such as $n = 7$ and $n = 9$[39]. The theoretical length of the unit cell vector along the pair stacking direction, however, may vary between 2.0 nm (n=7) and 2.6 nm (n=9). The theoretical length of the unit cell vector along the stripe direction and the angle between the unit cell vectors, on the contrary, remain constant and amount to 11.5 Å and 120°, respectively. The area per molecule may vary between 0.251 nm^2 (n=7) and 323 nm^2 (n=9). When n=8 is assumed, the area per molecule is 0.288 nm^2[39].

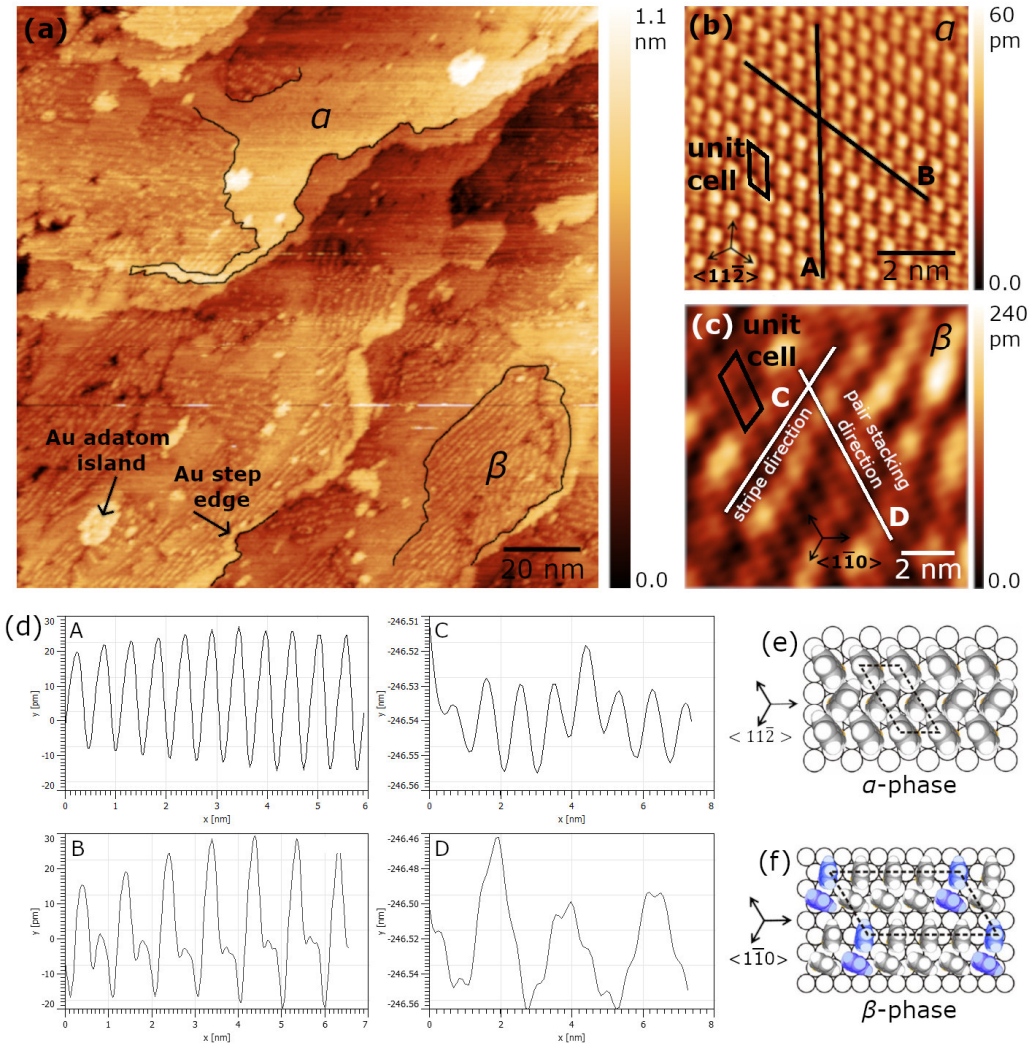

Figure 4.4: Morphology of the TPT/Au(111) surface prepared from DMF-based solution. (a) Low-magnification STM scan of the monolayer surface (+0.4 V, 70 pA, not cross-talk corrected), revealing the existence of two major structural phases, denoted as α- and β-phase. The respective domains are ~10-100 nm in size. The presence of gold adatom islands is also observed. (b) FFT-enhanced high-resolution STM scan of the α-phase (+0.4 V, 100 pA, cross-talk corrected). The unit cell is drawn in black. (c) FFT-enhanced high-resolution STM scan of the β-phase (+0.4 V, 70 pA, cross-talk corrected) including the unit cell. (d) Line profiles of lines A-D shown in (b) and (c). (e) Model of the α-phase of TPT on Au(111). The unit cell is drawn in black, dashed lines. (f) Model of the β-phase of TPT on Au(111) including the unit cell (black, dashed lines) for n~7.5. The pair of molecules forming one oval spot is colored in blue. *Part e and f are reprinted and adapted with permission from ref [39]. Copyright (2013) American Chemical Society.*

4.2.2 Preparation of SAMs from the Gas Phase

SAM preparation from the gas phase has yielded monolayers characterized by the exclusive presence of stripe phase domains, similar or equal to the β-phase observed for TPT SAMs prepared from DMF-based solution. Dissimilar phase domains such as α-phase domains were not observed. This may be a result of the competition and co-adsorption of the TPT molecules and DMF molecules on the Au(111) surface. The molecules in α-phase domains adopt a lower

tilt angle (~13°) compared to the molecules in the β-phase (33–49°)[39]. The area per molecule of the α-phase is also smaller (0.216 nm²) compared to the β-phase (~0.288 nm², see below). This may result from the fact that the adsorption of DMF molecules can impede the formation of flat-lying TPT phases which transform into β-phase domains at higher surface coverages. Instead, the molecules can adsorb directly in an upright orientation and therefore preferentially form phases characterized by a lower tilt angle and higher packing density. However, this assumption should be investigated more closely. An STM overview scan is shown in Figure 4.5 (a). The domain sizes range from 10-100 nm. Similar to the preparation from DMF-based solution or, more generally, arenethiol SAMs prepared in solution[109], the STM data reveals the presence of gold adatom islands covered by TPT molecules in an ordered arrangement (see inset). The adatom islands are elevated by 0.29 ± 0.07 nm with respect to the surrounding SAM-ambient interface, in agreement with the theoretical height of one Au(111) layer, which is 0.24 nm[111]. In contrast to Au adatom islands, which are typically observed for arenethiol SAMs on Au(111) prepared by wet chemistry, the adatom islands observed here have a well-defined shape. The edge contour lines are 60° apart, most likely due to their alignment along the three symmetry directions of the underlying Au(111) surface. Figure 4.5 (b) displays a molecularly resolved STM image of the TPT monolayer. The image shows the coexistence of structural phases similar to the β-phase discussed in the previous section and observed in previous studies[39],[40]. The stripe directions (green) of all domains visible in Figure 4.5 (b) are multiples of 120° (within the measurement error of the instrument) due to the three-fold symmetry of the Au(111) substrate. The pair stacking directions (blue), however, are only multiples of 120° among the phase domains denoted as β. The pair stacking direction (turquoise) of the phase domains denoted as $\beta_{distorted}$ (lower left corner) is twisted by an angle of 7.6 ± 5.0° with respect to the pair stacking directions of the adjacent (undistorted) β-phase domains. The stripe direction of the phase domain $\beta_{distorted}$ is also a multiple of 120° with respect to the stripe directions of the β-phase domains. A structural model of the $\beta_{distorted}$-phase developed within the scope of this thesis is presented below. The measured lengths of the β-phase unit cell vectors (black) are 0.99 ± 0.04 nm (line A) and 2.16 ± 0.05 nm (line B). The enclosed angle between the unit cell vectors is 117.2 ± 5.0°. The measured lengths of the $\beta_{distorted}$-phase unit cell vectors (black) are 0.97 ± 0.07 nm (line C) and 2.24 ± 0.04 nm (line D). The enclosed angle between the unit cell vectors is 117.2 ± 5.0°. Figure 4.5 (b) further shows that the appearance of the oval spots depends on the relative orientation between the fast scan

direction and the domain orientation. Depending on the relative orientation, the oval spots more or less divide into two spherical spots. A similar effect was already observed by Korolkov *et al.*[112] who investigated the dependence of the feature shape on the scan angle by employing a TPT/Au(111) substrate.

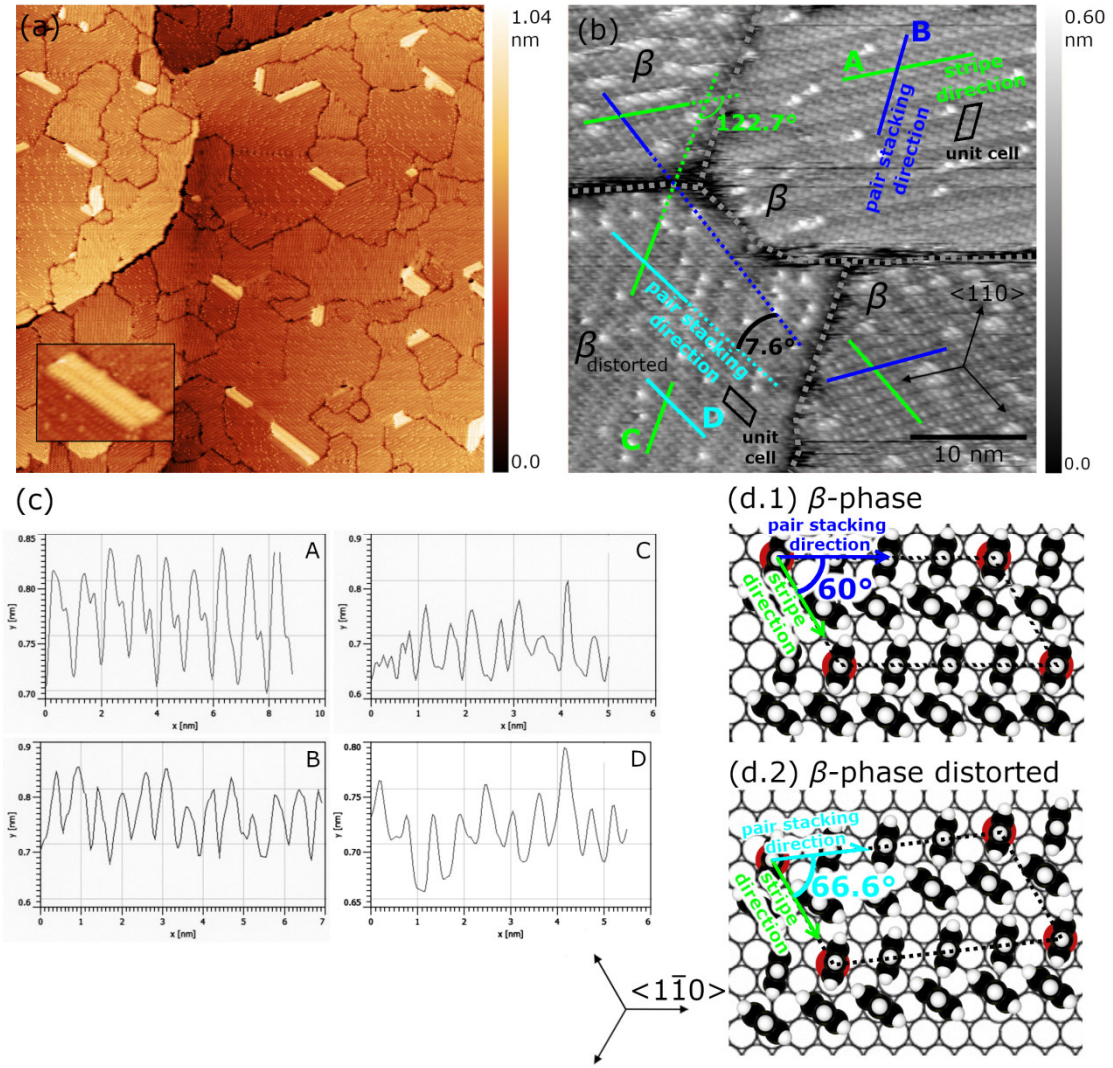

Figure 4.5: Morphology of the TPT/Au(111) surface prepared from the gas phase. (a) Low-magnification STM scan of the monolayer surface (+1.0 V, 30 pA, cross-talk corrected) revealing the presence of ordered domains with domain sizes of 10-100 nm. The STM scan was not perturbed by mobile adsorbates. The inset shows one Au adatom island with a height of 0.29 ± 0.07 nm which is covered by TPT molecules. (b) High-magnification STM image (+1.2 V, 30 pA, cross-talk corrected). The surface is covered by phase domains equal or similar to the β-phase observed previously (see text for details). A slightly distorted phase domain is also observed, denoted as , $\beta_{distorted}$. The stripe directions are highlighted in green. The pair stacking directions of the β-phase and the $\beta_{distorted}$-phase (blue and turquoise, respectively) exhibit a measured angle misfit of 7.6 ± 5.0°, whereas the stripe directions are multiples of 120°. The unit cells are drawn in black. The domain boundaries are highlighted by grey, dashed lines. (c) Line profiles along the lines A-D (see text for details). (d.1), (d.2) Structural models of the β-phase, according to ref [39], and the distorted β-phase (denoted as $\beta_{distorted}$), respectively. The model for the distorted β-phase was developed for this thesis. The unit cells are drawn in black, dashd lines. The characteristic symmetry directions are highlighted by colored arrows. Equivalent binding sites are highlighted by red circles. The unit cell of the distorted β-phase is constructed by a translocation of the original β-phase unit cell vector along the pair

stacking direction (turquoise) along one of the $< \mathbf{1\bar{1}0} >$ directions. The unit cell vector along the stripe direction is not changed. The translocation leads to a theoretical increase of the enclosed angle by 6.6°, in agreement with the experimental observation.

Model for the $\beta_{\text{distorted}}$-phase. The structural model for the distorted β-phase was developed for this thesis. According to the model introduced by ref [39], both stripe and the pair stacking directions of the undistorted β-phase domains are aligned along the $< 1\bar{1}0 >$ directions of the underlying Au(111) substrate. The structure of the $\beta_{\text{distorted}}$-phase can be explained by a slight modification of the β-phase model. The structural models are compared in Figure 4.5 (d.1) and (d.2). The unit cells are drawn by black, dashed lines. Equivalent binding sites are highlighted by red circles. The suggested unit cell of the $\beta_{\text{distorted}}$-phase can be constructed by shifting the unit cell vector along the pair stacking direction (turquoise) by one atomic distance along a specific $< 1\bar{1}0 >$ direction with respect to the pair stacking direction of the undistorted β-phase (blue). The theoretical value of the enclosed angle is 6.6°, in agreement with the measured value of 7.6 ± 5.0°. The unit cell vector along the stripe direction remains unchanged as the stripe directions of all phase domains (green), β and $\beta_{\text{distorted}}$, are still multiples of 120°. This modification of the unit cell is accompanied by a theoretical change of the unit cell length along the pair stacking direction from 2.02 nm (measured value 2.16 ± 0.22 nm) to 2.17 nm (measured value 2.24 ± 0.23 nm). The unit cell of the $\beta_{\text{distorted}}$-phase can be written as $\begin{bmatrix} 4 & 0 \\ -1 & n+1 \end{bmatrix}$ with parameter n close to 8.

4.2.3 Summary

TPT SAMs on Au(111) were prepared either from DMF-based solution or from gas phase and characterized by STM. Two distinct, ordered phases were observed in SAMs prepared from solution, denoted as α-phase and β-phase. Both phases were previously observed for TPT SAMs on Au(111) prepared in ethanolic solution[39]. The α-phase consists of densely-packed molecules arranged in the well-known $(2\sqrt{3} \times \sqrt{3})$R30° structure with two molecules per unit cell. The monomers occupy an area of 0.216 nm² and could adopt tilt angles of γ~13°. The β-phase is characterized by a point-on-line incommensurate $\begin{bmatrix} 4 & 0 \\ 0 & n \end{bmatrix}$ with parameter n close to 8 and eight molecules per unit cell. The monomers occupy an area of 0.288 nm² and adopt tilt angles of 33–49°[39]. SAMs prepared from the gas phase are characterized by the absence of α-phase domains. Instead, the largest part of the substrate surface is covered with β-phase domains. Moreover, domains of a slightly distorted β-phase were observed and identified. This

phase can be described by a $\begin{bmatrix} 4 & 0 \\ -1 & n+1 \end{bmatrix}$ lattice with n close to 8. Typical domains sizes for SAMs prepared either from DMF-based solution or from the gas phase are 10-100 nm. It has been found that SAMs prepared from gas phase are much better suited for STM experiments as they are completely free of mobile impurities or adsorbates that can lead to unstable imaging conditions. In the context of the investigation of cross-linking, TPT SAMs prepared from gas phase should, due to their structural analogy, constitute representive systems for TPT SAMs prepared from DMF-based solvent.

4.3 STM Study of Cross-Linking

In this section, STM data on the initial stage of cross-linking is presented and discussed in the first place, allowing for observing the influence of the electron impact on the local, molecular level and for deducing elementary mechanisms of cross-linking. Afterwards, the evolution of the monolayer towards the fully cross-linked state is investigated and the structural transformation associated with this is studied.

4.3.1 The Initial Stage of Cross-Linking

It is expected that the investigation of the initial stage of cross-linking will reveal deeper insight into the effect of the electron impact at the local molecular level. If the electron dose is so low that the monolayer is only slightly modified, i.e. the probability of each single monomer to be modified by the impinging electrons is low, the state of the irradiated monolayer is expected to resemble the pristine state, with the difference that pristine monolayer sections include modified spots which are spatially randomly dispersed and isolated from one another. Figure 4.6 compares STM data of pristine and slightly irradiated monolayer surfaces. All samples were prepared from the gas phase (see section 3.1.4). Figure 4.6 (a) shows the pristine TPT monolayer surface, which is characterized by β-phase domains of different orientations with respect to the underlying gold substrate. The bright protrusions in the center and left side of the image represent gold islands covered by TPT molecules in the same arrangement compared to the respective adjacent phase domains. Figure 4.6 (b) shows a surface section of the same sample that was exposed to 1 keV electrons by using the SEM with a dose of 0.5 mC/cm². It should be noted that the displayed images do not show the same sample location. The electron exposure causes the presence of coherent, depressed areas of various sizes within the domains (hereafter referred to as *dark spots*). Some spots are highlighted by

white arrows. Those dark spots have never been observed in non-irradiated monolayer sections. Figure 4.6 (c) shows a high-magnification image of the same sample where the dark spots were imaged with less stable imaging conditions. Figure 4.6 (d) shows a monolayer surface irradiated with 50 eV electrons using the flood-gun. Dark spots are also visible here, indicating that 50 eV electrons have a similar influence on the monolayer as 1 keV electrons. However, only limited STM data are available for monolayer surfaces irradiated with 50 eV electrons. Therefore, the dark spots are characterized in more detail with reference to Figure 4.6 (b).

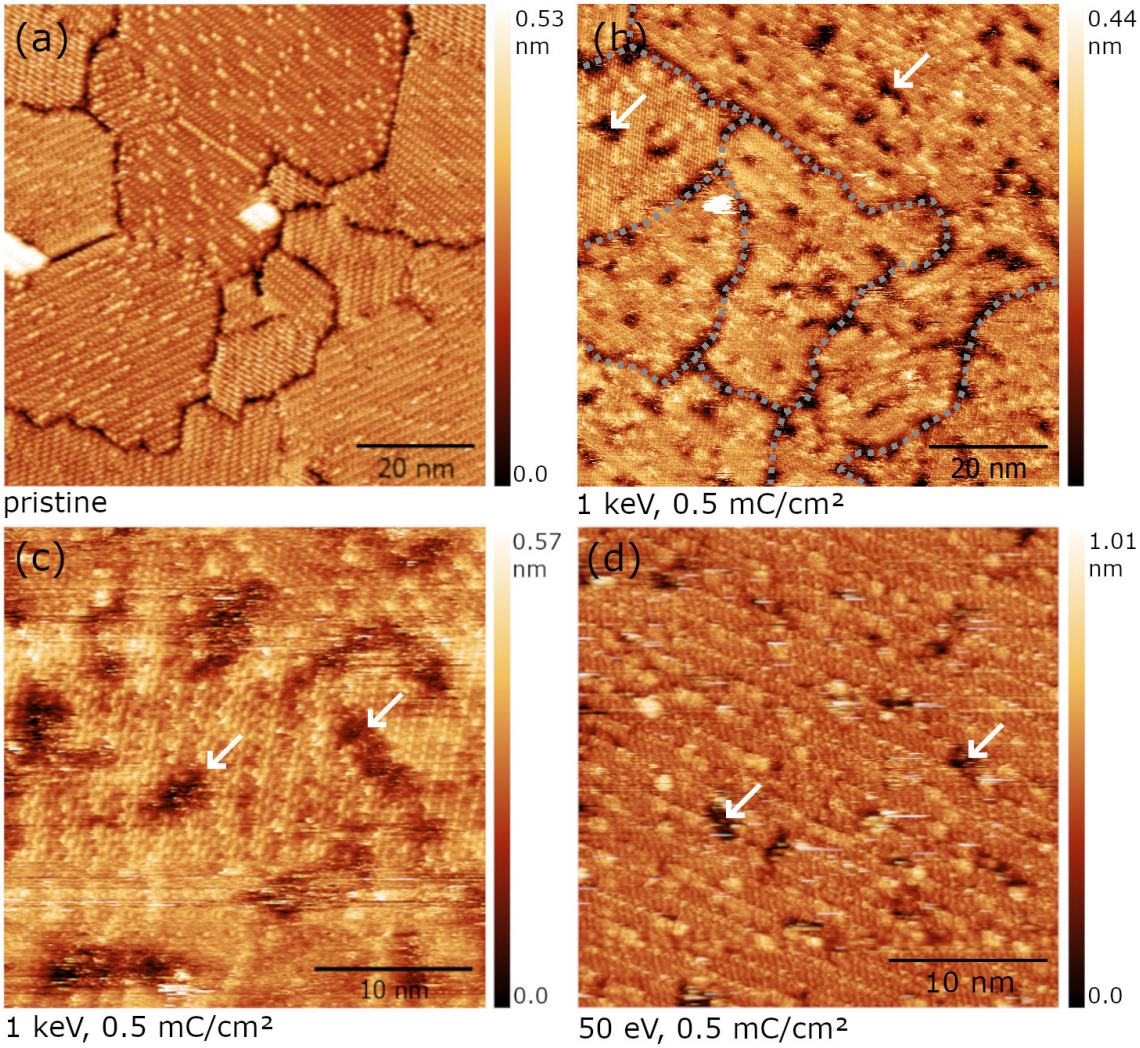

Figure 4.6: STM data contrasting (a) the pristine monolayer surface (U=+1.0V, I=30pA) and (b) an adjacent surface section that was irradiated with 1 keV electrons with a dose of 0.5 mC/cm². Tunneling parameters: (U=+0.45V, I=70pA). The presence of coherent, dark spots is observed (highlighted by white arrows). Domain boundaries are highlighted by grey, dashed lines. (c) High-magnification STM image (U=+0.45V, I=70pA) of the dark spots observed in (b). (d) High-magnification STM image (U=+1.0V, I=10pA) of a monolayer surface that was irradiated with 50 eV electrons with the same dose used in (b), showing the presence of dark spots as well. All data was acquired by using SAMs prepared from the gas phase (see section 3.1.4). All images were cross-talk corrected.

For this, their spatial distribution, their size distribution, and their (apparent) mean depth with respect to the SAM-ambient interface were evaluated using the STM image shown in Figure 4.6 (b) and by marking the spots (green) by employing the *Mark by Segmentation*-function of *gwyddion 2.41*. The marked image is shown in Figure 4.7 (a); the aforementioned distributions are shown in Figure 4.7 (b)-(d). Only the spots inside the phase domains were marked, whereas the domain boundaries were omitted. The size distribution of the dark spots (see Figure 4.7 b) is plotted as a function of the spot area, which is represented in units of 0.288 nm^2, corresponding to the molecular area in the β-phase. The size distribution is characterized by decay towards large areas and an average size of 5–6 molecular areas. The distribution seems to peak at two molecular areas, but spots up to 33 molecular areas in size can be observed. It should be noted that due to the overlap of smaller spots larger spots may also occur. To determine the size distribution of the spots more precisely, a larger STM dataset is required. The spatial distribution of the dark spots (see Figure 4.7 c) was evaluated by dividing the STM image into equal sections (see inset) and then counting the number of spots in each section. The spatial distribution can be approximated by a Poisson distribution (black, dashed line), indicating that the dark spots are random and independent of each other. To gain a higher statistical significance, however, a larger STM data set is required. It should also be taken into account that spots of smaller size can overlap, thus distorting the determination of their lateral distribution. The areal spot number density is $n_{spots}^{STM} \approx 2 \pm 1 \times 10^{12}\,cm^{-2}$ with an estimated measurement uncertainty of 50 %. Notice that the counting accuracy of smaller spots less than 3 molecules may be lower compared to larger spots. The mean depth distribution of the dark spots (see Figure 4.7 (d)) was obtained by determining the mean depth for every dark spot with respect to the SAM/ambient interfacial area. This was done by averaging the measured depth for each individual pixel. The mean depth distribution is characterized by a pronounced increase at small areas and a level-off behavior towards large areas. The data were analyzed by using an empirical fit according to Equation 4.1 (black, dashed line). However, the STM generally does not measure the physical height of surface features as both topographical and electronic variations of the sample surface can influence the tunneling current. Figure 4.7 (d) reveals that the measured depth of small spots is lower compared to large spots. This may be due to the finite size of the tip apex or due to the finite reaction speed of the feedback control system. For large spot areas, the measured depth is 1.4 ± 0.1 Å.

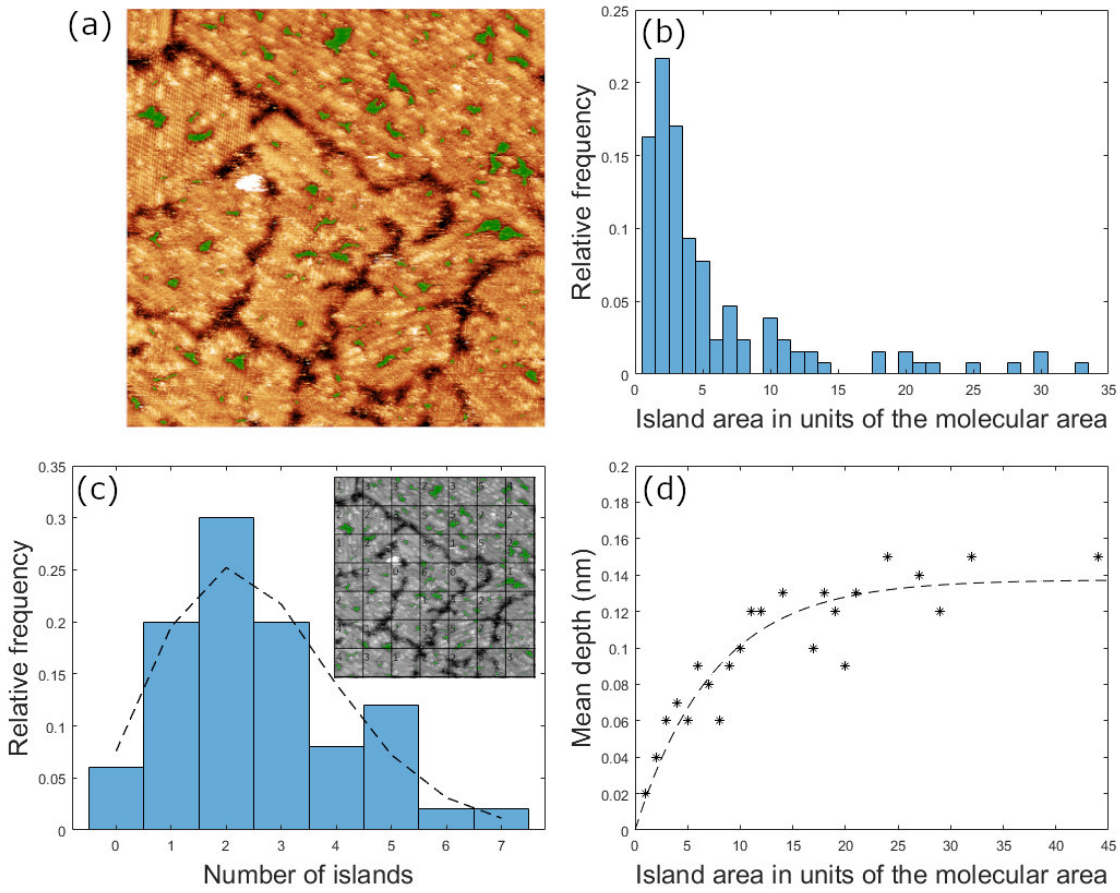

Figure 4.7: Characteristics of the electron irradiation-induced dark spots. (a) The STM image shown in Figure **4.6** (b) was evaluated by using the *Mark by Segmentation*-function in gwyddion v.2.41. (b) Size distribution of the dark spots, plotted as a function of the molecular area in the β-phase. (c) Lateral distribution of the dark spots, approximated by a Poisson-distribution (black, dashed line) with parameter $\lambda = 2.6$. The sectioning of the STM image is shown in the inset. (d) Apparent mean depth of the dark spots with respect to the SAM/ambient-interfacial area as a function of the depression area. The data was fitted empirically according to Equation 4.1 (black, dashed line).

It is reasonable to assume that the dark spots are due to electron irradiation-induced modifications of the monolayer, i.e. modifications of the carbonaceous matrix and/or the sulfur-gold interface. As discussed in section 2.3.5, it is expected that locally cross-linked spots within the TPT layer will appear as depressions in STM images and that the major contribution to the STM image contrast will result from the cleavage of S–Au bonds. The STM data allows for estimating the cross-section $\sigma^{STM}_{S-Au\ cleav.}$ for the S–Au bonds to be cleaved by an impinging electron based on the area fraction of the dark spots:

$$\sigma^{STM}_{S-Au\ cleav.} = a_{dark\ spots} \times e/d \qquad \text{Equation 4.2}$$

Here, $a_{dark\ spots}$ denotes the area fraction of the dark spots, d the applied electron dose and e the elementary charge.

The area fraction of the dark spots is $a_{dark\ spots} = 3.2 \pm 0.7\%$, which gives $\sigma^{STM}_{S-Au\ cleav.} = 1.0 \pm 0.3 \times 10^{-17}\text{cm}^2$. In this context the measurement error of $a_{dark\ spots}$ was estimated to 20% of the total value. This value is in good agreement with the cross-section of the S–Au bonds to be cleaved by the impingement of 1 keV electrons, i.e. $\sigma^{XPS}_{S-Au\ cleav.} = 1.2 \pm 0.2 \times 10^{-17}\text{cm}^2$, which was derived from XPS data (see section 4.1.2). Therefore, it is reasonable to assume that the dark spots observed in the STM images represent areas of cleaved S–Au bonds. It should be noted that the STM data allows an estimate of the areal number density of cleaved S–Au bonds rather than the (projected) areal number density of, for example, rehybridized carbon centers or cleaved C–H bonds. This is due to the fact that there is only one S–Au bond, but 13 carbon centers per monomer. Provided that the dark spots represent areas characterized by cleaved S–Au bonds, we have to answer the question why the cleavage of S–Au bonds is not evenly distributed over the monolayer. This would probably lead to the presence of molecular-sized spots in the STM images which are randomly distributed. However, the existence of extensive coherent spots with areas of up to several tens of molecules is observed instead. The appearance of dark spots upon electron irradiation may be explained by the propagation of radical polymerization reactions through the carbonaceous matrix of the monolayer, as previously proposed by Amiaud *et al.* based on HREELS data and irradiation experiments with 6 eV primary electrons (see section 2.2.1). These reactions may be initiated by the impact of impinging electrons, which produce the first radical and can be terminated after several propagation steps. Cross-linking of the carbonaceous matrix can then be accompanied by the cleavage of S–Au bonds, which gives the observed contrast in the STM images (see section 2.3.5). It is reasonable to assume that each dark spot represents a completed radical chain reaction initiated by the impact of a single electron. Since the monolayer has been homogeneously irradiated, it can be expected that independent chain reactions are initiated at random locations within the molecular layer, which is in good agreement with the Poisson-like areal distribution of the dark spots. In this context, the propagation of the chain reactions can be linear or in a rather ramified way, as highlighted in Figure 4.8. Figure 4.8 (a) also shows the high-magnification STM image shown in Figure 4.6 (c). Figure 4.8 (b) and (c) schematically show the potential propagation pathways through the monolayer: linear (b) and ramified (c). However, the available STM data do not allow this hypothesis to be further clarified.

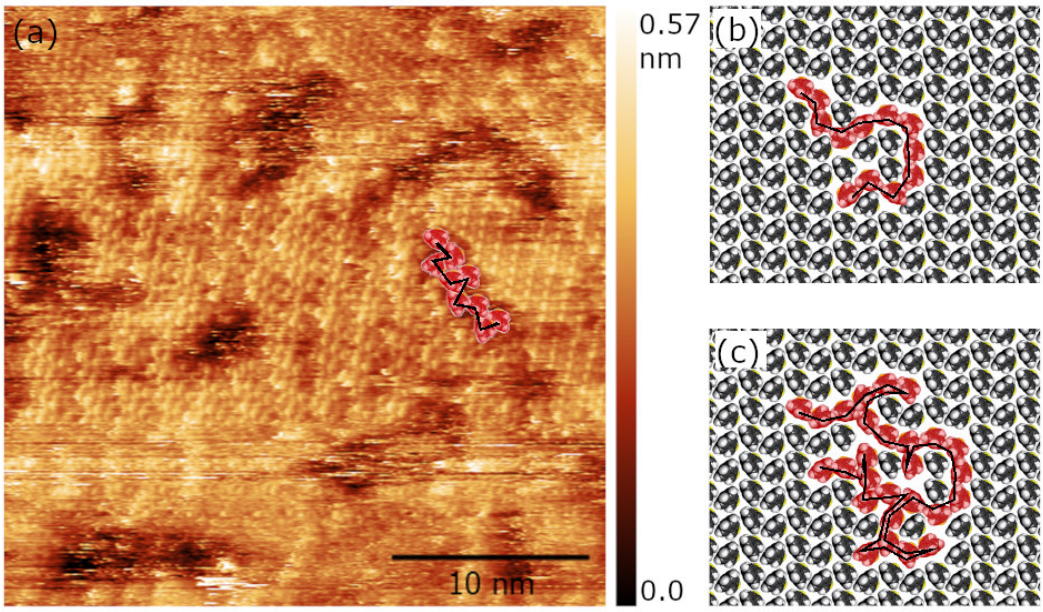

Figure 4.8: Potential chain reaction pathways that may lead to dark spots of observed shape. (a) High magnification STM image shown in Figure 4.6 (c) as well. (b) and (c) Potential propagation pathways through the monolayer; linear (b) and ramified (c).

According to Amiaud *et al.*[14], cross-linking within a TPT SAM can be achieved via radical chain reactions starting with a resonant *EA* process at 6 eV. The formation of the first radicals, which initiates chain reactions, can then proceed via electronic rearrangement or via DEA. As the irradiation was performed with 6 eV primary electrons, i.e. below the ionization and excitation thresholds, EA should be the major mechanism causing chemical transformations of the monolayer[113],[114]. Therefore, other electron-molecule interactions that could lead to the formation of the first radicalized were excluded[14]. The first ionization potential of benzene is 9.3 eV and the ionization potential of naphthalene is 8.2 eV[115]. TPT on Au(111) can therefore have the first ionization potential between 6 eV and 9 eV. However, as the irradiation experiments in this work were carried out with 50 eV and 1 keV PEs (the formation of dark spots was observed for both PE energies, see Figure 4.6), all electron-induced fragmentation pathways must be considered in the first place. Nevertheless, the STM data suggests that the impinging electrons initiate radical chain reactions within the monolayer, and these processes may also account for cross-linking induced by electron irradiation of aromatic SAMs in general, as already mentioned by Amiaud *et al.*[14]

In the following, it is assumed that the dark spots observed in the STM images result from the generation of one (first) radical each, which then initiate radical chain reactions. To investigate the potential contribution of the emitted 6 eV SE to the formation of the first radicals, the areal number density of the dark spots observed in the STM image shown in Figure 4.6 (b), n_{spots}^{STM}, is

compared with the expected areal number density of reactive EA events deduced from HREELS data (see below), n_{rEA}^{HREELS}. Reactive EA events are defined as EA events that eventually lead to the formation of at least one intermolecular carbon-carbon bond. n_{rEA}^{HREELS} can be estimated by employing the estimated reactive EA cross-section $\sigma_{rEA}^{HREELS} \sim 1.2 \times 10^{-16}\ \mathrm{cm}^2$, introduced by Amiaud *et al.* based on the observed loss of aromaticity (see section 2.2.1).

The expected areal number density of reactive EA events is estimated by employing the following equation:

$$n_{rEA}^{HREELS} = n_{SE,6eV} \times \frac{\sigma_{rEA}^{HREELS}}{A_{mol}} \qquad \text{Equation 4.3}$$

where A_{mol} denotes the area occupied by a single molecule in the β-phase, which is 0.288 nm^2[39] and $n_{SE,6eV}$ denotes the areal number density of SEs emitted within the window of the resonance, i.e. with kinetic energies of 6.0 ± 1.5 eV[14].

$n_{SE,6eV}$ can be determined by employing the following equation:

$$n_{SE,6eV} = SEY \times f_{SE,6eV} \times n_{PE} \qquad \text{Equation 4.4}$$

where SEY denotes the PE kinetic energy-dependent secondary electron yield, $f_{SE,6eV}$ the fraction of the overall distribution of SE produced within the window of the resonance, and d_{PE} the PE areal number density.

The SEY for incident 1 keV PE impinging on gold surfaces was determined by Gonzales *et al.*, which gives 1.65 for a clean surface and 1.85 for a contaminated surface[116]. $f_{SE,6eV}$ was graphically estimated to 5–10 % by Houplin *et al.*[53] for 50 eV PE impact. This value should be similar in case of 1 keV PE impact, since the low-energy tail of the SE energy distribution does not change significantly with the increase in the PE kinetic energy[117]. n_{PE} is derived by dividing the applied PE dose d_{PE} by the elementary charge e, yielding $n_{PE} = 0.5 \pm 0.1\ \mathrm{mC} \times \mathrm{cm}^{-2}/e = 3.1 \pm 0.7 \times 10^{15}\mathrm{cm}^2$. Accordingly, $n_{SE,6eV}$ is estimated to $4.1 \pm 1.7 \times 10^{14}\mathrm{cm}^{-2}$. The expected areal number density of reactive EA events upon 1 keV electron exposure with a dose of 0.5 $\mathrm{mC/cm}^2$ is therefore $n_{rEA}^{HREELS} = 1.7 \pm 0.7 \times 10^{13}\mathrm{cm}^{-2}$, which should be compared with $n_{spots}^{STM} = 2.0 \pm 1.0 \times 10^{12}\mathrm{cm}^{-2}$. The comparison of the areal number densities shows that n_{spots}^{STM} is roughly one order of magnitude lower than n_{rEA}. This result appears counterintuitive, as n_{rEA} was derived from the reactive EA cross-section determined from the HREELS data[14]. Assuming that each dark spot is created upon formation of a TPT monomer radical, n_{spots}^{STM} is

expected to be equal to or higher than n_{rEA}^{HREELS}, especially since further reaction pathways, such as *neutral dissociation* (ND) and/or *dissociative ionization* (DI) may contribute to the formation of radicalized monomers at higher energies[118]. It must be pointed out that, however, the reactive EA cross-section σ_{rEA}^{HREELS} was overestimated by Amiaud *et al.*[14] by neglecting the propagation of radical chain reactions. HREELS data show that 6 eV electron irradiation with a dose of 50 electrons per molecule leads to a 47–53% decrease of the aromatic C–H stretching feature. As one TPT monomer has 13 aromatic C–H groups, on average 6–7 aromatic carbon centers are converted to aliphatic carbon centers after irradiation. Without taking into account the propagation of radical chain reactions, i.e. only the reaction between two monomers is considered (see Figure 2.4), the creation of one radical center leads to the formation of two aliphatic groups. Assuming that each DEA event leads to a reaction with an adjacent monomer, on average 3 DEA events per monomer are required to cause the observed ~50% loss of aromaticity. Considering that every monomer is irradiated by 50 electrons and occupies an area of ~20 Å², the reactive EA cross-section is therefore $\sigma_{rEA}^{HREELS} \sim 1.2 \times 10^{-16}\text{cm}^2$.

The theoretical considerations by Amiaud *et al.* are extended in the following by considering the propagation of radical chain reactions: When considering the propagation with an average of n monomers involved, every DEA event should cause the formation of $2n$-2 aliphatic groups within the monolayer (see Figure 4.9), which means that n-1 times **more** aliphatic groups are created compared to the case when neglecting the propagation. Therefore, the reactive EA cross-section $\sigma_{rEA}^{HREELS} \sim 1.2 \times 10^{-16}\text{cm}^2$ estimated by Amiaud *et al.*[14] must be divided by (n-1), which leads to

$$\sigma_{rEA}^{HREELS}(n) \sim \frac{1.2 \times 10^{-16}\text{cm}^2}{n-1} \qquad \text{Equation 4.5}$$

The STM data indicates that n = 5–6 monomers are involved in the radical chain reactions on average, which leads to $\sigma_{rEA}^{HREELS}(n = 5\text{–}6) \sim 2.2 \pm 0.3 \times 10^{-17}\text{cm}^2$. Employing Equation 4.3 allows then for estimating $n_{rEA}^{HREELS}(n = 5\text{–}6) \sim 3.8 \pm 1.9 \times 10^{12}\text{cm}^2$. This value is in good agreement with the areal number density of the dark spots observed in the STM image shown in Figure 4.6 (b), which is $n_{spots}^{STM} = 2.0 \pm 1.0 \times 10^{12}\text{cm}^{-2}$. Hence, the present data indicates that the dark spots observed in the STM images were created by one EA event each, followed by the creation of the first radical.

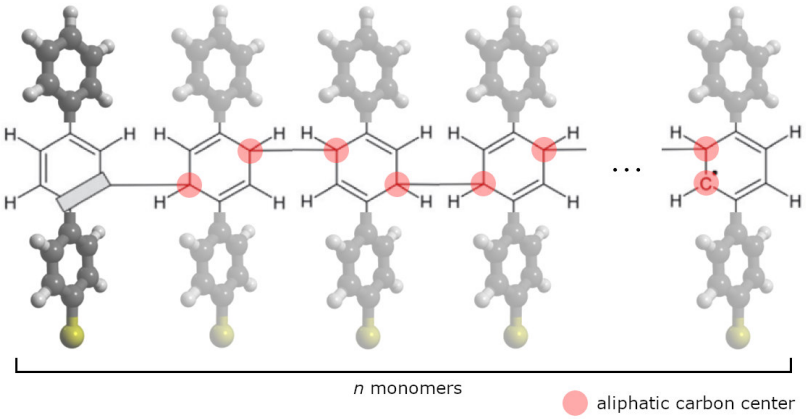

Figure 4.9: Schematic illustration showing that the propagation of radical chain reactions involving *n* monomers is expected to cause the formation of 2*n*-2 aliphatic groups (highlighted in red). This hypothesis is based on the proposed mechanisms for electron induced loss of aromaticity going along with cross-linking within a TPT SAM starting with electron attachment at 6 eV[14]. The gray shaded area is to be substituted to accommodate for the different initiators (routes (a) or (b), see Figure 2.4).

As previously discussed, EA could be the major mechanism that causes the initiation of radical chain reactions with 5–6 TPT monomers involved on average, which appear as dark spots in the STM images. It should be noted, however, that the contribution of other (non-resonant) scattering processes[118], which may lead to the formation of first radicalized monomers, cannot be excluded, since the irradiation experiments in this work were performed with 50 eV and 1 keV electrons. In particular, HREELS data indicates that electron impact ionization plays a significant role in the chemical transformation of the carbonaceous matrix associated with hydrogen loss under 50 eV electron impact, with impact electronic excitation contributing only marginally (see section 2.2.1). On the contrary, the data indicates that reactive processes induced by the low-energy SEs seem to contribute only marginally to hydrogen loss. Following the radical chain reaction mechanism proposed by Amiaud *et al.*, however, chain reactions may propagate nearly without hydrogen loss, which is due to the partial rehybridization of the carbon centers from sp^2 to sp^3. Hence, the significance of electron impact ionization for the creation of the first radicals which can initate radical chain reactions is not clear. Finally, the agreement between the areal number densities n_{rEA}^{HREELS} and n_{spots}^{STM} indicates that EA must not be neglected when estimating which processes are contributing to the creation of molecular radicals in the TPT monolayer.

4.3.1.1 Proposal for Possible Chain Termination Mechanisms

Possible mechanisms leading to the termination of the radical chain reactions are not discussed in the literature[14] and the STM data does not provide any information. However, assumptions

about possible mechanisms can be made. By presuming the creation of isolated molecular radicals that initiate chain reactions within the monolayer, it is assumed that termination by recombination of two radicals makes only a marginal contribution as long as the respective chain reactions propagate well-separated from each other in the SAM. It should be noted that the SAM monomers are bound to the substrate and thus almost immobilized, which distinguishes the current type of 2D chemistry from conventional chemical reactions in the gas or liquid phase.

We propose two different potential chain termination mechanism: i) Termination occurs due to steric hindrance of the cross-linked molecular island. It is expected that the cross-linking between two adjacent molecules will be accompanied by molecular reorientations. While single molecules should have sufficient translational and rotational degrees of freedom, cross-linking between several molecules can lead to reduced mobility of the monomer constituting the reaction front. ii) Termination occurs upon contraction of the cross-linked molecular island due to the formation of intermolecular covalent bonds. After several propagation steps, the front radical is separated by a gap from adjacent pristine molecules, thus terminating the propagation.

4.3.1.2 Alternative Interpretation of the Dark Spots

As discussed previously, the dark spots observed in the STM images can be ascribed to locally cross-linked segments of the monolayer, which are accompanied by S–Au bond cleavage. In this section, however, two alternative interpretations of the dark spots are discussed – first, the dark spots result from an irradiation-induced reconstruction of the underlying gold substrate, in particular from the formation of gold vacancy islands in the topmost Au(111) layer, and second, the dark spots result from the desorption of single TPT molecules and/or molecular fragments induced by electron irradiation and the subsequent reorientation of adjacent monomers. Figure 4.10 visualizes the two types of electron-induced modifications of the TPT/Au(111) system under consideration, which could be represented by dark spots in STM images.

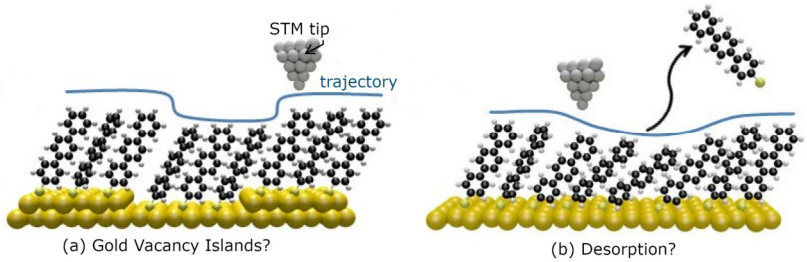

Figure 4.10: Schematic overview of two alternative interpretations of the dark spots. a) Gold vacancy islands within the first gold layer. b) Desorption of single molecules and/or molecular fragments and subsequent reorientation of the adjacent monomers.

a) Gold vacancy islands, often referred to as *etch pits*, are typically formed during the adsorption of alkanethiol SAMs on Au(111)[119],[120],[121],[122]. The assignment of the dark spots to the irradiation-induced formation of gold vacancy islands only makes sense if, regardless of the underlying mechanism, the depth of the vacancy islands is ~0.24 Å, which corresponds to the theoretical height of a single Au(111) gold layer[109],[111] as well as the height of the Au(111) step edges measured by STM. In this model (see Figure 4.10 (a)), the TPT monolayer is still in its pristine state, resulting in a nearly topographical contrast in the STM images. Lateral variations of the electronic structure of the monolayer-substrate system that result from cross-linking are not considered here. Since the tip radius of the STM probe prepared by electrochemical etching is typically several nanometers or tens of nanometers[123], it is not surprising that the depth of small depressions can be measured less accurately than the depth of large ones. However, it is expected that the saturation value of the fitting curve shown in Figure 4.7 (d) will provide a reliable value for the mean depth of large-area vacancies. In contrast to the theoretical depth of ~0.24 Å of Au vacancy islands, the saturation value of the fitting curve was determined to be 0.14 ± 0.01 nm, which is significantly different from the theoretical value.

The assignment of the dark spots to gold vacancy islands is in further contradiction to the absence of Au adatom islands in the vicinity of the spots as well as to the unchanged shape of the Au step edge contours after the irradiation process. Since gold vacancy islands can only be formed by the ejection of Au atoms from the topmost gold layer, it is expected that these Au atoms would either diffuse into the adjacent region of the depressions and possibly coalesce into Au adatom islands, or would diffuse to the surrounding step edges of the gold substrate during or after irradiation. It must be considered, however, that the lateral diffusion of the gold adatoms should be inhibited by the chemisorbed monolayer. As mentioned above, gold vacancy islands typically emerge during the adsorption of alkanethiol SAMs on Au(111),

which is a consequence of release of Au atoms mediated by the herringbone relaxation[122]. Here, the adatoms merge with the surrounding step edges, which is why gold adatom islands are typically not observed for alkanethiol SAMs on gold. In contrast, the morphology of arenethiol-SAMs is typically characterized by the presence of only very few vacancy islands, where gold adatom islands are formed as a consequence of an increased diffusion barrier and of a resulting decrease in the mobility of surface Au atoms[109].

Within the experiments for this thesis, electron exposure of TPT SAMs on Au(111) was not accompanied by the formation of additional gold adatom islands. The STM image sequences presented in Figure 4.11 show the same sample position before (left) and after the first irradiation step (right) by SEM. The SAMs were irradiated with electron doses of 0.3 mC/cm² (upper sequence) and 2.0 mC/cm² (lower sequence), respectively.

From the measured mean depth of the dark spots of only 0.14 ± 0.01 nm and the absence of gold adatom islands after electron exposure it can be concluded that the observed dark spots cannot be assigned to gold vacancy islands.

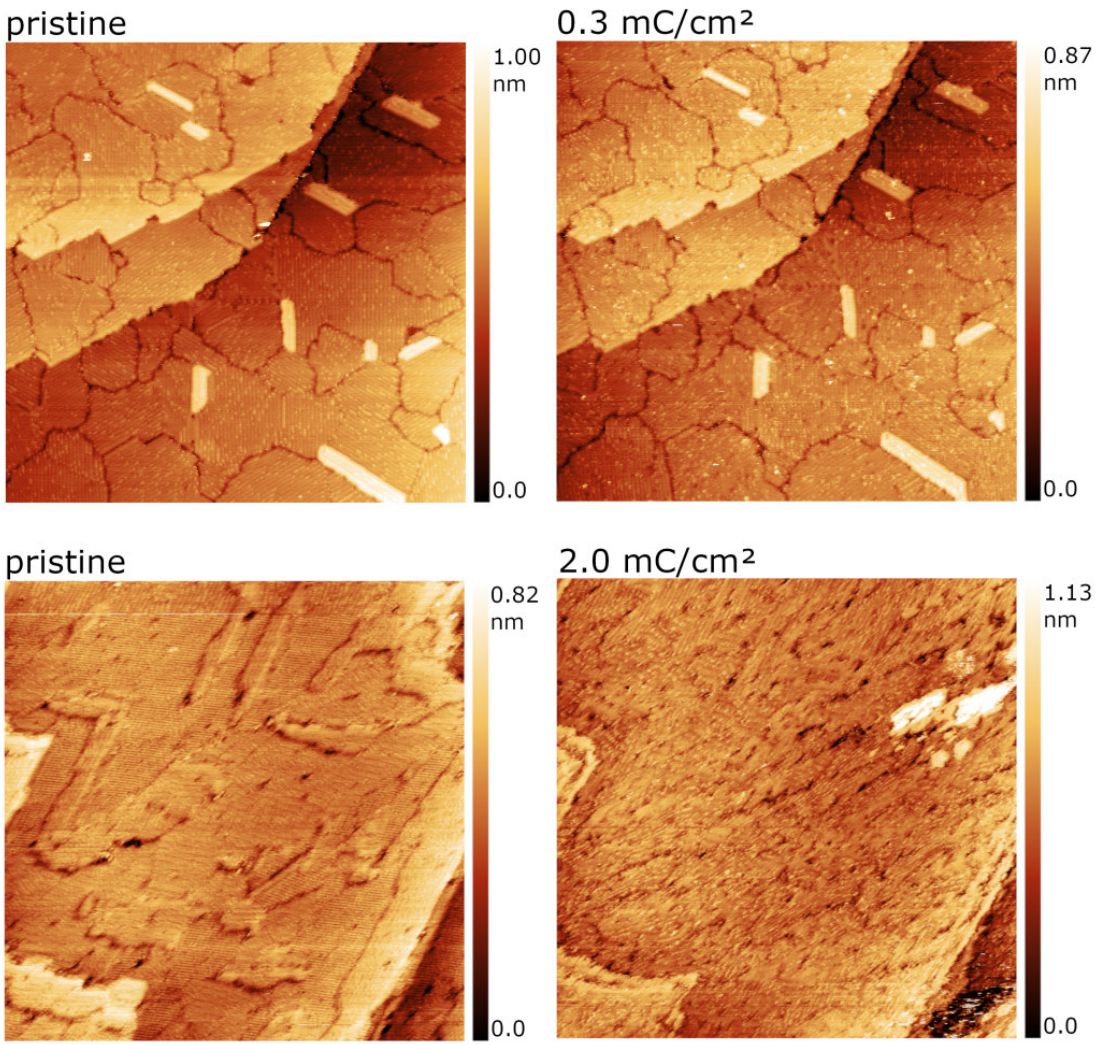

Figure 4.11: STM overview scans of TPT SAMs before and after 1 keV electron exposure by SEM. The SAM shown in the upper image sequence (cross-talk corrected) was prepared from the gas phase (see section 3.1.4). Tunneling parameter: (U=+0.4V, I=30 pA). The SAM shown in the lower image sequence (not cross-talk corrected) prepared from DMF-based solution (see section 3.1.3). Tunneling parameter: (left: U=+0.45 V, I=30 pA, right: U=-1.2 V, I=30 pA). The applied doses are displayed in the upper left corners. The irradiation process is apparently not accompanied by the formation of gold adatom islands. The white protrusion in the upper right corner of the 2 mC/cm²-irradiated SAM is due to interactions of the sample surface with the scanning probe.

b) Desorption of SAM material. The evolution of the carbon content of aromatic SAMs during electron irradiation is discussed in section 2.2.3. XPS data obtained in this thesis (see section 4.1.1) indicates a loss of the carbon content by a few percent after exposing the SAM to electron doses less than 5 mC/cm². The area percentage of the dark spots shown in Figure 4.6 (b) is ~3.2%, which is close to the value for the reduction of the carbon content. However, the dark spots do not appear to represent empty voids within the monolayer, but still contain molecular constituents. This is illustrated by Figure 4.12, which shows a three-dimensional view of a selected spot. However, the desorption of individual molecules and/or molecular

fragments, accompanied by an orientational collapse of surrounding molecules (see Figure 4.10 (b)) as a result of a locally reduced areal molecular density cannot be excluded.

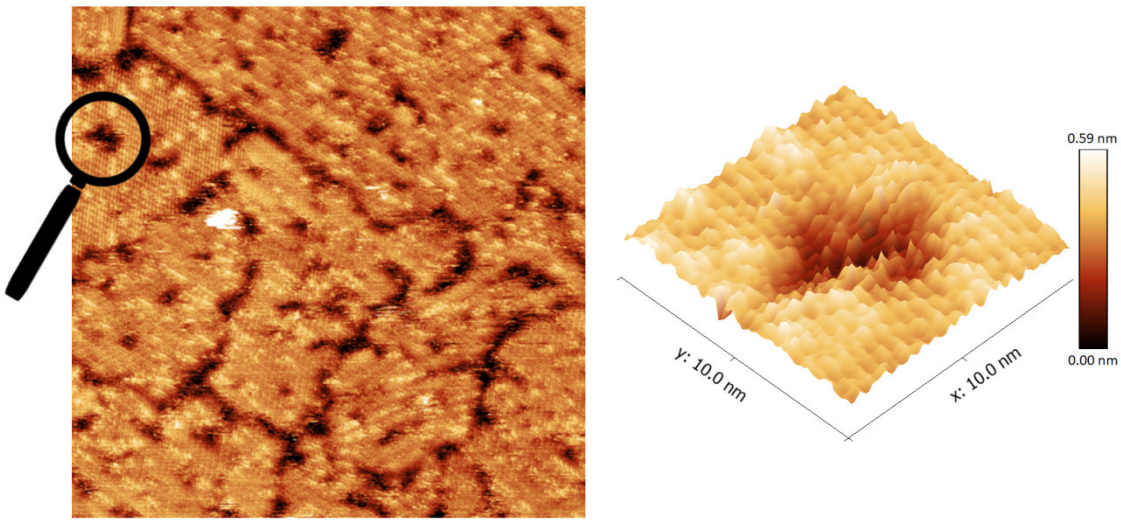

Figure 4.12: 3D view of one selected depression with larger area. Molecular corrugations are still visible, yet more disordered compared to the pristine SAM. The desorption of single molecular moieties cannot be excluded.

There are two reasons why a local orientational collapse of the monomers can appear as dark spots in STM images: a) the tilt angles of the monomers are locally increased (topographical contrast), and b) the correlation between the molecular orientation, the areal molecular density, and the local work function leads to a local increase of the tunneling barrier. To exclude the first point, AFM experiments should be performed. Case b) is discussed in more detail below.

The correlation between the molecular orientation, the areal molecular density, and the local work function has been recently investigated by Biere *et al.*[124] using KPFM and TPT SAMs on Au(111) and Ag(111). A schematic diagram illustrating this correlation is shown in Figure 4.13.

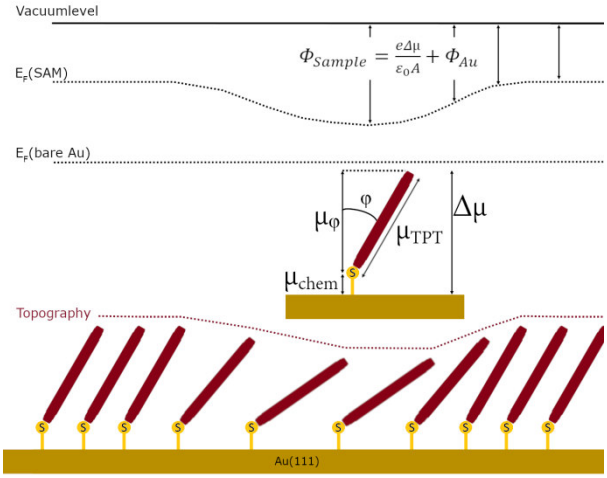

Figure 4.13: Correlation between the areal density of the molecules, the molecular orientation and the work function of the sample. The local decrease of the molecular area density leads to a structural collapse, which is accompanied by an increase of the tilt angle of the concerned molecules. It is expected that the local collapse of the molecules will result in the appearance of depressions in the STM images for two reasons: 1) the topographic contrast due to the local increase of the inclination angle, and 2) the electronic contrast, due to the local increase of the work function and consequently the local increase of the tunneling barrier (see text for details).

The local work function of a sample surface, Φ_{sample} can be modified by the presence of adsorbate molecules. It can be written as the sum of the local work function of the adsorbate layer, $\Phi_{adsorbate}$, and the metal substrate, Φ_{metal}, that is, $\Phi_{sample} = \Phi_{adsorbate} + \Phi_{metal}$ [124]. For SAMs, the work function of the monolayer, Φ_{SAM} (= $\Phi_{adsorbate}$), is a function of the molecular dipole moment, in particular, a function of the component perpendicular to the sample surface, $\Delta\mu$. Furthermore, Φ_{SAM} depends on the area per molecule, A. Φ_{SAM} can be written as $\Phi_{SAM} = e\Delta\mu/\varepsilon_0 A$ [124]. The molecular dipole $\Delta\mu$ is split up into two components: the sulfur-substrate bond, μ_{chem}, and the effective aromatic moiety, μ_φ. Hence, $\Delta\mu = \mu_\varphi + \mu_{chem}$, where μ_φ depends on the tilt angle φ of the molecules.

As already shown by Biere *et al.* [124], the local work function for densely packed phases of TPT on Au(111) is significantly lower (~300 meV) compared to less densely packed phases. Desorption of SAM material, as schematically shown in Figure 4.10 (b), may therefore yield an electronic contrast in STM images due to the local decrease of $\Delta\mu$ and the local decrease of the areal monomer density, which leads to the appearance of dark spots in (constant-current) STM images (see Figure 4.13). Further investigations may include atomic force microscopy (AFM) experiments, which provide almost pure topographic contrast, and KPFM experiments, which measure the local working function within the dark spots and within the unaffected areas of the monolayer surface.

4.3.2 Evolution towards the Fully Cross-Linked State

The previously presented STM results provide information about electron-induced modifications of the TPT monolayer-substrate system at the initial stage of cross-linking. In the following, the STM data on the evolution of the monolayer-substrate system towards a fully cross-linked monolayer is presented and discussed.

4.3.2.1 Reduction of the Structural Order

XPS data indicates that the 50 eV and 1 keV electron irradiation-induced loss of molecular order in TPT SAMs on Au(111) is most pronounced for irradiation doses less than 10 mC/cm² (see section 4.1.1). The STM data presented in this section is in agreement with this finding. Figure 4.14 displays STM scans of (a) the pristine monolayer surface, (b)-(d) monolayers that were exposed to doses of 2.5, 10, and 25 mC/cm², respectively. All samples were prepared from DMF-based solution and irradiated with 50 eV electrons. The pristine SAM (a) is characterized by the presence of phase domains of high molecular order, as discussed thoroughly in section 4.2.1. Some domain sizes range from 10 to 100 nm. Domain boundaries are highlighted by black lines. Moreover, the image reveals the presence of Au adatom islands which are covered with TPT molecules. The irradiated SAM shown in (b) is characterized by the presence of dark spots that may be ascribed to locally cross-linked areas of the monolayer, which have evolved through the propagation of radical chain reactions (see section 4.3.1). Electron exposure with a dose of 10 mC/cm² (c) leads to a significant reduction of the long-range order of the monolayer. The surface is characterized by small but well-ordered phase domains (some are framed by green lines) with sized typically less than 10 nm. The internal molecular structure is similar to the structures observed in the pristine SAM, indicating that the corresponding areas were only slightly affected during electron exposure. The domains appear to be "embedded" in a rather amorphous matrix (some parts are framed by blue lines) that could not be resolved molecularly. This matrix appears darker compared to the bright, well-ordered domains, which indicates that these areas were subject to rather significant cross-linking. In the pristine SAM, ordered domains are separated by domain boundaries, which also appear darker in STM images but are only ~2 nm wide and are still characterized by a relatively high degree of molecular order. Here, molecular phase domains are separated by apparently amorphous areas that are 5-10 nm wide. Electron irradiation with a dose of 25 mC/cm² (d) apparently leads to a complete loss of long- and short-range molecular order. Molecular phase

domains that are identical or similar to pristine phase domains could not be observed. However, the surface morphology is still characterized by brighter areas of 5-10 nm in size (framed by green, dashed lines), separated by darker structures of branched shape (framed by blue, dashed lines). The brighter appearance can be explained by a certain residual molecular order. As indicated by (c) and discussed in detail in section 2.3.5, monolayer areas that were more affected by electron exposure should appear darker in constant-current STM images. XPS data also indicates a certain residual order after electron exposure at 25 mC/cm², since the conformational and orientational order of the monolayer still shows a certain tendency to decrease when the irradiation dose is increased from 25 mC/cm² to 50 mC/cm² (see section 4.1.1).

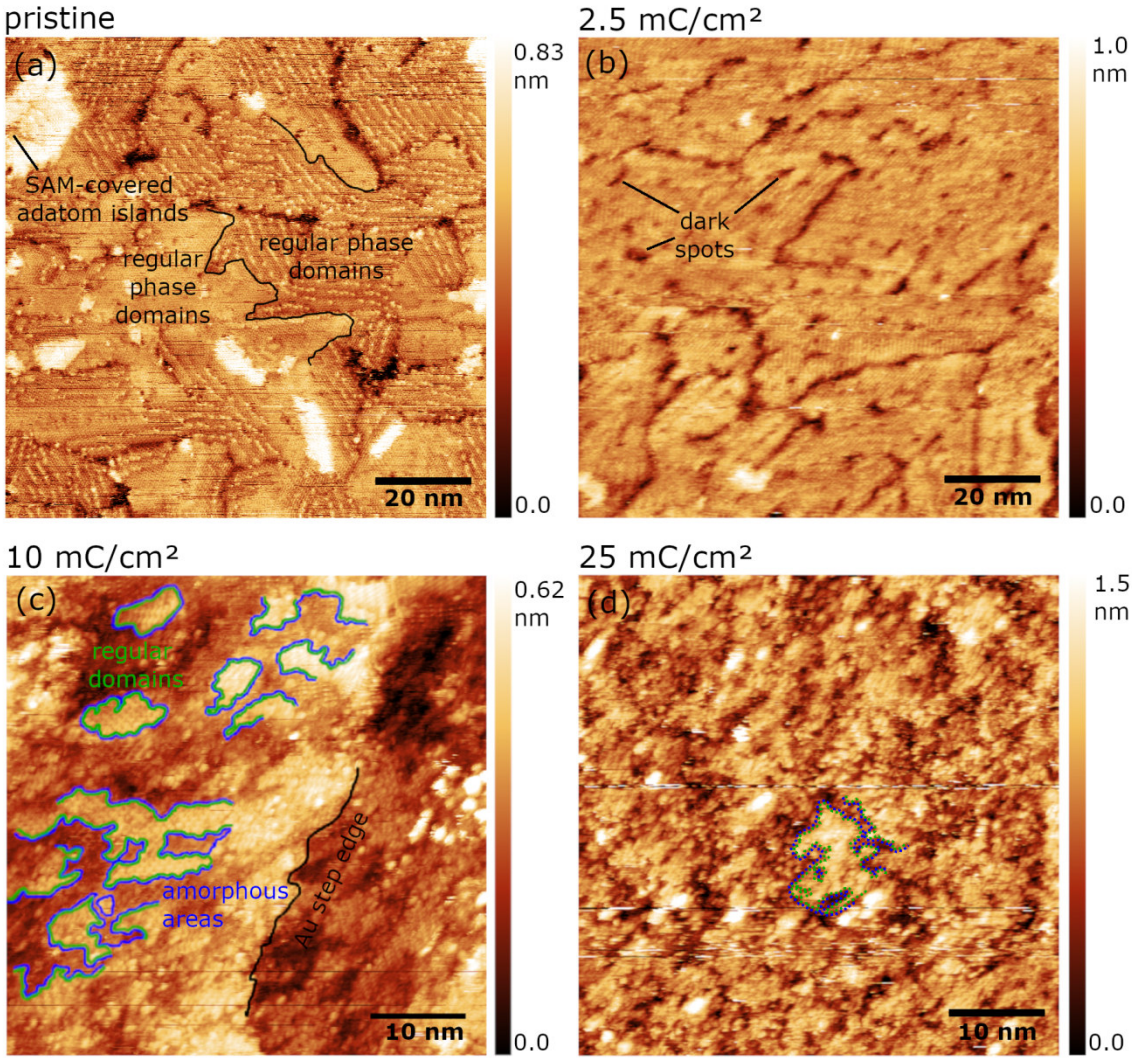

Figure 4.14: Structural evolution of the monolayer upon 50 eV electron exposure. SAMs were prepared from DMF-based solution. (a) The pristine TPT SAM is characterized by the presence of highly-ordered phase domains and Au adatom islands covered by TPT molecules. Tunneling parameter: (U=+1.0V, I=30pA) The image is cross-talk corrected. (b) Electron exposure with a dose of 2.5 mC/cm² causes the formation of dark spots. Tunneling parameter: (U=-1.2V, I=10pA). The image is not cross-talk corrected. (c) Exposing the monolayer to 10 mC/cm² causes a significant reduction of the long-range molecular order. Ordered phase domains with sizes < 10 nm are still visible (marked by green lines). The domains are surrounded by darker areas of low order (marked by blue lines) that may be ascribed to rather cross-linked parts of the monolayer. Tunneling parameter: (U=-1.2V, I=10pA). The image is not cross-talk corrected. (d) Electron exposure to 25 mC/cm² causes the loss of long- and short-range order. However, some residual order might be left as indicates by brighter parts of the monolayer (green), surrounded by darker parts (blue) of branched shape. Tunneling parameter: (U=-1.2V, I=10pA). The image is not cross-talk corrected.

The STM data shown in Figure 4.15 supports the previous observations regarding the loss of long-range molecular order upon electron exposure. Electron exposure by SEM with a dose of 2 mC/cm² led to a significant reduction of the average phase domain size. Figure 4.15 (a) and (b) show the pristine SAM surface, revealing the presence of rather large phase domains (primarily β-phase domains). Some domain boundaries are marked by green lines in (a).

Figure 4.15 (c) and (d) show the monolayer at the same sample location (see the nearly preserved contours of the Au step edges) after electron irradiation. The monolayer structure is now characterized by smaller domains (< 10 nm) similar or equal to the β-phase and some without an additional superstructure (marked by green lines in (c)).

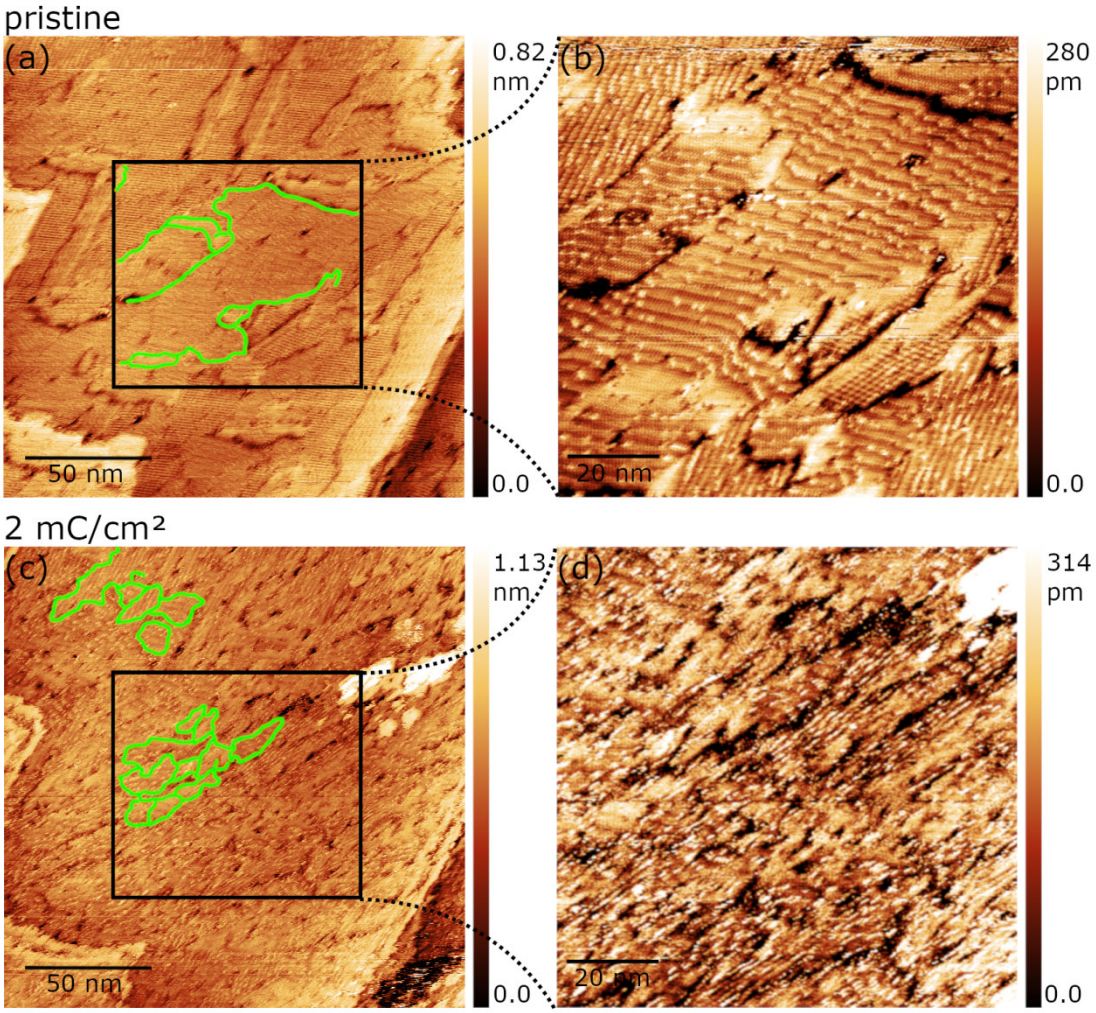

Figure 4.15: Reduction of the regular phase domain size upon 1 keV electron exposure with a dose of 2 mC/cm². The STM images were acquired at the same sample location before and after electron exposure. The SAM was prepared from DMF-based solution. (a),(b) Pristine SAM surface with regular phase domains being 10-100 nm in size. Some domain boundaries are marked in green. Tunneling parameter: (U=+450 mV, I=30pA). (c),(d) Irradiated monolayer surface, characterized by smaller phase domains (< 10 nm). Some domain boundaries are marked in green. Tunneling parameter: (U=-1.2 V, I=30pA). The images are not cross-talk corrected.

4.3.2.2 Formation of Sub-Nanometer-Sized Voids

Carbon Nanomembranes from TPT precursor molecules have shown a high performance for selective water permeation, according to Yang *et al.*[9], whereby the presence of intrinsic sub-nanometer-sized channels within the fully cross-linked TPT monolayer could be the cause. Cross-linking was performed with 50 eV electrons and a dose of 50 mC/cm². The water

molecules can pass through these pores, whereas other substances are efficiently blocked. The size and area density of the pores were estimated based on AFM measurements[9], yielding an estimated pore diameter of 0.7 ± 0.1 nm and an areal pore density of 0.7×10^{18} m^{-2}.

Sub-nanometer-sized voids, which could be a preliminary stage for pores, were found in this work for partially cross-linked TPT monolayers. Figure 4.16 (a) shows an irradiated monolayer surface (50 eV, 10 mC/cm²). One void is framed by a black, dashed circle. The voids may be surrounded by less ordered molecular constituents/ moieties. The molecular layer itself is still characterized by a certain residual order in the form of small regular domains, typically less than 10 nm in size (see Figure 4.14 (c)). The measured depth of the voids is ~0.1 nm (see Figure 4.16 (b)). It should be noted that the true depth of the voids cannot be measured accurately due to the finite sharpness of the STM tip. The presence of voids can probably be explained by a local variation in the areal molecular density caused by irradiation-induced local contractions of the monolayer as a result of cross-linking.

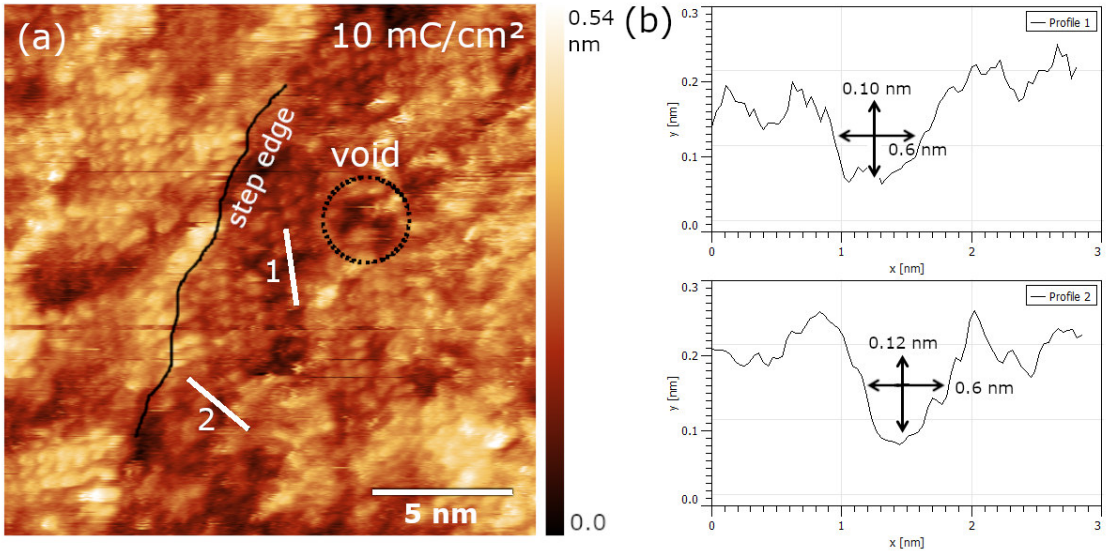

Figure 4.16: Formation of sub-nanometer-sized voids within the partially irradiated TPT monolayer (50 eV, 10 mC/cm²). The SAM was prepared from DMF-based solution. (a) High-magnification STM scan of the monolayer surface (U=-1.2 V and I=10 pA). (b) Height profiles across the voids. The measured depth is ~0.1 nm. The image is not cross-talk corrected.

The presence of nanovoids is more pronounced after increasing the irradiation dose to 25 mC/cm². Figure 4.17 (a) shows the STM image previously presented in Figure 4.14 (b), post-processed by using the *continuous wavelet transform*-function of gwyddion v.2.41 (scale: 2 pixels, wavelet type: Gaussian). This was to improve the visibility of the voids and to facilitate the marking of the voids by drawing the mask displayed in Figure 4.17 (b). The mask allows the determination of the lateral distribution and the size distribution of the voids. The lateral

distribution was approximated by a Poisson-distribution (see Figure 4.17 (c), red dashed line). The data was evaluated by dividing the surface area into equal segments (see inset) and counting the number of voids in each segment. However, it should be borne in mind that the limited size of the STM image may not provide representative data of the entire monolayer surface and therefore may not be of sufficient statistical significance. The observed deviation from the fit may therefore be a consequence of lack of statistical significance or may be due to structural influences of the monolayer, i.e. non-uniform cross-linking of the monolayer. Since the irradiation dose has been set to only 50% of the dose required to convert the monolayer into a fully cross-linked film, some fairly pristine molecular structures may still be present. This hypothesis is supported by the observation that the voids are more likely located in the darker regions (black arrows) of the image, while no voids are visible in the brighter regions (white arrows). This is consistent with the previous observation (see Figure 4.14 (c)) that monolayer areas with a certain residual molecular order appear brighter in STM images compared to cross-linked areas. This suggests that the local areal void density correlates with the monolayer molecular structure and that the void formation is directly attributed to cross-linking. The distribution of the equivalent void diameter was approximated by a Gaussian distribution, yielding a void diameter of 0.5 ± 0.2 nm. The consistency between the void diameter estimated here and the nanopore diameter of 0.7 ± 0.1 nm determined by Yang *et al.* using AFM[9] suggests that the voids could be ascribed to pores. The mean depth of the voids displayed in Figure 4.17 was derived from the applied mask and is 0.21 ± 0.02 nm. The areal density of the voids is $\sim 1.7 \cdot 10^{17}$ m^{-2}. This value is approximately four times lower than the areal pore density estimated in ref [9], which may be due to the higher irradiation dose used in ref [9] and/or the fact that not all existing voids were covered by the mask shown in Figure 4.17 (b). Unfortunately, the frequent occurence of imaging tip artifacts for highly-irradiated samples (see section 4.3.3) prevented the acquisition of molecularly-resolved STM images of fully cross-linked TPT monolayers (50 mC/cm²). It must be considered that the molecular packing density may also influence the areal void density. As discussed in section 4.2.1, the pristine SAM prepared from DMF-based solution is characterized by the presence of two major molecular phase domains, i.e. α- and β-phase domains. The molecular area in the α-phase is 0.216 nm² and in the β-phase is 0.288 nm². It is not known whether the cross-linked film shown in Figure 4.17 (a) has evolved from an α- or β-phase domain or from both. Molecular phase domains with sizes between 10 and 100 nm were observed in the pristine

SAM (see section 4.2.1), whereas the size of the STM image shown in Figure 4.17 (a) is only 50 nm.

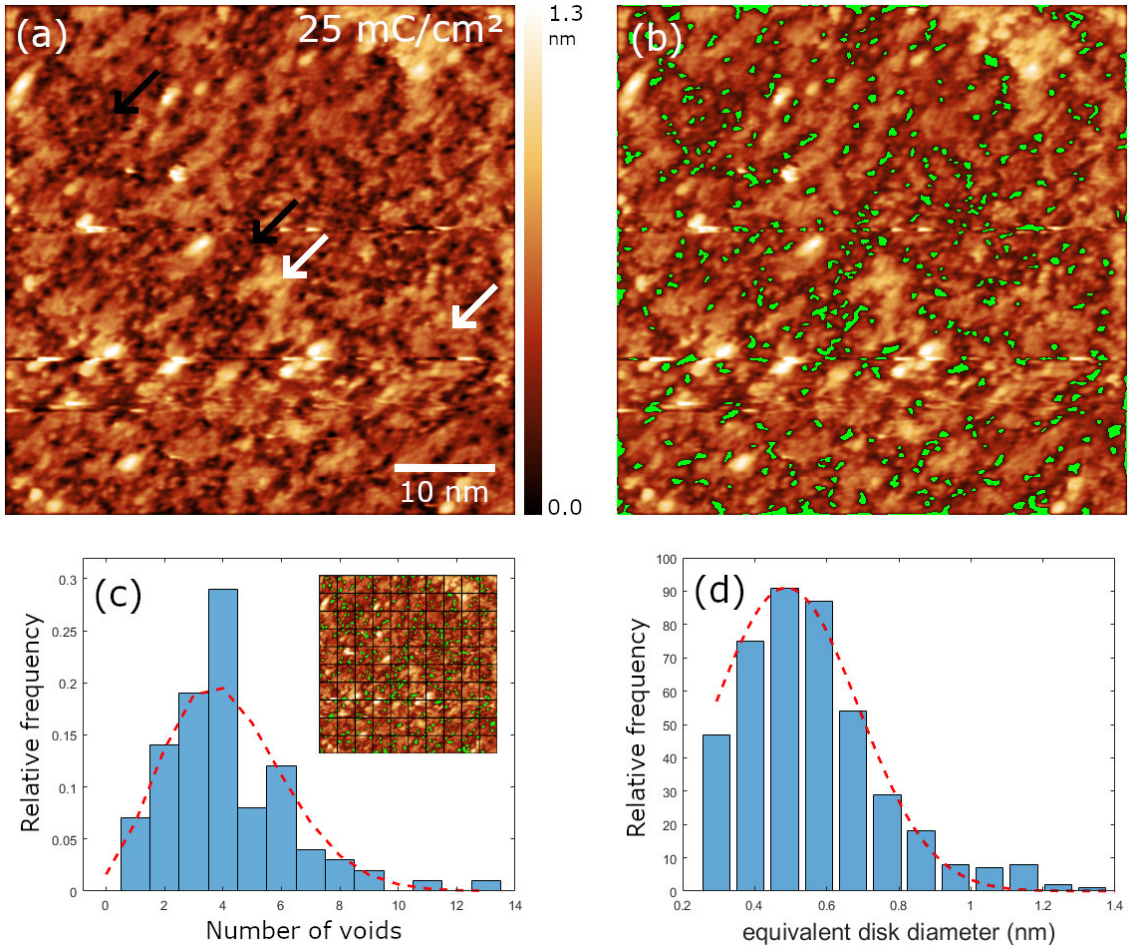

Figure 4.17: Formation of sub-nanometer-sized voids within the partially irradiated TPT monolayer. The SAM was prepared from solution. The irradiation was performed with 50 eV electrons and an irradiation dose of 25 mC/cm². (a) STM scan of the monolayer surface (U=-1.2 V, I=10 pA). The image is also shown in Figure **4.14** (d). The image was post-processed by using the *2D CWT*-function of gwyddion 2.41 (see text for details). Voids are preferentially located in darker regions (black arrow), whereas brighter regions (white arrow) are rather free of voids. (b) The same image as shown in (a). The voids were marked by using the *Mark by Segmentation*-function of gwyddion. (c) Lateral distribution of the voids. The fit displayed in red approximates the data by following a Poisson-distribution with parameter $\lambda = 3.7$. The data was acquired by dividing the STM image shown in (b) into equal sections (inset) and counting the number of voids in each section. (d) Estimation of the void diameter by calculating the equivalent disk diameter, which is the diameter of circular voids of similar area. The fit displayed in red approximates the data by following a Gaussian distribution, revealing a void diameter of 0.5 ± 0.2 nm.

4.3.3 Tip Artifacts in Imaging of Partially Cross-linked Monolayers

When rough surfaces are imaged by STM or AFM, the images often contain three-dimensional tip artifacts that directly reflect the shape of the tip[125]. The artifacts appear as a set of protrusions identical in size, shape and orientation and may therefore lead to incorrect image

interpretations. They may be caused by the presence of sharp features protruding out of the sample surface and rastering the surface of the scanning probe tip. Whereas the acquisition of STM data of pristine TPT SAMs has never been subject to tip artifact imaging within the scope of this thesis, imaging of partially irradiated monolayer surfaces was typically accompanied by imaging of tip artifacts. Two different image sequences comprising consecutive up- and down-scans are shown in Figure 4.18. The monolayers were exposed to 50 eV electrons with doses of 0.1 mC/cm² (upper sequence) and 40 mC/cm² (lower sequence). The tip artifacts are highlighted by black, dashed circles. The tip artifact pattern did not change in consecutive up- and down-scans, indicating the presence of sharp features that remain unaltered during scanning. As a general tendency, higher irradiation doses were accompanied by a higher areal density of tip artifacts. Imaging of partially cross-linked monolayers (> 10 mC/cm²) was often fully dominated by this effect. As imaging of pristine SAM surfaces has never been subject to tip artifact imaging, the appearance of tip artifacts may be traced back to electron irradiation-induced structural modifications of the monolayer, accompanied by molecular moieties protruding out of the monolayer surface. With increasing irradiation dose, TPT monolayers become rougher and more amorphous. As a result, the molecular structure of monolayers that had been irradiated with electron doses > 10 mC/cm² could only be resolved under exceptional circumstances that might be traced back to particularly sharp tip states.

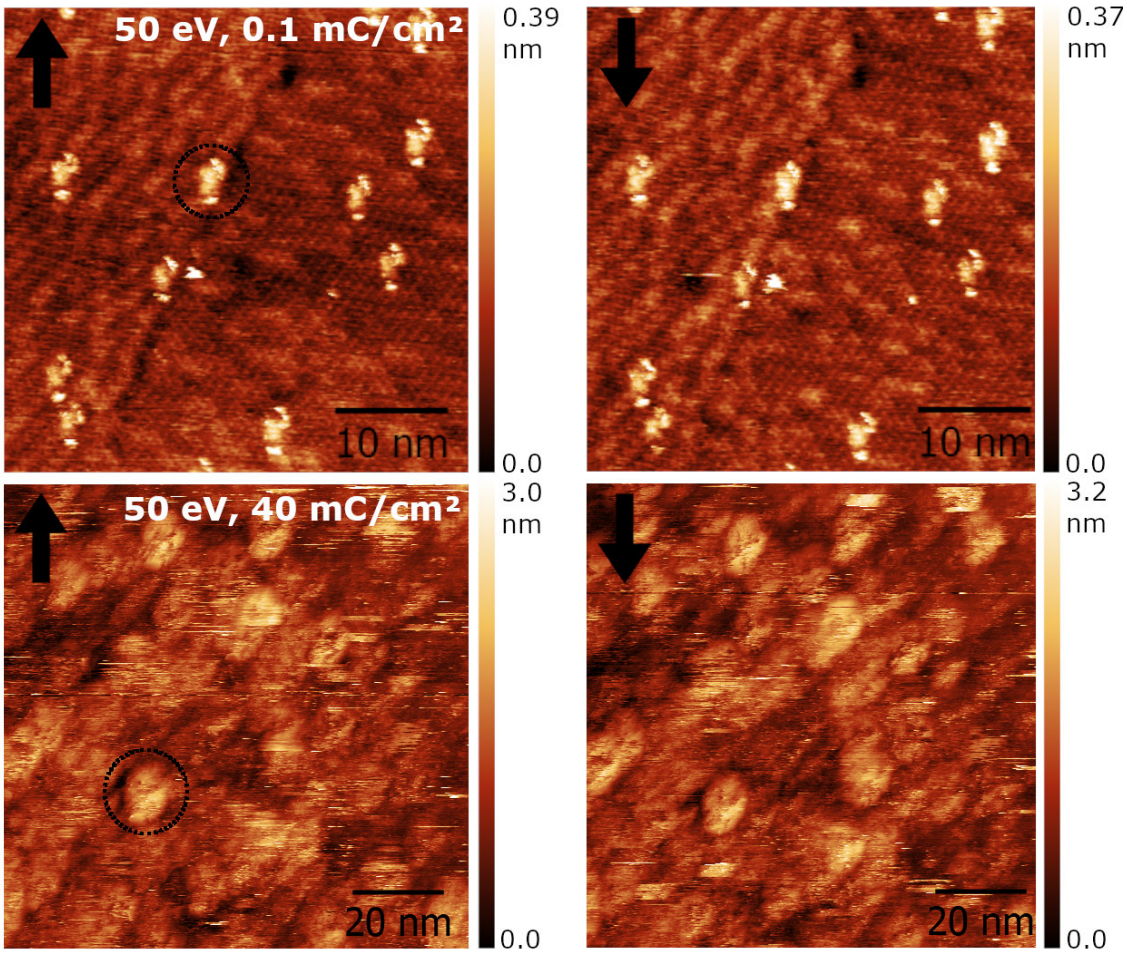

Figure 4.18: Imaging of tip artifacts on partially cross-linked monolayers. The artifact are highlighted by black, dashed circles. The artifact pattern remains unchanged in consecutive up and down scans (highlighted by black arrows). SAMs were irradiated with 50 eV electrons by applying a dose of 0.1 mC/cm² (upper image sequence, cross-talk corrected) and 40 mC/cm² (lower image sequence, not cross-talk corrected), respectively.

4.3.4 Summary

Electron-induced cross-linking of TPT SAMs on Au(111) on mica was studied by scanning tunneling microscopy. SAMs were grown either by immersing Au substrates into a solution of the TPT molecules diluted in DMF or from the gas phase under UHV conditions. SAMs were irradiated either by employing an in-situ electron floodgun emitting 50 eV electrons, an energy commonly used for cross-linking aromatic SAMs, or by employing the 1 keV rastering beam of a SEM, constituting the minimum energy of the electron column. The STM/SEM combination system may allow for acquiring STM images of the same sample location before and after the irradiation process, thus allowing for studying the effect of the electron impact on the local molecular scale by comparison of the respective images. However, due to the complexity of the experimental procedure, no extensive data sets were acquired. Cross-linking was investigated

by varying the irradiation dose. First of all, the initial stage of cross-linking was studied by irradiating the pristine SAM with a dose of 0.5 mC/cm², which corresponds to ~1 % of the total dose required to achieve a fully cross-linked monolayer. The evolution of the monolayer towards the nearly fully cross-linked state was studied by applying intermediate doses up to 25 mC/cm², which corresponds to ~50 % of the total dose for a fully cross-lined monolayer. Unfortunately, STM data of the fully cross-linked monolayer could not be obtained due to extensive tip artifact imaging.

At the initial stage of cross-linking, the irradiation with both 50 eV and 1 keV electrons leads to the presence of coherent, depressed spots (*dark spots*) that are randomly distributed over the whole surface and are apparently surrounded by the pristine monolayer. The size distribution of the dark spots decreases towards large areas, where spots with an average size of 5–6 molecular areas were identified and spots with sizes up to 33 molecular areas in the respective phases were also found. The measured depth of dark spots as a function of their area saturates at 1.4 ± 0.1 Å. Based on this observation and on the absence of gold adatom islands, a reconstruction of the underlying gold substrate into vacancy islands that could lead to the appearance of dark spots is thus excluded. STM data indicates that the internal structure of the dark spots appears to be of lower structural order compared to the pristine SAM, but the data does not provide further insights into their structure. It cannot be excluded that the dark spots in the STM images could also be caused by electron irradiation-induced desorption of molecular constituents or fragments and the consequential structural collapse of the surrounding molecules. However, the cross-section of TPT monomers derived from the XPS data for the PEs subject to cleavage of the respective S–Au bond indicates that the dark spots represent monolayer sections characterized by cleaved S–Au bonds. As the major contrast mechanism in the STM images is believed to be due to an enhanced tunneling barrier at the monolayer/substrate interface, the dark spots are ascribed to locally cross-linked islands within the pristine monolayer. As the spots include up to several tens of molecules, it is suggested that they may have evolved via radical chain reactions. The propagation of radical chain reactions within TPT monolayers upon 6 eV electron irradiation was previously proposed based on the observed aromaticity loss of 47-53 %[14]. Here, individual two-dimensional chain reactions are initiated by creation of one monomer radical each. Monomer radicalization proceeds via electron attachment at 6 eV, followed by the subsequent formation of a carbon radical center. Chain reactions are accompanied by a partial loss of aromaticity due to partial rehybridization

of the carbon centers from sp^2 to sp^3 and propagate via formation of covalent carbon-carbon bonds between rehybridized carbon centers on neighboring phenyl rings. The formation of locally cross-linked islands within the TPT monolayer surfaces irradiated with 50 eV and 1 keV PEs can therefore be caused by the 6 eV SEs emitted from the gold substrate. Indeed, the areal number density of the dark spots observed in the STM images of the 1 keV electron-irradiated monolayer surface is in good agreement with the expected areal number density of (secondary) EA events at 6.0 eV, which is derived from the reactive EA cross-section previously calculated by Amiaud *et al.* [14] divided by the factor n-1, where $n = 5–6$ is the average number of monomers involved in chain reactions which was derived from the STM data. However, it should be noted that the contribution of various electron-molecule primary interactions that generate radicals such as neutral dissociation or dissociative ionization cannot be excluded. In particular, it was estimated by Houplin *et al.*[53] that electron impact ionization is the major mechanism leading to hydrogen loss upon 50 eV electron impact, whereas the contribution of impact electronic excitation and the contribution of the 6 eV secondary electrons to the chemical transformations associated with the hydrogen loss were estimated to be much weaker. Following the proposed mechanisms, however, the propagation of radical chain reactions occurs almost exclusively without hydrogen loss[14]. Therefore, electron attachment may still play an essential role in the initiation of radical chain polymerization reactions. However, there is still an inconsistency in spectroscopic data that needs to be clarified: While 6 eV electron irradiation leads to the observed aromaticity loss, no noticeable rehybridization of the carbon centers was observed after irradiation with 50 eV electrons[53]. It is expected, though, that the 6 eV SEs emitted from the Au substrate upon 50 eV electron exposure have the same influence on the monolayer as 6 eV PEs. However, STM data at the initial stage of cross-linking indicates that the exposure to 50 eV and 1 keV electrons leads to the initiation and propagation of radical chain reactions. Potential mechanisms that could lead to the termination of the chain reactions were not discussed by Amiaud *et al.*[14]. Nevertheless, a termination either due to steric hindrance of the frontal monomer radical or due to contraction of the cross-linked molecular island is conceivable. In the further course of the irradiation process (50 eV, 10 mC/cm²), the long-range order is significantly reduced compared to the pristine SAM. The molecular structure is characterized by small domains of well-ordered molecules, with domain sizes typically less than 10 nm, whereas the pristine TPT SAM is typically characterized by phase domains sizes up to ~ 100 nm. The domains with regular

molecular ordering are separated by apparently cross-linked, amorphous parts of the monolayer. The electron-induced reduction of the average phase domain size is supported by STM data obtained in STM/SEM experiments (1 keV, 2 mC/cm²), which provides STM data of the same sample site immediately before and after the irradiation step.

The STM data for the nearly completely cross-linked monolayer (50 eV, 25 mC/cm²) allow the identification of sub-nanometer-sized voids, which can be assigned to *sub-nanochannels* or *pores* found and characterized by Yang *et al.*[9]. The lateral distribution of the voids can be approximated by a Poisson-distribution, indicating their random character. However, the lateral distribution may still be influenced by the initial SAM structure, since different structural phases with different molecular area densities are present (see section 4.2). This cannot be excluded due to the limited size of the respective STM image. The diameter of the voids was estimated to 0.5 ± 0.2 nm, which is consistent with the pore diameter estimated by Yang *et al.*[9]. The areal density of the voids amounts to ~$1.7 \cdot 10^{17}$ m^{-2}, which is roughly a factor of 4 lower than the areal pore density determined by Yang *et al.* However, it must be taken into account that the electron dose used by Yang *et al.* is 50 mC/cm² and thus higher by a factor of 2. Unfortunately, no STM data are available for 50 mC/cm² due to the extensive occurrence of tip artifact imaging. A further increase of the irradiation dose can still lead to an increasing area density of the voids. The comparison of the size distribution and the areal density of the voids observed by STM with the corresponding values for the pores determined by Yang *et al.* leads to the conclusion that the voids shown in Figure 4.17 (a) can probably be assigned to sub-nanometer pores within the cross-linked TPT layer, which will later on provide the already proven high filtration performance of TPT CNMs[9].

The essential stages of the electron irradiation-induced cross-linking of TPT on Au(111), as indicated by STM data obtained in this work, are visualized schematically in Figure 4.19. At the initial stage of cross-linking (a), individual radical chain reactions occur within the monolayer, which lead to the formation of (partially) cross-linked islands. At intermediate electron doses (b), the long-range order is significantly reduced compared to the pristine SAM, which leads to the existence of small domains of regular structural order that are separated by apparently cross-linked, amorphous parts of the monolayer. The progressive stage of cross-linking (c) is characterized by the absence of nearly any molecular ordering. The STM data allow the identification of sub-nanometer-sized voids that are apparently randomly distributed in the monolayer matrix and can be assigned to sub-nanochannels or pores.

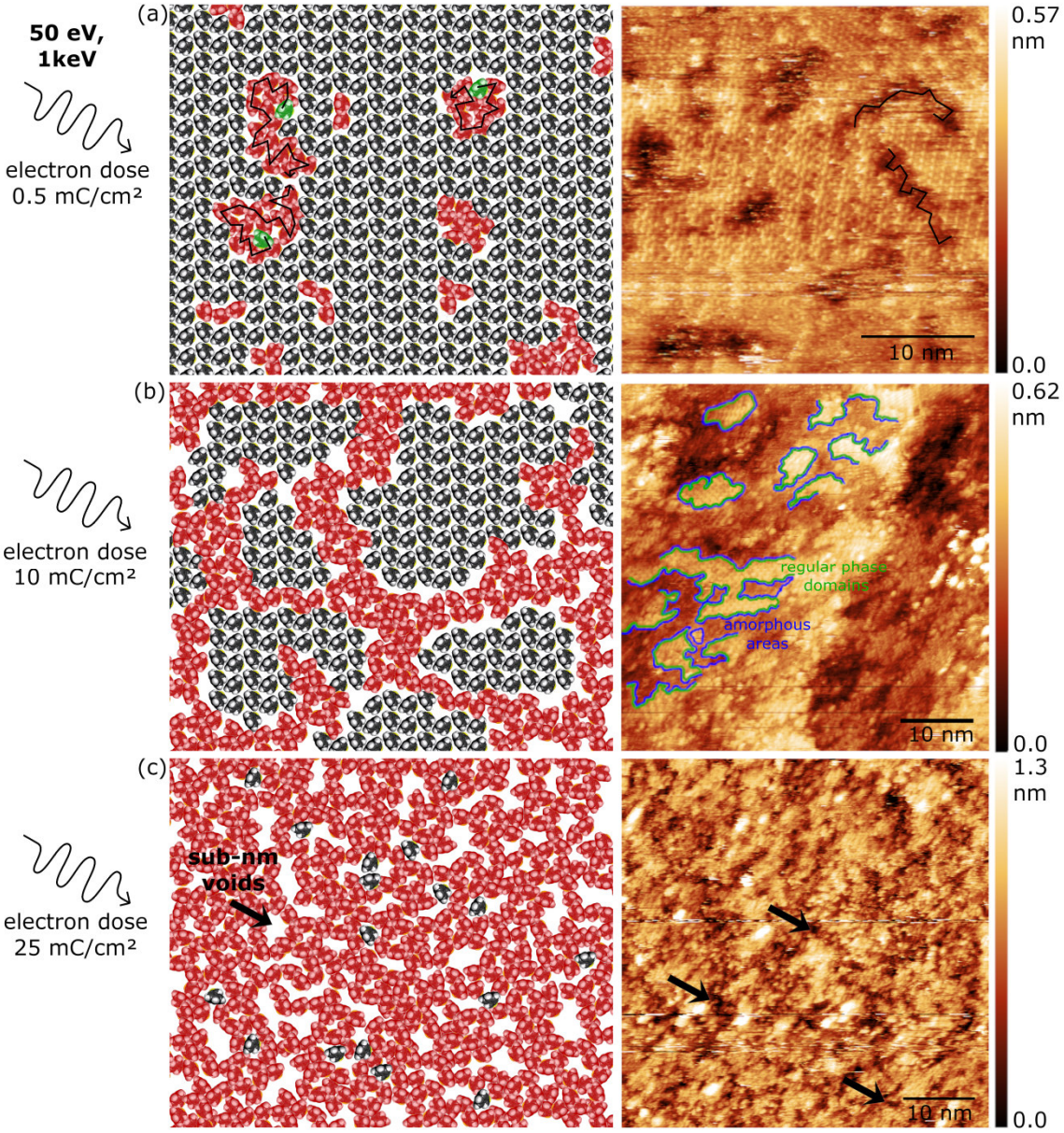

Figure 4.19: Schematic visualization of 50 eV/1 keV electron irradiation-induced cross-linking of *p*-terphenylthiol SAMs on Au(111), as indicated by STM data. (a) Electron impact at the initial stage of cross-linking (0.5 mC/cm²) creates radicalized molecular monomers (green) that initiate radical chain reactions, leading to the formation of cross-linked molecular "islands", accompanied by the cleavage of S–Au bonds (red). Potential reaction pathways are indicated by black arrows. (b) Intermediate doses lead to a reduction of the average domain size (~10 nm), separated by cross-linked parts of the monolayer (red). (c) An electron dose of 25 mC/cm² transforms the SAM into an amorphous molecular network of potentially porous structure. The presence of pristine monomers in the cross-linked layer cannot be excluded. Unfortunately, no STM data are available for 50 mC/cm², which is the dose required to convert the monolayer into a transferrable CNM.

5 Conclusion and Outlook

The electron irradiation-induced cross-linking of aromatic SAMs on Au(111) was studied by STM, employing TPT SAMs as model aromatic SAMs. So far, the electron irradiation-induced cross-linking of aromatic SAMs has been studied thoroughly by spectroscopic methods, yielding deep insight into structural and chemical transformations and the underlying mechanisms of cross-linking. However, microscopic data of cross-linked SAMs with molecular resolution is available only rarely, in particular when considering the initial stage and intermediate stages of cross-linking. The STM data acquired within the scope of this thesis provides information about cross-linking for the first time on the molecular scale, thus enabling to observe the influence of the electrons on the SAM on the local, molecular level. Cross-linking was investigated by delivering low, intermediate, and high 50 eV and 1 keV electron doses to the TPT monolayer, followed by the acquisition of STM data.

The molecular structures of the pristine TPT SAMs, prepared either from DMF-based solution or from the gas phase under UHV conditions were studied by high-resolution STM. The preparation from DMF-based solution is the common method for the preparation of carbon nanomembranes from TPT SAMs[9],[1]. SAMs prepared from the gas phase, however, are characterized by a similar molecular arrangement and have shown to be more suitable for STM experiments due to their outstanding crystalline purity. It is therefore expected that TPT SAMs prepared from the gas phase constitute a representative system of TPT SAMs prepared from DMF-based solution. STM data allows for the identification of two distinct, ordered phases for SAMs prepared from DMF-based solution; α-phase and β-phase domains. Both phases occupy approximately ~50% of the surface area. SAMs prepared from the gas phase are characterized by the absence of α-phase domains, that is, only β-phase domains and slightly distorted β-phase domains were observed. The packing density of the molecules in the α-phase is ~ 33% higher compared to the β-phase. Typical domains sizes for SAMs prepared either from DMF-based solution or from the gas phase are 10-100 nm.

STM data of the irradiated monolayer surface at the initial stage of cross-linking (50 eV and 1 keV, 0.5 mC/cm^2) reveals the presence of dark spots which may represent locally cross-linked sections of the monolayer. The STM contrast may originate from the local decoupling of

the molecules through the cleavage of S–Au bonds, as can be gathered from the cross-section for the S–Au bonds to be cleaved by an impinging electron deduced from XPS data. Based on the acquired STM data it is proposed that cross-linking in TPT SAMs (and possibly in aromatic SAMs in general) proceeds via radical chain reactions as previously proposed[14]. Following the size distribution of the dark spots, the chain reactions involve up to 33 molecules and 5–6 monomers on average. The first radicals initiating individual chain reactions may form upon 6 eV (secondary) EA, indicated by the reactive 6 eV electron attachment cross-section estimated previously based on HREELS data[14]. However, different electron-molecule primary interactions producing radicals cannot be excluded. Potential termination mechanisms cannot be deduced from the STM data but different mechanisms were proposed.

With reference to the aforementioned cross-sections derived from spectroscopic data, the dark spots were ascribed to locally cross-linked sections of the monolayer. However, surveying the internal structure and chemical nature of the dark spots is still an outstanding task. This may support the hypothesis that the dark spots can be ascribed to cross-linking via radical chain reactions. For this, *inelastic electron tunneling spectroscopy* (IETS) at low temperature may verify the partial sp^3-rehybridization of the carbon centers inside the dark spots. IN previous studies, two different conformations of the acetylene molecule (sp^2-like and sp^3-like) were found to exist on a Ni(110) surface[127]. A change of the LDOS of the dark spots compared to the pristine SAM areas may be detected by *I*-*V*-spectroscopy. The modification of the local work function by the dark spots may be quantified by ln(*I*)-*z*-spectroscopy[68] or by performing spatially resolved tunneling barrier height measurements[128]. Resolving the topographical structure of the dark spots by AFM may reveal whether or not the internal structure is subject to amorphization.

The propagation of radical chain reactions at the initial cross-linking stage may be investigated by preparing TPT SAMs including spin traps at low concentration compared to the TPT monomers. The isolated spin traps should be easily distinguishable from the surrounding TPT monolayer due to their expected difference in STM contrast. The irradiated TPT/spin trap-surface may be characterized by the presence of dark spots tendentially being smaller compared to the spots in the pure TPT monolayer as the propagation of the chain reactions is expected to be terminated in the presence of spin trapping molecules. It is conceivable to employ aromatic thiol-containing molecules similar to TPT molecules but including spin traps such as n-tert-butyl-alpha-phenylnitrone or 5,5-dimethyl-1-pyrroline *N*-oxide.

To explore which electron-molecule primary interactions cause the initiation of radical chain reactions and thus contribute to the creation of cross-linked islands within the monolayer, the irradiation experiments should be performed with 6 eV primary electrons, corresponding to the energy of the DEA resonance. Below ionization and excitation thresholds, the production of monomer radicals can only proceed upon electron attachment, thus excluding different interaction mechanisms. Provided that equivalent electron doses were delivered to the monolayer (the 6 eV primary electron dose should be similar to the estimated 6 eV secondary electron dose the monolayer was exposed to in the 1 keV irradiation experiments for this thesis), the areal number density and possibly the size distribution of the dark spots may give insight into the role of electron attachment for cross-linking.

Provided that cross-linking indeed proceeds via radical chain reactions, the dependency of the average number of molecules involved in individual chain reactions on the areal molecular density may be of interest. It would be conceivable that higher packing densities facilitate the propagation of chain reactions. The average size of the dark spots in α-phase domains (packing density ~33% higher compared to β-phase domains) may differ significantly from the respective value in β-phase domains. Irradiation experiments of biphenyltiolate and/or quaterphenylthiolate-based SAMs may give additional insight.

In the further course of the irradiation process (50 eV, 10 mC/cm²), the long-range order is reduced significantly compared to the pristine SAM. Pristine like domains are typically less than 10 nm in size, being separated by apparently cross-linked, amorphous parts of the monolayer. The reduction of the average regular phase domain size is supported by STM data acquired within the scope of complementary STM/SEM experiments (1 keV, 2 mC/cm²). The evolution towards the nearly fully cross-linked state (50 eV, 25 mC/cm²) is characterized by a loss of long- and short-range molecular order. Sub-nanometer-sized voids that can be assigned to *sub-nanochannels* or *pores* found and characterized by Yang *et al.*[9] were observed. Here again, the dependency of the equivalent pore diameter on both the molecular packing density and the molecular length may be of interest.

The STM experiments were significantly impaired by unstable measurement conditions, in particular experiments on partially irradiated samples (electron dose > 1 mC/cm²). Recurrent tip modifications during the scan and tip artifact imaging resulted in quite a limited data set.

Sample cooling and SAM preparation under UHV conditions from the gas phase may help to increase the stability of the measurements.

List of Figures

References

[1] P. Angelova, A. Gölzhäuser, Carbon Nanomembranes. Physical Sciences Reviews. 2 (2017).

[2] A. Turchanin, A. Gölzhäuser, Carbon nanomembranes from self-assembled monolayers: Functional surfaces without bulk. Progress in Surface Science. 87, 108–162 (2012).

[3] A. Turchanin, A. Beyer, C. T. Nottbohm, X. Zhang, R. Stosch, A. Sologubenko, J. Mayer, P. Hinze, T. Weimann, A. Gölzhäuser, One Nanometer Thin Carbon Nanosheets with Tunable Conductivity and Stiffness. Advanced Materials. 21, 1233–1237 (2009).

[4] X. Zhang, C. Neumann, P. Angelova, A. Beyer, A. Gölzhäuser, Tailoring the Mechanics of Ultrathin Carbon Nanomembranes by Molecular Design. Langmuir. 30, 8221–8227 (2014).

[5] X. Zhang, A. Beyer, A. Gölzhäuser, Mechanical characterization of carbon nanomembranes from self-assembled monolayers. Beilstein Journal of Nanotechnology. 2, 826–833 (2011).

[6] A. Turchanin, M. El-Desawy, A. Gölzhäuser, High thermal stability of cross-linked aromatic self-assembled monolayers: Nanopatterning via selective thermal desorption. Applied Physics Letters. 90, 53102 (2007).

[7] N. Meyerbröker, Z.-A. Li, W. Eck, M. Zharnikov, Biocompatible Nanomembranes Based on PEGylation of Cross-Linked Self-Assembled Monolayers. Chemistry of Materials. 24, 2965–2972 (2012).

[8] M. Ai, S. Shishatskiy, J. Wind, X. Zhang, C. T. Nottbohm, N. Mellech, A. Winter, H. Vieker, J. Qiu, K.-J. Dietz, A. Gölzhäuser, A. Beyer, Carbon Nanomembranes (CNMs) Supported by Polymer: Mechanics and Gas Permeation. Advanced Materials. 26, 3421–3426 (2014).

[9] Y. Yang, P. Dementyev, N. Biere, D. Emmrich, P. Stohmann, R. Korzetz, X. Zhang, A. Beyer, S. Koch, D. Anselmetti, A. Gölzhäuser, Rapid Water Permeation Through Carbon Nanomembranes with Sub-Nanometer Channels. ACS Nano. 12, 4695–4701 (2018).

[10] L. Wang, M. S. H. Boutilier, P. R. Kidambi, D. Jang, N. G. Hadjiconstantinou, R.

Karnik, Fundamental transport mechanisms, fabrication and potential applications of nanoporous atomically thin membranes. Nature Nanotechnology. 12, 509–522 (2017).

[11] P. Angelova, H. Vieker, N.-E. Weber, D. Matei, O. Reimer, I. Meier, S. Kurasch, J. Biskupek, D. Lorbach, K. Wunderlich, L. Chen, A. Terfort, M. Klapper, K. Müllen, U. Kaiser, A. Gölzhäuser, A. Turchanin, A Universal Scheme to Convert Aromatic Molecular Monolayers into Functional Carbon Nanomembranes. ACS Nano. 7, 6489–6497 (2013).

[12] D. Emmrich, A. Beyer, A. Nadzeyka, S. Bauerdick, J. C. Meyer, J. Kotakoski, A. Gölzhäuser, Nanopore fabrication and characterization by helium ion microscopy. Applied Physics Letters. 108, 163103 (2016).

[13] A. Turchanin, D. Käfer, M. El-Desawy, C. Wöll, G. Witte, A. Gölzhäuser, Molecular Mechanisms of Electron-Induced Cross-Linking in Aromatic SAMs. Langmuir. 25, 7342–7352 (2009).

[14] L. Amiaud, J. Houplin, M. Bourdier, V. Humblot, R. Azria, C.-M. Pradier, A. Lafosse, Low-energy electron induced resonant loss of aromaticity: consequences on cross-linking in terphenylthiol SAMs. Phys. Chem. Chem. Phys. 16, 1050–1059 (2014).

[15] C. Yildirim, M. Füser, A. Terfort, M. Zharnikov, Modification of Aromatic Self-Assembled Monolayers by Electron Irradiation: Basic Processes and Related Applications. The Journal of Physical Chemistry C. 121, 567–576 (2017).

[16] J. C. Love, L. A. Estroff, J. K. Kriebel, R. G. Nuzzo, G. M. Whitesides, Self-Assembled Monolayers of Thiolates on Metals as a Form of Nanotechnology. Chemical Reviews. 105, 1103–1170 (2005).

[17] C. Vericat, M. E. Vela, R. C. Salvarezza, Self-assembled monolayers of alkanethiols on Au(111): surface structures, defects and dynamics. Physical Chemistry Chemical Physics. 7, 3258 (2005).

[18] C. Vericat, M. E. Vela, G. Corthey, E. Pensa, E. Cortés, M. H. Fonticelli, F. Ibañez, G. E. Benitez, P. Carro, R. C. Salvarezza, Self-assembled monolayers of thiolates on metals: a review article on sulfur-metal chemistry and surface structures. RSC Adv. 4, 27730–27754 (2014).

[19] Y. Xue, X. Li, H. Li, W. Zhang, Quantifying thiol–gold interactions towards the efficient strength control. Nature Communications. 5 (2014).

[20] C. Vericat, M. E. Vela, G. Benitez, P. Carro, R. C. Salvarezza, Self-assembled monolayers of thiols and dithiols on gold: new challenges for a well-known system. Chemical Society Reviews. 39, 1805-1834 (2010).

[21] E. Verwüster, E. Wruss, E. Zojer, O. T. Hofmann, Exploring the driving forces behind the structural assembly of biphenylthiolates on Au(111). The Journal of Chemical Physics. 147, 24706 (2017).

[22] L. F. Peiretti, P. Quaino, F. Tielens, Competition between Two High-Density Assemblies of Poly(phenyl)thiols on Au(111). The Journal of Physical Chemistry C. 120, 25462–25472 (2016).

[23] D. Samanta, A. Sarkar, Immobilization of bio-macromolecules on self-assembled monolayers: methods and sensor applications. Chemical Society Reviews. 40, 2567 (2011).

[24] B. Bhushan, Nanotribology and Nanomechanics. Springer. (2017).

[25] S. Casalini, C. A. Bortolotti, F. Leonardi, F. Biscarini, Self-assembled monolayers in organic electronics. Chemical Society Reviews. 46, 40–71 (2017).

[26] T. Schmaltz, G. Sforazzini, T. Reichert, H. Frauenrath, Self-Assembled Monolayers as Patterning Tool for Organic Electronic Devices. Advanced Materials. 29, 1605286 (2017).

[27] J.-P. Hong, A.-Y. Park, S. Lee, J. Kang, N. Shin, D. Y. Yoon, Tuning of Ag work functions by self-assembled monolayers of aromatic thiols for an efficient hole injection for solution processed triisopropylsilylethynyl pentacene organic thin film transistors. Applied Physics Letters. 92, 143311 (2008).

[28] I. Langmuir, VAPOR PRESSURES, EVAPORATION, CONDENSATION AND ADSORPTION. Journal of the American Chemical Society. 54, 2798–2832 (1932).

[29] H. J. Butt, K. Graf, M. Kappl, Physics and Chemistry of Interfaces. Wiley. (2013).

[30] G. E. Poirier, E. D. Pylant, The Self-Assembly Mechanism of Alkanethiols on Au(111). Science. 272, 1145–1148 (1996).

[31] H. Kampmann, Über das Wachstum und die Struktur Selbstorganisierender Monolagen. Universitätsbibliothek Bielefeld, Bielefeld (2014).

[32] G. E. Poirier, Coverage-Dependent Phases and Phase Stability of Decanethiol on Au(111). Langmuir. 15, 1167–1175 (1999).

[33] D. K. Schwartz, MECHANISMS AND KINETICS OFSELF-ASSEMBLED

MONOLAYER FORMATION. Annual Review of Physical Chemistry. 52, 107–137 (2001).

[34] T. Ishida, W. Mizutani, H. Azehara, F. Sato, N. Choi, U. Akiba, M. Fujihira, H. Tokumoto, Adsorption Processes of Self-Assembled Monolayers Made from Terphenyl Thiols. Langmuir. 17, 7459–7463 (2001).

[35] F. Schreiber, Structure and growth of self-assembling monolayers. Progress in Surface Science. 65, 151–257 (2000).

[36] Y. Arima, H. Iwata, Effect of wettability and surface functional groups on protein adsorption and cell adhesion using well-defined mixed self-assembled monolayers. Biomaterials. 28, 3074–3082 (2007).

[37] M. Yu, H. Ascolani, G. Zampieri, D. P. Woodruff, C. J. Satterley, Robert G. Jones, V. R. Dhanak, The Structure of Atomic Sulfur Phases on Au(111). J. Phys. Chem. B. 111, 10904-10914 (2007).

[38] G. E. Poirier, M. J. Tarlov, The c(4X2) Superlattice of n-Alkanethiol Monolayers Self-Assembled on Au(111). Langmuir. 10, 2853–2856 (1994).

[39] A. Bashir, W. Azzam, M. Rohwerder, A. Terfort, Polymorphism in Self-Assembled Terphenylthiolate Monolayers on Au(111). Langmuir. 29, 13449–13456 (2013).

[40] W. Azzam, A. Bashir, M. Ebqa'ai, H. Almalki, N. Al-Refaie, Unexpected Formation of Dense Phases along with Temperature-Induced, Self-Assembled Terphenylthiolate Monolayers on Au(111). The Journal of Physical Chemistry C. 120, 17308–17322 (2016).

[41] C. Fuxen, W. Azzam, R. Arnold, G. Witte, A. Terfort, C. Wöll, Structural Characterization of Organothiolate Adlayers on Gold: The Case of Rigid, Aromatic Backbones. Langmuir. 17, 3689–3695 (2001).

[42] D. G. Matei, H. Muzik, A. Gölzhäuser, A. Turchanin, Structural Investigation of 1,1′-Biphenyl-4-thiol Self-Assembled Monolayers on Au(111) by Scanning Tunneling Microscopy and Low-Energy Electron Diffraction. Langmuir. 28, 13905–13911 (2012).

[43] S. Frey, V. Stadler, K. Heister, W. Eck, M. Zharnikov, M. Grunze, B. Zeysing, A. Terfort, Structure of Thioaromatic Self-Assembled Monolayers on Gold and Silver. Langmuir. 17, 2408–2415 (2001).

[44] P. J. Cumpson, The Thickogram: a method for easy film thickness measurement in

XPS. Surface and Interface Analysis. 29, 403–406 (2000).

[45] M. J. Lercel, H. G. Craighead, A. N. Parikh, K. Seshadri, D. L. Allara, Sub-10 nm lithography with self-assembled monolayers. Applied Physics Letters. 68, 1504–1506 (1996).

[46] N. Ballav, S. Schilp, M. Zharnikov, Electron-Beam Chemical Lithography with Aliphatic Self-Assembled Monolayers. Angewandte Chemie International Edition. 47, 1421–1424 (2008).

[47] W. Eck, A. Küller, M. Grunze, B. Völkel, A. Gölzhäuser, Freestanding Nanosheets from Crosslinked Biphenyl Self-Assembled Monolayers. Advanced Materials. 17, 2583–2587 (2005).

[48] W. Geyer, V. Stadler, W. Eck, M. Zharnikov, A. Gölzhäuser, M. Grunze, Electron-induced crosslinking of aromatic self-assembled monolayers: Negative resists for nanolithography. Applied Physics Letters. 75, 2401–2403 (1999).

[49] P. A. Waske, N. Meyerbröker, W. Eck, M. Zharnikov, Self-Assembled Monolayers of Cyclic Aliphatic Thiols and Their Reaction toward Electron Irradiation. The Journal of Physical Chemistry C. 116, 13559–13568 (2012).

[50] N. Meyerbroeker, P. Waske, M. Zharnikov, Amino-terminated biphenylthiol self-assembled monolayers as highly reactive molecular templates. The Journal of Chemical Physics. 142, 101919 (2015).

[51] X. Zhang, H. Vieker, A. Beyer, A. Gölzhäuser, Fabrication of carbon nanomembranes by helium ion beam lithography. Beilstein Journal of Nanotechnology. 5, 188–194 (2014).

[52] A. Turchanin, M. Schnietz, M. El-Desawy, H. H. Solak, C. David, A. Gölzhäuser, Fabrication of Molecular Nanotemplates in Self-Assembled Monolayers by Extreme-Ultraviolet-Induced Chemical Lithography. Small. 3, 2114–2119 (2007).

[53] J. Houplin, C. Dablemont, L. Sala, A. Lafosse, L. Amiaud, Electron Processing at 50 eV of Terphenylthiol Self-Assembled Monolayers: Contributions of Primary and Secondary Electrons. Langmuir. 31, 13528–13534 (2015).

[54] W. Eck, V. Stadler, W. Geyer, M. Zharnikov, A. Gölzhäuser, M. Grunze, Generation of Surface Amino Groups on Aromatic Self-Assembled Monolayers by Low Energy Electron Beams—A First Step Towards Chemical Lithography. Advanced Materials. 12, 805–808 (2000).

[55] S. Koch, C. D. Kaiser, P. Penner, M. Barclay, L. Frommeyer, D. Emmrich, P. Stohmann, T. Abu-Husein, A. Terfort, D. H. Fairbrother, O. Ingólfsson, A. Gölzhäuser, Amplified cross-linking efficiency of self-assembled monolayers through targeted dissociative electron attachment for the production of carbon nanomembranes. Beilstein Journal of Nanotechnology. 8, 2562–2571 (2017).

[56] Y. Tai, A. Shaporenko, W. Eck, M. Grunze, M. Zharnikov, Depth Distribution of Irradiation-Induced Cross-Linking in Aromatic Self-Assembled Monolayers. Langmuir. 20, 7166–7170 (2004).

[57] K. Takahiro, A. Terai, S. Oizumi, K. Kawatsura, S. Yamamoto, H. Naramoto, Amorphization of carbon materials studied by X-ray photoelectron spectroscopy. Nuclear Instruments and Methods in Physics Research Section B: Beam Interactions with Materials and Atoms. 242, 445–447 (2006).

[58] D. G. Matei, N.-E. Weber, S. Kurasch, S. Wundrack, M. Woszczyna, M. Grothe, T. Weimann, F. Ahlers, R. Stosch, U. Kaiser, A. Turchanin, Functional Single-Layer Graphene Sheets from Aromatic Monolayers. Advanced Materials. 25, 4146–4151 (2013).

[59] M. Zharnikov, A. Shaporenko, A. Paul, A. Gölzhäuser, A. Scholl, X-ray Absorption Spectromicroscopy Studies for the Development of Lithography with a Monomolecular Resist. The Journal of Physical Chemistry B. 109, 5168–5174 (2005).

[60] N. Meyerbröker, M. Zharnikov, Modification of Nitrile-Terminated Biphenylthiol Self-Assembled Monolayers by Electron Irradiation and Related Applications. Langmuir. 28, 9583–9592 (2012).

[61] P. Cabrera-Sanfelix, A. Arnau, D. Sánchez-Portal, First-principles investigation of electron-induced cross-linking of aromatic self-assembled monolayers on Au(111). Physical Chemistry Chemical Physics. 12, 1578 (2010).

[62] G. Binnig, H. Rohrer, C. Gerber, E. Weibel, 7 × 7 Reconstruction on Si(111) Resolved in Real Space. Physical Review Letters. 50, 120–123 (1983).

[63] G. Binnig, H. Rohrer, C. Gerber, E. Weibel, Tunneling through a controllable vacuum gap. Applied Physics Letters. 40, 178–180 (1982).

[64] M. F. Crommie, C. P. Lutz, D. M. Eigler, E. J. Heller, Quantum corrals. Physica D: Nonlinear Phenomena. 83, 98–108 (1995).

[65] Wikipedia contributors. (2019, September 10). Scanning tunneling microscope.

In Wikipedia, The Free Encyclopedia. Retrieved 11:18, September 18, 2019, from https://en.wikipedia.org/w/index.php?title=Scanning_tunneling_microscope&oldid=915051607

[66] L. De Broglie, Waves and Quanta. Nature. 112, 540–540 (1923).

[67] E. Schrödinger, Quantisierung als Eigenwertproblem. Ann. Phys. 385, 437–490 (1926).

[68] R. Wiesendanger, Scanning Probe Microscopy and Spectroscopy: Methods and Applications. Cambridge: Cambridge University Press. (1994).

[69] J. Bardeen, Tunnelling from a Many-Particle Point of View. Physical Review Letters. 6, 57–59 (1961).

[70] G. Wentzel, Eine Verallgemeinerung der Quantenbedingungen für die Zwecke der Wellenmechanik. Zeitschrift für Physik. 38, 518–529 (1926).

[71] H. A. Kramers, Wellenmechanik und halbzahlige Quantisierung. Zeitschrift für Physik. 39, 828–840 (1926).

[72] L Brillouin, La mécanique ondulatoire de Schrödinger; une méthode générale de resolution par approximations successive. Compt.Rend.Hebd.Seances Acad.Sci. 183, 1, 24-26 (1926).

[73] J. G. Simmons, Generalized Formula for the Electric Tunnel Effect between Similar Electrodes Separated by a Thin Insulating Film. Journal of Applied Physics. 34, 1793–1803 (1963).

[74] J. Tersoff, D. R. Hamann, Theory and Application for the Scanning Tunneling Microscope. Physical Review Letters. 50, 1998 (1983).

[75] J. Tersoff, D. R. Hamann, Theory of the Scanning Tunneling Microscope. Phys. Rev. B. 31, 805 (1985).

[76] C. J. Chen, Theory of scanning tunneling spectroscopy. Journal of Vacuum Science & Technology A: Vacuum, Surfaces, and Films. 6, 319–322 (1988).

[77] R. Wiesendanger, D. Buergler, G. Tarrach, D. Anselmetti, H. R. Hidber, H. -J. Güntherodt, An ultrahigh vacuum scanning tunneling microscope for the investigation of clean surfaces. Journal of Vacuum Science & Technology A: Vacuum, Surfaces, and Films. 8, 339–344 (1990).

[78] C. J. Chen, Origin of atomic resolution on metal surfaces in scanning tunneling microscopy. Physical Review Letters. 65, 448 (1990).

[79] C. J. Chen, Microscopic view of scanning tunneling microscopy. Journal of Vacuum Science & Technology A. 9, 44 (1991).

[80] C. J. Chen, Tunneling matrix elements in three-dimensional space: The derivative rule and the sum rule. Physical Review B. 42, 8841–8857 (1990).

[81] K. D. Sattler, Fundamentals of Picoscience. CRC Press. (2014).

[82] V. M. Hallmark, S. Chiang, J. F. Rabolt, J. D. Swalen, R. J. Wilson, Observation of Atomic Corrugation on Au(111) by Scanning Tunneling Microscopy. Physical Review Letters. 59, 2879–2882 (1987).

[83] A. N. Chaika, S. S. Nazin, V. N. Semenov, S. I. Bozhko, O. Lübben, S. A. Krasnikov, K. Radican and I. V. Shvets, Selecting the tip electron orbital for scanning tunneling microscopy imaging with sub-ångström lateral resolution. EPL (Europhysics Letters). 92, 46003 (2010).

[84] C. Grave, C. Risko, A. Shaporenko, Y. Wang, C. Nuckolls, M. A. Ratner, M. A. Rampi, M. Zharnikov, Charge Transport through Oligoarylene Self-assembled Monolayers: Interplay of Molecular Organization, Metal–Molecule Interactions, and Electronic Structure. Advanced Functional Materials. 17, 3816–3828 (2007).

[85] N. D. Lang, Apparent Size of an Atom in the Scanning Tunneling Microscope as a Function of Bias. Physical Review Letters. 58, 45 (1987).

[86] H. Ohtani, R. J. Wilson, S. Chiang, and C. M. Mate, Scanning Tunneling Microscopy Observations of Benzene Molecules on the Rh(111)-(3 × 3) (C6H6 + 2CO) Surface. Physical Review Letters. 60, 2398 (1988).

[87] P. Sautet, Images of Adsorbates with the Scanning Tunneling Microscope: Theoretical Approaches to the Contrast Mechanism. Chemical Reviews. 97, 1097–1116 (1997).

[88] P. Penner, X. Zhang, E. Marschewski, F. Behler, P. Angelova, A. Beyer, J. Christoffers, A. Gölzhäuser, Charge Transport through Carbon Nanomembranes. The Journal of Physical Chemistry C. 118, 21687–21694 (2014).

[89] C. Yildirim, E. Sauter, A. Terfort, M. Zharnikov, Effect of Electron Irradiation on Electric Transport Properties of Aromatic Self-Assembled Monolayers. The Journal of Physical Chemistry C. 121, 7355–7364 (2017).

[90] X. Zhang, E. Marschewski, P. Penner, A. Beyer, A. Gölzhäuser, Investigation of electronic transport through ultrathin carbon nanomembrane junctions by

conductive probe atomic force microscopy and eutectic Ga–In top contacts. Journal of Applied Physics. 122, 55103 (2017).

[91] B. de Boer, A. Hadipour, M. M. Mandoc, T. van Woudenbergh, P. W. M. Blom, Tuning of Metal Work Functions with Self-Assembled Monolayers. Advanced Materials. 17, 621–625 (2005).

[92] E. Sauter, C. Yildirim, A. Terfort, M. Zharnikov, Adjustment of the Work Function of Pyridine and Pyrimidine Substituted Aromatic Self-Assembled Monolayers by Electron Irradiation. The Journal of Physical Chemistry C. 121, 12834–12841 (2017).

[93] L. Kong, F. Chesneau, Z. Zhang, F. Staier, A. Terfort, P. A. Dowben, and M. Zharnikov, Electronic Structure of Aromatic Monomolecular Films: The Effect of Molecular Spacers and Interfacial Dipoles. The Journal of Physical Chemistry C. 115, 45, 22422-22428 (2011).

[94] J. Houplin, L. Amiaud, C. Dablemont, A. Lafosse, DOS and electron attachment effects in the electron-induced vibrational excitation of terphenylthiol SAMs. Physical Chemistry Chemical Physics. 17, 30721–30728 (2015).

[95] D.-Q. Feng, D. Wisbey, Y. B. Losovyj, Y. Tai, M. Zharnikov, P. A. Dowben, Electronic structure and polymerization of a self-assembled monolayer with multiple arene rings. Physical Review B. 74 (2006).

[96] A. Einstein, Über einen die Erzeugung und Verwandlung des Lichtes betreffenden heuristischen Gesichtspunkt. Ann. Phys. 322, 132–148 (1905).

[97] M. Planck, On the Law of Distribution of Energy in the Normal Spectrum. Ann. Phys. 4, 553-563 (1901).

[98] J. H. Scofield, Hartree-Slater subshell photoionization cross-sections at 1254 and 1487 eV. Journal of Electron Spectroscopy and Related Phenomena. 8, 129–137 (1976).

[99] M. P. Seah, W. A. Dench, Quantitative electron spectroscopy of surfaces: A standard data base for electron inelastic mean free paths in solids. Surface and Interface Analysis.
1, 2–11 (1979).

[100] D. Briggs, J. T. Grant, Surface Analysis by Auger and X-Ray Photoelectron Spectroscopy. SurfaceSpectra: Manchester, UK (2003).

[101] J. Houplin, L. Amiaud, T. Sedzik, C. Dablemont, D. Teillet-Billy, N. Rougeau, A. Lafosse, A combined DFT/HREELS study of the vibrational modes of terphenylthiol

SAMs. The European Physical Journal D. 69 (2015).

[102] K. Heister, M. Zharnikov, M. Grunze, L.S.O. Johansson, Adsorption of alkanethiols and biphenylthiols on Au and Ag substrates: a high-resolution X-ray photoelectron Spectroscopy study. J.Phys.Chem. B. 105, 4058-4061 (2001).

[103] P. Rahe, R. Bechstein, A. Kühnle, Vertical and lateral drift corrections of scanning probe microscopy images. Journal of Vacuum Science & Technology B. 28, C4E31 (2010).

[104] D. Necas, P. Klapetek, Gwyddion: An open-source software for SPM data analysis. Cent. Eur. J. Phys. 10(1), 181-188 (2012).

[105] J. M. Rodriguez-Fortun, J. Orus, J. Alfonso, F. Buil, J. A. Castellanos, Hysteresis in Piezoelectric Actuators: Modeling and Compensation. IFAC Proceedings Volumes. 44, 5237–5242 (2011).

[106] S. Frey, H.-T. Rong, K. Heister, Y.-J. Yang, M. Buck, M. Zharnikov, Response of Biphenyl-Substituted Alkanethiol Self-Assembled Monolayers to Electron Irradiation: Damage Suppression and Odd–Even Effects. Langmuir. 18, 3142–3150 (2002).

[107] M. Zharnikov, S. Frey, K. Heister, M. Grunze, Modification of Alkanethiolate Monolayers by Low Energy Electron Irradiation: Dependence on the Substrate Material and on the Length and Isotopic Composition of the Alkyl Chains. Langmuir. 16, 2697–2705 (2000).

[108] C. Olsen, P. A. Rowntree, Bond-selective dissociation of alkanethiol based self-assembled monolayers adsorbed on gold substrates, using low-energy electron beams. The Journal of Chemical Physics. 108, 3750–3764 (1998).

[109] G. Yang, G. Liu, New Insights for Self-Assembled Monolayers of Organothiols on Au(111) Revealed by Scanning Tunneling Microscopy. The Journal of Physical Chemistry B. 107, 8746–8759 (2003).

[110] C. A. Widrig, C. A. Alves, M. D. Porter, Scanning tunneling microscopy of ethanethiolate and n-octadecanethiolate monolayers spontaneously absorbed at gold surfaces. Journal of the American Chemical Society. 113, 2805–2810 (1991).

[111] T. Sawaguchi, Y. Sato, F. Mizutani, In situ STM imaging of individual molecules in two-component self-assembled monolayers of 3-mercaptopropionic acid and 1-decanethiol on Au(111). Journal of Electroanalytical Chemistry. 496, 50–60 (2001).

[112] V. V. Korolkov, S. Allen, C. J. Roberts, S. J. B. Tendler, High-Temperature Adsorption of p-Terphenylthiol on Au(111) Surfaces. The Journal of Physical Chemistry C. 115, 14899–14906 (2011).

[113] R. M. Thorman, R. Kumar T. P., D. H. Fairbrother, O. Ingólfsson, The role of low-energy electrons in focused electron beam induced deposition: four case studies of representative precursors. Beilstein Journal of Nanotechnology. 6, 1904–1926 (2015).

[114] E. Böhler, J. Warneke, P. Swiderek, Control of chemical reactions and synthesis by low-energy electrons. Chemical Society Reviews. 42, 9219 (2013).

[115] M. E. Wacks, V. H. Dibeler, Electron Impact Studies of Aromatic Hydrocarbons. I. Benzene, Naphthalene, Anthracene, and Phenanthrene. The Journal of Chemical Physics. 31, 1557–1562 (1959).

[116] L. A. Gonzalez, M. Angelucci, R. Larciprete, R. Cimino, The secondary electron yield of noble metal surfaces. AIP Advances. 7, 115203 (2017).

[117] M. P. Seah, Slow electron scattering from metals. Surface Science. 17, 132–160 (1969).

[118] E. Böhler, J. Warneke, P. Swiderek, Control of chemical reactions and synthesis by low-energy electrons. Chemical Society Reviews. 42, 9219 (2013).

[119] T. Fukuma, K. Kobayashi, T. Horiuchi, H. Yamada, K. Matsushige, Alkanethiol self-assembled monolayers on Au(111) surfaces investigated by non-contact AFM. Applied Physics A. 72, 109–112 (2001).

[120] M. Nakaya, M. Shikishima, M. Shibuta, N. Hirata, T. Eguchi, A. Nakajima, Molecular-Scale and Wide-Energy-Range Tunneling Spectroscopy on Self-Assembled Monolayers of Alkanethiol Molecules. ACS Nano. 6, 8728–8734 (2012).

[121] C. A. McDermott, M. T. McDermott, J.-B. Green, M. D. Porter, Structural Origins of the Surface Depressions at Alkanethiolate Monolayers on Au(111): A Scanning Tunneling and Atomic Force Microscopic Investigation. The Journal of Physical Chemistry. 99, 13257–13267 (1995).

[122] G. E. Poirier, Mechanism of Formation of Au Vacancy Islands in Alkanethiol Monolayers on Au(111). Langmuir. 13, 2019–2026 (1997).

[123] M. Setvín, J. Javorský, D. Turčinková, I. Matolínová, P. Sobotík, P. Kocán, I. Ošťádal, Ultrasharp tungsten tips—characterization and nondestructive cleaning. Ultramicroscopy. 113, 152–157 (2012).

[124] N. Biere, S. Koch, P. Stohmann, V. Walhorn, A. Gölzhäuser, D. Anselmetti, Resolving

the 3D Orientation of Terphenylthiol Molecules on Noble Metals with Kelvin Probe Force Microscopy. The Journal of Physical Chemistry C. 123, 19659–19667 (2019).

[125] E. J. van Loenen, D. Dijkkamp, A. J. Hoeven, J. M. Lenssinck, J. Dieleman, Evidence for tip imaging in scanning tunneling microscopy. Applied Physics Letters. 56, 1755–1757 (1990).

[126] B. C. Stipe, Single-Molecule Vibrational Spectroscopy and Microscopy. Science. 280, 1732–1735 (1998).

[127] Y. Konishi, Y. Sainoo, K. Kanazawa, S. Yoshida, A. Taninaka, O. Takeuchi, H. Shigekawa, Tunneling spectroscopy and manipulation of a singleC2H2molecule on a Cu(111) surface. Physical Review B. 71 (2005).

[128] G. Binnig, H. Rohrer, Scanning Tunneling Microscopy. Surface Science. 126, 236 (1983).

Publications and Talks

Paper

Yang, Y., Dementyev, P., Biere, N., Emmrich, D., Stohmann, P., Korzetz, R., Zhang, X., Beyer, A., Koch, S., Anselmetti, D., and Gölzhäuser, A. Rapid Water Permeation Through Carbon Nanomembranes with Sub-Nanometer Channels. ACS Nano 12, 4695–4701 (2018).

Koch, S., Kaiser, C. D., Penner, P., Barclay, M., Frommeyer, L., Emmrich, D., Stohmann, P., Abu-Husein, Tarek., Terfort, A., Fairbrother, D. H., Ingolfsson, O., and Gölzhäuser, A. Amplified cross-linking efficiency of self-assembled monolayers through targeted dissociative electron attachment for the production of carbon nanomembranes. Beilstein Journal of Nanotechnology 8, 2562–2571 (2017).

Eickenberg, B., Wittbracht, F., Stohmann, P., Schubert, J.-R., Brill, C., Weddemann, A., and Hütten, A. Continuous-flow particle guiding based on dipolar coupled magnetic superstructures in rotating magnetic fields. Lab on a Chip, 13(5), 920 (2013).

Biere, N., Koch, S., Stohmann, P., Walhorn, V., Gölzhäuser, A., Anselmetti, D. Resolving the 3D Orientation of Terphenylthiol Molecules on Noble Metals with Kelvin Probe Force Microscopy. The Journal of Physical Chemistry C. 123, 19659 (2019).

Conference Talks

Stohmann, P., Koch, S., Yang, Y., Kaiser, C.D., Biere, N., and Gölzhäuser, A. Molecularly resolved STM imaging of electron-induced cross-linking of aromatic self-assembled monolayers. DPG Frühjahrstagung (2019), Regensburg, Deutschland.

Stohmann, P., Koch, S., Yang, Y., Kaiser, C.D., and Gölzhäuser, A. Investigation of stepwise crosslinked 4-terphenylthiol self-assembled monolayers. DPG Frühjahrstagung (2018), Berlin, Deutschland.

Stohmann, P., Eickenberg, B., and Hütten, A. Microfluidic device using anchored, 1D superstructures of superparamagnetic beads for controllable particle filtration. DPG Frühjahrstagung (2014), Dresden, Deutschland.

Poster Presentations

Stohmann, P., Koch, S., Hinaut, A., Glatzel, T., Meyer, E., and Gölzhäuser, A. Deposition of biphenylthiols on Au(111) by Electrospray Ionization. DPG Frühjahrstagung (2017), Dresden, Deutschland.

Kaiser, C.D., Stohmann, P., Frommeyer, L., Koch, S., Husein, T., Terfort, A., and Gölzhäuser, A. Radiation reduced CNM formation from halogenated biphenylthiols. NMWP Think Tank-Konferenz (2016), Siegen, Deutschland.